Fabrication and Application of Surface-anisotropic Particles

by

Amar Babanrao Pawar

A Dissertation Submitted to the Graduate Faculty in Engineering in Partial Fulfillment of the Requirements for the Degree of Doctor of Philosophy

The City University of New York

2009

This manuscript has been read and accepted for the Graduate Faculty in Engineering in satisfaction of the dissertation requirement for the degree of Doctor of Philosophy.

Date	Prof. Ilona Kretzschmar Chair of Examining Committee
Date	Prof. Mumtaz Kassir Executive Officer
	Prof. Alexander Couzis
	Prof. Charles Maldarelli
	Prof. Joel Koplik
	Prof. Marc Donohue

Supervision Committee

THE CITY UNIVERSITY OF NEW YORK

Abstract

Fabrication and Application of Surface-anisotropic Particles

by

Amar B. Pawar

Advisor: Ilona Kretzschmar

Engineering the surface properties of particles has provided a powerful tool to fabricate novel building blocks for future materials. Techniques that are capable of producing a diverse spectrum of surface-anisotropic particles in large-scale quantities by varying easily adjustable experimental parameters are needed. In this thesis, we present a Glancing Angle Vapor Deposition (GLAD) technique to produce a wide variety of surface-anisotropic (patchy) particles and study their potential for future applications.

The GLAD technique is utilized to produce patchy particles with predefined patch sizes varying from 3.7 to 50 % of the particle surface. The technique is further extended to fabricate patchy particles with overlapping patches on the same hemisphere of the particle. The controlled overlap of the patches provides a new engineering dimension to these particles. A particle stamping technique is employed to access the whole particle surface during vapor deposition. The particle-stamping technique is implemented to produce patchy particles with two independent, non-overlapping patches on opposite poles by inverting the particles on a polymer stamp.

Patchy particles are investigated under AC electric fields, in concentration gradients, and in self-assembly. The dielectrophoretic behavior of patchy particles is tuned from staggered chains to network structure of horizontal and vertical chains as well as diagonal chains by varying the patch size and number. The autonomous motion of patchy particles due to a self-inflicted concentration gradient in reactive environments is studied experimentally and theoretically. Last but not the least, DFT based

models are employed to investigate the self-assembly of patchy particles into target structures.

Overall, the GLAD technique is shown to provide precise control over the surface anisotropy of patchy particles. Further, the degree of surface anisotropy of the patchy particles is found to influence their properties, which enables their implementation in functional structures and a wide range of applications.

Acknowledgements

First and foremost, I want to express my sincere gratitude towards my advisor Prof. Ilona Kretzschmar for her unflinching support and guidance throughout my research work. She has been an excellent mentor and above all a good friend. I am thankful for the enthusiasm for the research she has shown at each stage of this thesis. I truly believe that she is the ideal mentor that any student can ask for.

Further, I would like to thank my PhD committee members Prof. Alexander Couzis, Prof. Charles Maldarelli, Prof. Joel Koplik, and Prof. Marc Donohue for providing the necessary feedback and guidance. I appreciate the generous guidance provided by Prof. Maldarelli in solving the transport theory problems in this research. A special thanks to Dr. Gregory Aranovich and Prof. Marc D. Donohue for our enlightening discussions about the T-structure project.

In addition, I would like to thank my present and alumni lab colleagues: Kevin, Jingqin, Hsin-yu, Bin Ren, Sonia, Amara, Mahmud and Carlos for proving the motivating work environment in the lab. Without friends, life as a graduate student would not have been the same. A big thank you to all you guys: Rohit, Anil, Pandurang, Manoj, Shyam, Sandeep, Vikas, Nikhil K/B, Prasad Y/K, Shripad, Swapnil, John, Rajesh, Ashish, Abhinav, Jayant, Nilesh, Vilobh, Pratik and Mayur for excited, cheerful four and half years at CCNY.

Finally, I would like to dedicate this thesis to my parents, Mr. Babanrao Pawar and Mrs. Nanda Pawar. It is the result of their enduring efforts, love and confident support that I am able to undertake and finish this thesis. They gave me the freedom to choose my career path and always encouraged me to achieve higher and higher goals in life.

Contents

List of Figures

Chapter 1

Introduction

Various innovative particle synthesis techniques have led us to the next generation of materials. Not just limited to isotropic building blocks, a wide variety of anisotropic particles with diverse anisotropy in size, shape,[1–6] and chemical functionality[7–14] has been explored. Within such a large diversity of anisotropic particles, significant attention has been given to the study of surface-anisotropic particles, i.e., particles exhibiting multiple surface functionalities. The simplest example of particle surface-anisotropy is a particle possessing two hemispheres with dissimilar properties. The two halves of the particle may differ in electrical, chemical, or physical properties. Such particles, with two distinguishable hemispheres are most commonly referred to as "Janus" particles.[15] Janus particles have been an active area of research for the past few years. A lot progress has been made in the research field of fabrication and characterization of Janus particles as well as towards testing and exploring their applications.[8,13,16–18] Undoubtedly, Janus particles present an interesting approach to new materials with dual distinguishable properties. However, not restricting the surface coverage to 50 %, as is the case for Janus particles, a precise control over dual or multiple properties of a particle can be achieved by varying the proportion of the different surface-functionalities. This strategy has led to a new class of particles, "patchy particles", i.e., particles with more than one patch or patches that are less than 50 % of the total particle surface.[19]

The potential applications of such surface-anisotropic particles lie in fabricating photonic crystals,[20] targeted drug delivery[21,22] and electronics[23] and have been reported earlier. It is crucial to put the surface-anisotropic particles together into a functional form that will be employed in the aforementioned applications. Implementing the patchy particles in functional, applicable structures has opened a door to study the self- and directed-assembly of such particles. The directed- or self-assembly of particles, also well-known as "bottom-up" strategy has a great potential to overcome the size limitations and processing restrictions of present-day, "top-down" manufacturing processes such as photolithography.[24–27] The anisotropic nature of the particle-surface enables a certain degree of control over the assembly process, since the specific interactions between the anisotropic particles can provide a driving force for the assembly of a target structure. Recently, several computational studies on the self-assembly of surface-anisotropic or patchy particles have been reported.[28–35] But fabrication of patchy particles is still a developing research area and is gaining more and more attention rapidly.[10–12]

This thesis strives towards fabrication of patchy particles with a controlled degree of surface modification. The patchy particles investigated here possess metallo-dielectric properties owing to the gold patches on the dielectric polystyrene particle core. The Glancing Angle Vapor deposition (GLAD) technique is employed to produce patchy particles with a single patch. The GLAD technique is further extended to produce multifunctional patchy particles, particles with more than one patch which can be made up of different materials or of unique patches of the same material. The produced patchy particles are used to fabricate two-dimensional (2D) metallo-dielectric crystals by virtue of an external electric field. Our study investigates the effect of the size of the patch on the assembled crystal structure. Yet another application of patchy particles as osmotic motors in a suitable chemical environment is studied. The computational aspect of the thesis involves understanding the effect

of physical parameters such as interaction energies, temperature, and concentration on the assembly of such patchy particles into well-defined target structures.

In the following, Chapter 2 presents a detailed literature review on advances in the fabrication of surface-anisotropic patchy particles along with advantages and limitations of the available techniques. In the later part of Chapter 2, applications of surface-anisotropic particles, both the computational and the experimental studies, are reviewed. Chapter 3 focuses on the fabrication of patchy particles. The two sections in Chapter 3 describe the fabrication of single-patch particles using GLAD and the extension of GLAD to produce particles with multiple patches, respectively. The applications of fabricated patchy particles are explored in Chapter 4. The first section demonstrates experimental studies of the dielectrophoretic assembly of patchy particles. The following section contributes the application of patchy particles as osmotic motors. Computational studies of the self-assembly of patchy particles in molecular fluids using the principles of lattice density functional theory are reported in the final section of Chapter 4. The thesis is concluded by a future work chapter, Chapter 5.

Chapter 2

Patchy particles as novel materials

This chapter gives a brief overview of recent advances in the fabrication of surface-anisotropic particles and their applications. The first section explains various techniques currently used for surface modification of particles and their implications for producing patchy particles. Following the review of fabrication techniques, the next section discusses applications of patchy particles. Three application are explored: (i) Self- and external field directed-assembly of Janus particles, (ii) autonomous, self-propelling motion of osmotic motors, and (iii) computational studies of the assembly of patchy particles into well-defined target structures.

2.1 Anisotropic surface modification of colloids

Various techniques available for surface modification are broadly classified in two categories (i) Vapor Phase Deposition (VPD) and (ii) Liquid Phase Deposition (LPD). The vapor phase deposition techniques include physical vapor deposition, chemical vapor deposition, and molecular beam epitaxy, while the liquid phase deposition techniques include layer-by-layer deposition, electrochemical deposition, and electroless deposition techniques. Both the vapor and liquid phase deposition techniques have been successfully used for producing surface-anisotropic colloids. A symmetric coating of the entire object/particle surface leads to core-shell particles,

while asymmetric coating results in only partial coverage of the particle surface forming asymmetrically modified particles. Selective modification of a partial surface of a particle is directly feasible in the case of VPD techniques because of the natural shadow effect, while in the case of LPD techniques various strategies are needed to shield part of the object surface from the modification.

The initial studies of surface-anisotropic particles are mostly directed towards fabrication of Janus particles (50 % surface-modified particles) and have provided us with numerous techniques for their synthesis.[8] For example, the direct physical vapor deposition of gold onto a monolayer of polystyrene particles is one of the earliest approaches reported for producing Janus particles.[16] Cayre et. al. have used a microcontact printing technique for transferring patterns of surfactants and colloidal monolayers onto another colloidal particle and have been successful in producing dipolar particles.[7] Temporary masking and demasking of colloids using gels or elastomers has been a successful strategy in liquid phase deposition techniques for producing Janus particles.[14,36,37] Though a variety of other techniques have also been developed for producing Janus particles,[38,39] very few of them can be extended or modified to produce patchy particles. Figure 2.1 summarizes recent advances in the techniques developed for fabrication of patchy particles along with applications they can be used in.

2.1.1 Particle lithography

The "Particle lithography" technique is a LPD-based technique developed for patterning individual particles site-specifically.[40,46] Figure 2.1(a) shows a schematic of the technique. Since particle lithography is a LPD-based technique, a mask is needed to produce site-specific functionalization. The essence of the method is that the charged polystyrene particles adhere to an oppositely charged surface. The region of contact between the particle and the surface is used as a mask for functionalization

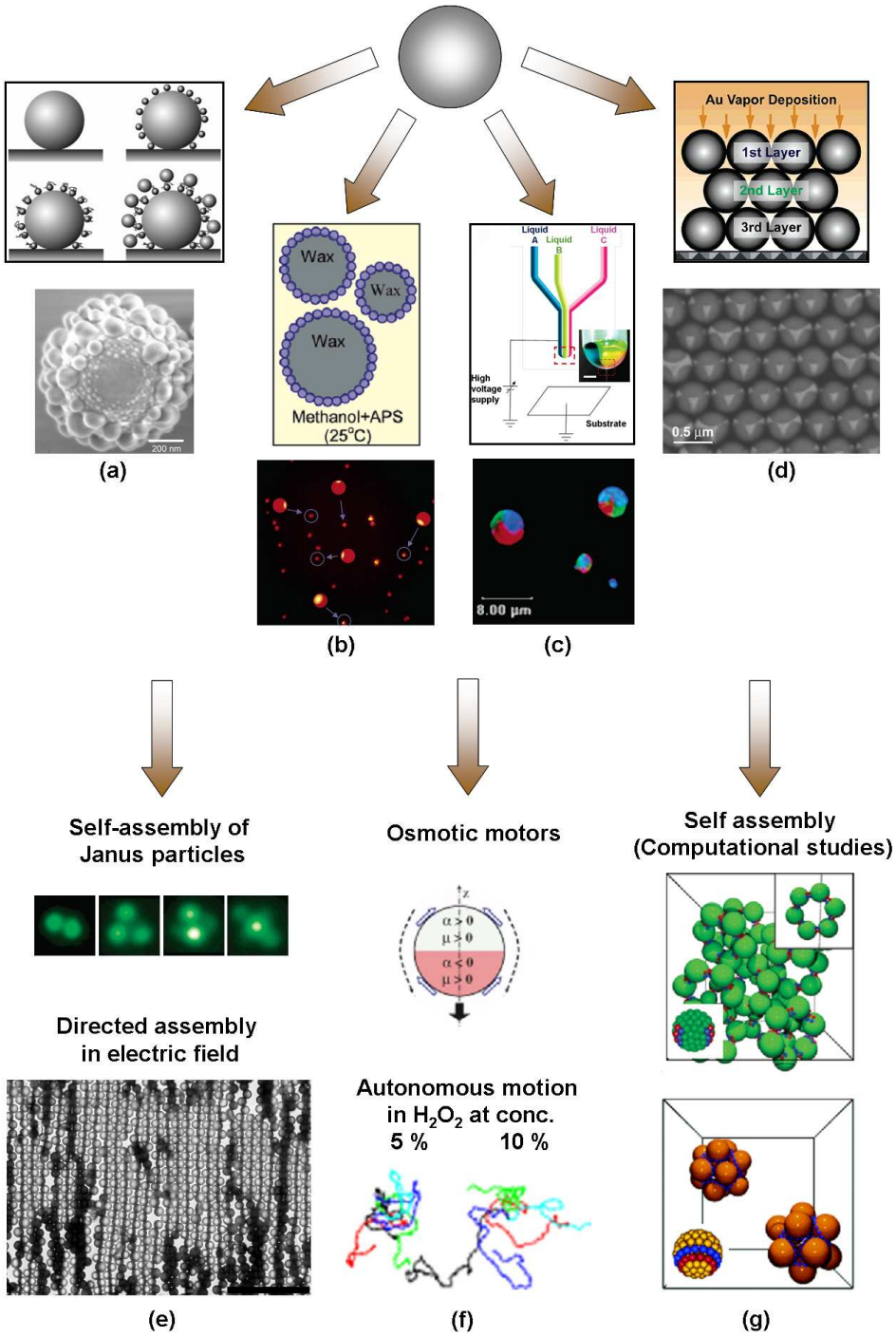

Figure 2.1: Synthesis (a) - (d) and applications (e) - (g) of patchy particles. Schematic and experimental images for patchy particle fabrication techniques (a) particle lithography technique,[12,40] (b) wax-in-water emulsion technique,[13,41] (c) micro-fluidic technique,[42,43] and (d) nano-sphere lithography technique.[10,11,44] Application of patchy particles (e) experimental studies of self-[18] (top panel) and directed-assembly[17] (bottom panel) of Janus particles, (f) Janus particles as osmotic motors,[45] and (g) computational studies of self-assembly of pathcy particles into rings and isohydra of particles.[29] The images are adopted from the references cited.

of the remaining surface area of the particle. For example, positively charged amidine functionalized polystyrene particles (3.3 μm) adhere to a negatively charged glass surface in water. The contact point between the sedimented particle and the glass surface is used as a mask for anisotropic surface modification of particles. Thus, negatively charged polyelectrolyte poly(styrene sulfonate) is specifically adsorbed onto the particle-surface avoiding the contact point. The size of the lithographed region can be controlled by varying the particle size, the radius of gyration, and the Debye length of the polyelectrolyte.[12] A Layer-by-Layer (LbL) patterning can be used to adsorb oppositely charged particles on the polyelectrolyte-coated particle surface area. Figure 2.1(a) shows such an example of a patchy particle produced by multilayered particle lithography that is composed of 2 layers of particles adsorbed on a 1 μm amine-functionalized silica particle. The first layer is made up of 10 nm sulfate polystyrene (PS) particles followed by a layer of poly (allylamine hydrochloride) (PAH) adsorbed onto them, followed by adsorption of a second layer of 84 nm sulfate latex PS particles onto the PAH layer.

The particle lithography technique is a versatile liquid phase based technique and allows coating of particles with liquid-based reagents, which allows site-specific functionalization with proteins or DNA. Despite its advantages, the technique inherently lags with respect to scale-up issues as the process is based on functionalization of individual colloids. Also, the time scales required for each step are considerable and complex base-surface geometries are needed for creating multi-patterned particles.

2.1.2 Oil in water emulsion technique

The scale-up of the techniques for producing large quantities of surface-anisotropic particles is a big concern when these particles have to be implemented in practical applications. The emulsion-based techniques are promising techniques for scale-up as large quantities of patchy particles can be synthesized using these techniques.

The initial emulsion-based approach suggests to add a small amount of water to a particle-in-oil dispersion. The silica particles aggregate because of the capillary forces and form clusters, whose exterior is chemically modified.[47] The method is further modified and extended to produce a large amount of Janus particles where the surface coverage is controlled by thermodynamic conditions.[13] The schematic of the emulsion technique is presented in Figure 2.1(b) with the epifluorescence microscopy images of fabricated Janus particles. The silica particles are modified with fluorescently labeled (aminopropyl)triethoxysilane (APS) in methanol solution.

The proposed emulsion technique to produce Janus silica particles uses molten paraffin wax as an oil phase for the oil-in-water emulsion. The emulsion is made at higher temperatures (75 °C) when the wax is molten. The particles are adsorbed at the oil-water interphase and form colloidosomes for surface functionalization of particles in either the water or the oil phase.[48] The distance by which the particles penetrate into the wax determines the amount of functionalized area. The embedment of particles in the wax is controlled by controlling the hydrophobicity of the particles. As the particles become more hydrophobic, they are embedded more into the wax phase and less surface area is available for functionalization from the water phase. Thus, the concentration of surfactant is an easily controlled parameter which in-turn controls the functionalized area of the particle surface. For example, negatively charged silica particles (3 μm diameter) are observed to embed more and more into a wax droplet as the concentration of didodecyldimethylammonium bromide surfactant is increased.[41] The particles are trapped at the oil-water interface by lowering the temperature when the wax solidifies. Finally, after surface functionalization of the particles at room temperature, the wax is molten by raising the temperature and the particles are recovered by centrifugation. Such an asymmetric modification of interfacially adsorbed silica particles with gold on a planar liquid water surface has also previously been observed by Petit et. al.[49]

The emulsion technique has the advantage that large quantities of Janus particles can be easily fabricated. Also, the amount of surface functionalization is easily controlled by controlling the concentration of additional reagents. However, the most critical step in the procedure is the separation of the modified particles from the oil or wax phase.

2.1.3 Microfluidic synthesis

Apart from just relying on the surface functionalization of isotropic colloids, attention has been given to the production of multiphasic colloids directly via polymerization of a mixture of polymers inside a single particle.[9,42,43,50,51] Such colloids contain two or more compartments of different polymer materials. The individual phases of polymers within a particle can be loaded or functionalized with a specific type of molecules, which introduces anisotropy to the resulting particles, not limited to the surface but also in the bulk of the particles.

The microfluidic technique is used to produce Janus or ternary droplets of immiscible monomers, emulsified in an aqueous solution. The droplets are polymerized with UV light for synthesis of Janus or ternary particles with size distributions from 40 to 100 μm.[50,51] Electrified co-jetting is used as an alternative to produce Janus particles with two distinct bulk properties.[9] The electrified co-jetting process involves manipulation of liquid jets at the nanometer scale using electro-hydrodynamic forces. The process has been extended to produce biphasic and triphasic nanocolloids.[42] A typical experimental procedure involves a laminar flow of three distinct polymer solutions through a modified nozzle opening. The schematic of the flow apparatus is shown in Figure 2.1(c). The three capillaries are aligned to form a multiphasic liquid flow. A high voltage electric potential, applied across the conductive capillary and the substrate, produces electrostatically charged liquid droplets. The jet extension followed by the jet break down and the solvent evaporation results into multiphasic

nano-colloids.

Figure 2.1(c) shows a confocal image of triphasic nanocolloids fabricated with the electrified co-jetting technique. The three phases of the particles contain biomolecules labeled with FITC, rhodamine B, and Alexa Fluor 647 dye. The electrified co-jetting technique has the distinct advantage that the process can be operated in a continuous fashion thereby increasing the scale-up possibility. The main constrain in this technique is that the particle size distribution is not uniform. Also, the secure operation of the co-jetting apparatus is facilitated but not limited towards use of water-soluble polymers.

2.1.4 Nanosphere lithography

Nanosphere lithography[52] or natural lithography[53] is a vapor phase deposition based surface modification technique where colloids or nanospheres are used as a lithographic mask for creating patterns on surfaces. The presence of an external shadow mask between the source and the substrate creates a deposition pattern on the substrate in VPD techniques. Thus, the resolution of the shadow mask is of utmost importance in creating nanoscale patterns. Fabrication of an external shadow mask is a cumbersome procedure and requires accurate precision. However, nanosphere lithography represents an intrinsic advantage in lowering the resolution of the patterns created to the size of the particles used in the technique. Nanosphere lithography can also be employed to produce patchy particles. It uses upper single or double layers of particles as shadow masks for patterning spheres in lower layers within a multilayered colloidal crystal.[10] Thus, use of any external shadow mask is avoided and the resolution of patterns created is as low as $\sim$ 50 nm.

Figure 2.1(d) represents a schematic of the nanosphere lithography technique. Vertical vapor deposition is performed on a close-packed multilayered colloid crystal. As depicted in the schematic, the uppermost layer acts as a shadow mask for the

second and the third layer, while the first and the second layers act as shadow masks for the third layer. The experimental results in Figure 2.1(d) show Au patterned 520 nm silica particles within the second layer of the colloidal crystal. The versatility of the technique is demonstrated by fabricating a variety of Au patterned colloids. The geometry of the Au pattern produced on the particles is dependent on the orientation of particles in the different layers. Also, the geometry of the pattern depends on the position of the layer to which the modified particle belongs.

The nanosphere lithography technique has the intrinsic advantage that the resolution of the patterns created is dependent on the particle size and not on the resolution of the external shadow mask. The main drawback of the technique is that particles within different layers get different amounts of surface modification. Thus, separation of particles based on the layer they belong to is necessary to obtain particles with uniform functionalization.

The concept of nanosphere lithography can be modified to avoid the difficulty of particle separation. Instead of using upper layers as shadow masks, particles within the same layer can be employed as shadow mask when the vapor deposition is done on a close-packed monolayer of particles at an inclined angle. Vapor deposition at an inclined angle is known as glancing angle vapor deposition (GLAD).[54,55] The GLAD technique is commonly used to produce silicon nanocolumns. The shadow effect of the angle-resolved nanosphere lithography on the substrate below the colloidal monolayer has been studied and quantified by Haynes et. al.[56] In this thesis, we demonstrate the application of the GLAD technique to fabricate surface-anisotropic particles. The details of the developed technique are reported in Chapter 3.

2.2 Applications of patchy particles

As discussed in the previous section a lot of attention has recently been given to the synthesis of patchy particles. The enormous efforts to produce such particles are fueled by the aspiration to utilize these particles for various applications. It is crucial to put these novel particles into functional structures to use them for practical purposes. One of the strategies is to assemble these particles into desired target structures, which will further be employed in photonics, electronics, or sensor applications. Other applications of such surface-anisotropic particles are anisotropy based switching for displays, self-healing materials, or drug delivery, which have been reviewed recently.[57] Application of patchy particles in assembling desired target structures and as autonomous osmotic motors are briefly discussed in the following subsections.

2.2.1 Self- and directed assembly of Janus particles : Experimental Studies

Self-assembly is a process where the building blocks assemble according to the nature of forces between them without any human intervention. The emerging approach of directed assembly lies in predefining the instructions for the assembly by controlling the interactions between the constituent building blocks. Thus, in the context of assembling target structures, surface-anisotropic particles play an important role by inducing directionality in the assembly process.

Recent experimental studies involving self- and directed assembly of Janus particles have shown the potential of transferring the computational predictions into practical realty. The experimental study of the assembly of Janus particles, particles with opposite charge on both hemispheres, shows clusters of Janus particles rather than strings (Figure 2.1(e)).[18] The experimentally observed cluster size and shapes of

colloids are confirmed with Monte-Carlo simulations. Both the experimental clusters and computational predictions are in very good agreement.

Not just relying on the intrinsic interactions between Janus particles, external fields such as electric or magnetic fields have been used to study the assembly of Janus particles. The AC dielectrophoretic assembly of metallo-dielectric Janus particles, dielectric particles possessing a metallic hemispherical surface, have been studied by Gangwal et. al.[17] Such Janus particles assemble into staggered chains and 2D metallo-dielectric crystals at higher field frequencies (> 10 kHz). Figure 2.1(e) shows a metallo-dielectric crystal of Janus particles assembled in an AC electric field at 125 kHz field frequency. The Janus particles are assembled in such a way that the metallic caps are facing each other and form a conductive lane throughout the staggered chains. At lower frequencies (< 10 kHz) self-propelling motion of Janus particles is observed due to ICEP (Induced Charge Electrophoresis).[58]

Apart from the assembled structures of Janus particle, Janus particles themselves have also been used in applications such as "electronic paper". The dipole response of "gyricon" balls (particles possessing two halves with distinct electrical properties) to an external electric field has been studied by Crowley et. al.[59] The rotation of such gyricon balls in the electric field has been implemented in "electronic paper".

2.2.2 Osmotic motors

Designing self-propelling microscale objects has been a challenge especially concerning the controlled motion of motors. Owing to an increased interest in the application of such autonomous motors as microrobots in medicine delivery, in fluid mixing, or for on-chip particle transport, various strategies have been developed to fabricate them.

One of the successful strategies recently developed includes conversion of chemical energy into mechanical work of propulsion. In the initial pioneering experiments,

Paxton et. al. observed autonomous motion of platinum-gold nanorods (370 nm dia. and 2 μm length) in a hydrogen peroxide solution.[60,61] The exact mechanism for the propulsion of these micro-swimmers is still a developing area of research and various models have been proposed. The autonomous motion of meso-scale objects (few mm) by bubble propulsion observed by Whitesides et. al.[62] is not responsible for the motion of nanorods since no bubbles are observed on the nanorod surface. Instead, it was suggested that the oxygen concentration gradient resulted in an asymmetric interfacial tension gradient around the PtAu nanorod that induces a slip velocity at the particle-fluid interface and the motion of particles is related to the interfacial force gradient across the rod surface.[60]

In another strategy, *phoretic* effects are employed to produce net particle motion. The gradients of fields such as concentration, temperature, or electric field can be used for colloid transport by interfacial forces.[63] The field gradient couples with the surface properties of the particle to produce slip velocity patterns, which results in a net propulsion of the particle. Such a diffusionphoretic motion of a particle is proposed by Golestanian et. al.[64] They propose that a particle with an asymmetric distribution of a catalyst on the surface propels itself due to an asymmetric distribution of reaction products generated by asymmetric surface catalytic activity. The resulting motion of particles is called "self-diffusiophoresis" of particles.

The concept of self-diffusiophoresis is further examined and experimentally verified by studying the autonomous motion of Janus particles (1.2 μm) in hydrogen peroxide solution.[45] The 50 % platinum-coated polystyrene Janus particles show an autonomous motion due to catalytic reduction of H_2O_2 only on the platinum-modified surface of the particles. Figure 2.1(f) shows a schematic of the proposed motion of Janus particles and their trajectories in 5 % and 10 % H_2O_2 solutions indicating the particle motion. The authors studied the motion of Janus particles as a function of H_2O_2 concentration and proposed a Michaelis-Menten type kinetics for the H_2O_2

reduction on the platinum surface at the microscale.

2.2.3 Self-assembly of patchy particles : Computational Studies

The experimental success of assembling surface-anisotropic Janus particles has directed more computational studies to predict the assembly of surface-anisotropic particles. The computational approach gives an advantage over the experiments. It enables researchers to think beyond the currently fabricated surface-anisotropic particles and to predict their assembly ahead of time. The results from the computational studies can be implemented to focus on developing techniques to fabricate the required patchy particles. In addition, it is time-consuming to test every possible thermodynamic condition experimentally and thus, theoretical studies of the assembly of patchy particles present an efficient tool for the prediction of process parameters and conditions required for the self-assembly.

The initial approach to incorporate directional anisotropic interactions in studying the phase behavior of globular proteins has been presented by Sear.[65] The model assumes the pair potential between globular proteins as a sum of two parts: a hard-sphere repulsion and a set of sites (sticky patches), which mediate short-range attractions. The phase behavior of globular proteins with such directional attractive interactions has been shown to have a phase diagram similar to that of short-range isotropic interactions. However, because of the directional attractive interactions, the solid phase of proteins is not always a hexagonally close-packed or face-centered cubic structure. Instead it has been reported that the binding site configuration decides the final phase structure. Although, anisotropic interactions have been included in the calculations previously, during recent years significant attention has been focused on assembling target structures using such anisotropic interactions.

The computational study of the assembly of patchy particles into well-defined

structures has been reported by Glotzer et. al.,[29,32] who show that the patchy particles can be successfully used to produce predefined structures such as rings, sheets, tetrahedra or diamond-like structures. Patchy particles are modeled in the simulations as particles with discrete, attractive patches on the particle surface. In the study by Zhang et. al.,[29] the attractive or repulsive interactions between the patches of the particles are accommodated in the model by assigning arbitrary interactions to the atoms comprising the particles. Brownian dynamics simulations are used to simulate an isothermal system and the solvent is implicitly included in the calculation through the choice of interaction potentials. In the study, the authors have shown that a wide range of patchy particles with different orientations of patches can be used to produce a variety of structures such as polyhedra, sheets, rings, etc. Figure 2.1(g) shows the assembly of patchy particles into rings and isohydra as predicted in the simulations by Zhang et. al.[29] The type of patchy particles needed to form rings or isohydra are shown as insets (bottom left) in Figure 2.1(g).

More studies to include anisotropic interactions in simulations and to understand the order-disorder transitions in such systems have been reported recently.[33,34] Aranovich and Donohue have successfully implemented a 2D Ising lattice model along with the principles of lattice density functional theory for modeling self-assembly in molecular fluids. Particularly, phase transitions and the self-assembly of supramolecular structures such as chains and sheets are observed with anisotropic monomers.[28] Wang has shown that the lattice model with Kawasaki-exchange dynamics can be employed to understand the dynamics of phase ordering and to obtain the equilibrium mean field solutions for the lattice model.[66] In particular, the dynamic mean field (DMF) model has been used for studying the phase behavior of anisotropic monomers.[34]

Chapter 3

Fabrication of Patchy Particles

In this chapter the application of glancing angle deposition (GLAD) as a means to produce surface-anisotropic (patchy) particles is reported. The first section summarizes the fabrication of patchy particles with variable patch size and shape. Patchy particles with a patch size from 50 % of the particle surface (Janus particle) to as small as 3.7 % of the particle surface are fabricated using GLAD.[67] The subsequent section demonstrates an extension of GLAD to produce patchy particles with multiple patches having a variable patch size, shape, and orientation on the particle surface. In order to access the entire particle surface, a particle stamping technique is employed using a PDMS stamp. The particle stamping technique along with GLAD is implemented to yield multifunctional patchy particles having patches on opposite poles.

3.1 Patchy particles with single patches by GLAD

Vapor deposition onto a close-packed monolayer of colloids is a widely used technique to produce surface-anisotropic particles.[10,11,16,44,68] Straightforward vertical vapor deposition onto a monolayer of particles yields Janus (50 % coated) particles.[16,68] The technique has been extended by Zhang et. al. to yield patchy particles with patches smaller than 50 % by performing vertical vapor deposition onto

multilayers of particles as discussed in subsection 2.1.4.[10] In the modified technique, the particles in the upper layer of a multilayered crystal act as shadow masks for the surface modification of particles in the lower layers. The main disadvantage of the technique is that the particles within each layer get modified in different proportions, i.e., particles in the top most layer are 50 % modified and the particles in the layer beneath exhibit four patches covering less than 50 % of the particle surface. Thus, separation of the particles based on their patch size and the patch number is necessary. In order to avoid this difficulty and to produce patchy particles with uniform patch sizes, we employed the GLAD[54,55] technique, where vapor deposition on a close-packed monolayer of particles is performed at an angle. In the current technique, particles within the same monolayer act as shadow mask and no further separation of the shadow mask from the fabricated particles is required.

3.1.1 Experimental details

Convective assembly of microspheres into close-packed monolayer

The convective assembly method is used to produce close-packed monolayers of 2.4 μm sulfate latex polystyrene (PS) particles (Invitrogen Inc.). The procedure and the details of the process are explained in details by Velev et.al.[69] The schematic of the coating apparatus is shown in Figure 3.1(a). The apparatus consists of two precleaned glass slides (cleaned with conc. sulfuric acid and Nochromix solution) inclined at an angle ($\sim 20^\circ$ - 30°). Concentrated solution (16 % - 24 % w/v) of PS particles is injected into the wedge between the two glass slides. Approximately 10 μl of solution is used for each experiment. The bulk of the liquid drop is held in the wedge due to capillarity and the drop meniscus stretches out as the linear motor of the syringe pump pushes the deposition plate at fixed speed. The coatings are deposited at an ambient temperature (20 - 30° C) and a relative humidity of 30 - 50 %. The speed of the deposition is adjusted based on the ambient conditions to

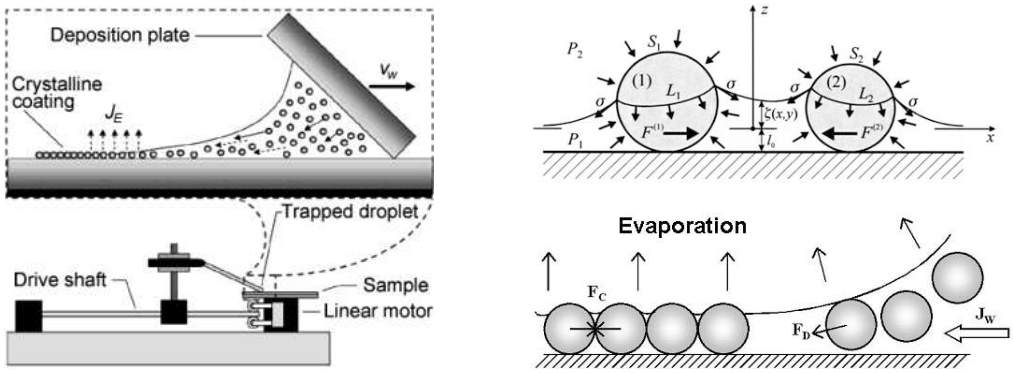

Figure 3.1: Details of the convective assembly method. (a) Schematic of the film coating apparatus.[69] (b) The process of convective assembly. Top figure[70] shows origin of capillary forces between partially immersed particles. The bottom figure indicates capillary forces leading to a close-packed monolayer of colloids.

obtain a close-packed monolayer of particles. For 16 % concentrated solution of 2.4 μm colloids a deposition speed of 6 - 8 μm/s is used for producing the close-packed monolayer.

The top schematic in Figure 3.1(b) shows the details of the origin of immersion capillary forces between the partially immersed particles leading to the formation of 2D arrays of colloids.[70–74] The net horizontal force F_1 exerted on particle 1 is the net force due to surface tension, σ, integrated along the contact line L_1 and the pressure distribution integrated along the particle surface S_1.[70] The bottom schematic in Figure 3.1(b) shows a drying region in the thin film produced during the film deposition using the apparatus shown in Figure 3.1(a). J_w is the flux of the solvent during evaporation, which produces the drag force F_D on the particles. The immersion capillary forces (F_C) between the particles lead to a close-packed monolayer. The dragging speed of the meniscus determines the film thickness during evaporation. A film thickness of less than a particle diameter is needed to keep the particles partially immersed. A lower dragging speed leads to higher film thickness, which results in multilayers of particles while a higher dragging speed leads to sub-monolayer formation.

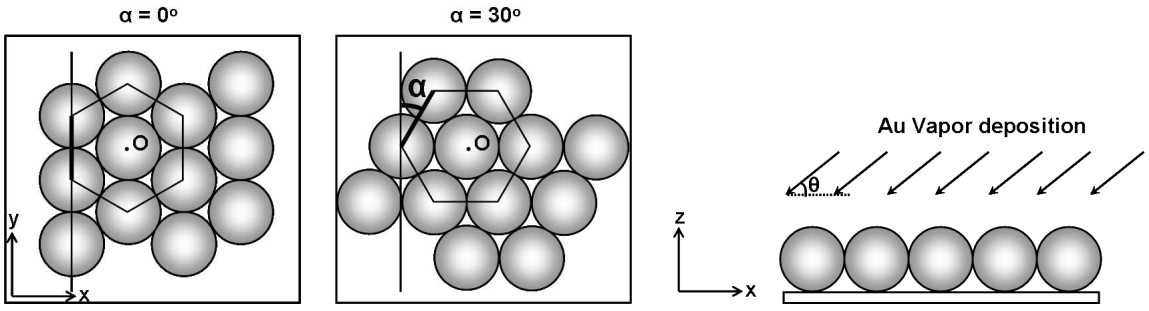

Figure 3.2: Schematic of monolayer orientation and GLAD with respect to incident vapor beam. (a) x-y cross section indicating monolayer orientation at α= 0°, and (b) α = 30°.(c) x-z cross sectional view indicating angle of incidence θ.

Close-packed domains of colloids with varying monolayer orientations are observed within a 2D array of particles produced by the convective assembly. The average domain size is $\sim$ 15000 μm^2 ($\sim$ 3000 particles of 2.4 μm diameter). The orientation of the monolayer domains is denoted by the angle α. The monolayer orientation as shown in Figure 3.2(a), is set as a reference, α = 0°, and for all the remaining orientations α is calculated by measuring the domain's clockwise rotation with respect to the reference orientation as shown in Figure 3.2(b) for α = 30°.

Glancing Angle Vapor deposition

Gold or silver vapor deposition on the close-packed colloidal monolayer is performed inside a bench top vacuum metal evaporation system (Cressington 308 R, Ted Pella, Inc.) at a pressure of 10^{-6} mbar. Figure 3.2(c) represents a schematic view of an angled vapor deposition onto a close-packed monolayer. The angle of incidence of gold vapor also referred to as the angle of vapor deposition, θ, measured from the substrate as shown in Figure 3.2(c) (θ = 90°, being perpendicular to the sample), is adjusted by tilting the sample in the vacuum chamber. The sample is accurately tilted using a cell made from rectangular acrylic blocks. The acrylic cell consists of two vertical parallel plates mounted on a horizontal acrylic block. The sample glass slide (thickness = 0.12 cm) is cut to a specific length (3.3, 2.2, and 4.4 cm for 30°,

10°, and 5° angle of evaporation, respectively) and placed at an inclination between the two plates. The separation distance between the two vertical plates is adjustable (1.8 cm for 30° and 0.51 cm for 10° and 5° angle of evaporation) and determines the tilt angle of the glass slide, which corresponds to the angle of vapor deposition, θ. In the case of the silicon wafer ($\sim 2 \times 2$ cm^2), the wafer is taped to a glass slide using double-sided sticky tape, and the glass slide is inclined as described above, which also tilts the wafer. The distance between the source and the inclined sample is $\sim$ 15 cm. The small monolayer area ($\sim 1 \times 1$ cm^2), the long working distance ($\sim$ 15 cm), and the two vertical acrylic plates minimize the divergence from the evaporation source and lead to a uniform patch geometry across the entire monolayer.

A quartz crystal microbalance mounted in the evaporator at an angle of $\sim 30°$ to normal incidence is used to monitor the vapor deposition. The evaporation source is blocked off when a 20 nm thickness is measured by the quartz crystal microbalance. The actual thickness of the patches depends upon the angle of evaporation and the position of the sample with respect to the source. After the evaporation, the samples are imaged using a variable pressure (VP) scanning electron microscope (EVO40 Zeiss).

SEM imaging of patchy particles

The imaging of the particles is performed at a variable pressure (VP) of 30 - 40 Pa, an accelerating voltage of 10 - 15 kV, and a working distance of 6 - 7 mm, using a VP EVO40 Zeiss scanning electron microscope with a variable pressure secondary electron (VP-SE) detector. In VP mode, ambient air is leaked into the chamber and subsequently ionized by the electron beam, leading to a cloud of positive ions around the beam. The positive ions pick up trapped charges from the surface of the nonconductive sample, creating a charge equilibrium, which enables the imaging of nonconductive materials without a conductive coating.[75] Note, metals usually appear brighter than hydrocarbons in SEM because of their higher electron density.

3.1.2 Mathematical model for patch geometries

A mathematical model is used to analyze the geometries of the patches obtained with GLAD. The mathematical model solves equations of spheres (representing particles) and inclined lines (representing incident rays), simultaneously. The obtained patch geometries are used for calculating the areas of the patches. The mathematical model allows us to predict the experimental parameters, such as the angle of vapor deposition, θ, required to deposit a patch of the desired size the particle surface.

Patch geometry calculations Figure 3.3 shows details of the mathematical model used for the patch-geometry calculations. The bottom panel (x-y view) shows a top view of two neighboring particles within a close-packed monolayer with an orientation of $\alpha = 30°$. The red colored boundary in the top view image shows the patch boundary obtained for vapor deposition at $\theta = 45°$. The top panel (x-z view) represents a cross section view in the x-z plane passing through the center of the two particles as shown by the dashed line in the top view (bottom panel). The red arrows are representative vapor rays intersecting with the particles.

The vapors depositing on the sample are represented by the equations of lines hitting the x-y plane at the angle of incidence θ and lying in the x-z plane. For a unit sphere diameter, the density of the incident rays used for patch calculations is such that the rays are spaced by 0.0005 units in the x and y directions. The intersection of rays and the spheres (for example, points C and D in the top panel of Figure 3.3) visualizes of the patch. In order to calculate the exact patch boundary, the rays tangent to the particles are determined. For example, points A and B in the top panel of Figure 3.3 lie on the patch boundary. The coordinates of points A and B are calculated from the tangents to the particle and the neighboring particle, respectively. We assume that the rays travel in straight lines parallel to each other

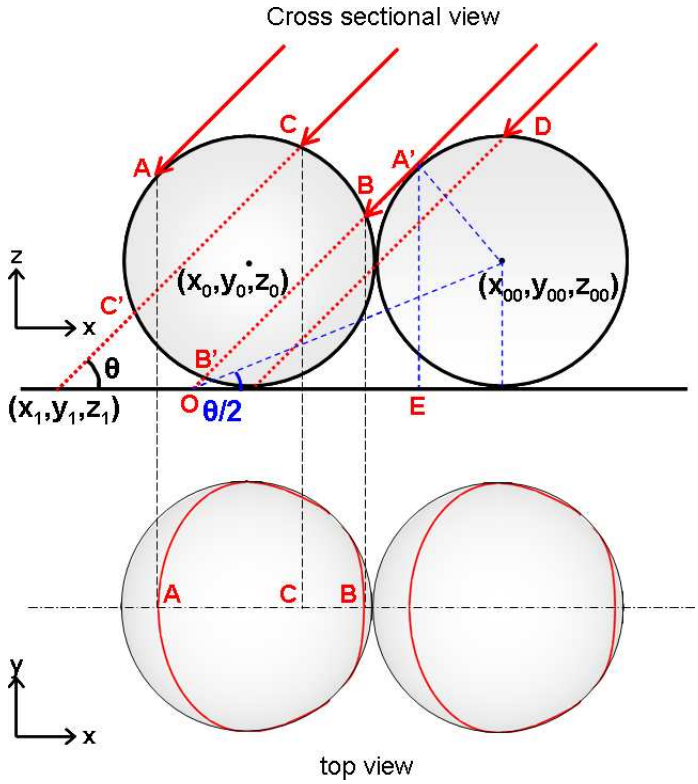

Figure 3.3: Details of the mathematical model. The cross-sectional view and top view of two particles in monolayer orientation $\alpha = 30°$. Incident rays (red arrows) intersecting spheres with centers at (x_0, y_0, z_0) and (x_{00}, y_{00}, z_{00}). The blue and black dotted lines are the constructions lines drawn for calculations.

and hit the sample at the angle θ. This assumption is based on the condition that the source is at an infinite distance with respect to the particle size, which is consistent with the experimental set-up, where the source distance to the sample ($\sim 10^{-1}$ m) can be treated as infinite compared to the particle size (2.4×10^{-6} m). The calculations are done for a monolayer of 6×6 spheres. The equation of each line is solved simultaneously with the equation of the sphere with which it intersects. In the case where the ray intersects multiple spheres, the farthest x distance point (point closest to the source) is identified as a patch point and the rest of the solutions are discarded. The patch geometries are obtained by simultaneously solving the equations of all the rays with the 6×6 sphere matrix.

The equation of a sphere with a center at (x_0, y_0, z_0) is given as

$$(x - x_0^2) + (y - y_0^2) + (z - z_0^2) = 1 \tag{3.1}$$

In an x-z plane as shown in Figure 3.3 (top view), y = y_1 and the equation of the incident ray at (x_1, y_1, z_1) is written as

$$z = (x - x_1) \tan\theta \tag{3.2}$$

where θ is the angle of incidence. Solving the equation of the line and the equation of the sphere simultaneously with $y = y_1$ in the x-z plane gives two solutions corresponding to the intersecting points C and C$'$ as indicated in Figure 3.3. Equations (3.2) and (3.1) give a solution in terms of a quadratic equation with respect to x as:

$$x^2\{1+t^2\} - 2x\{x_0 + x_1t^2 + z_0t\} + \{x_0^2 + (y_1 - y_0)^2 + x_1^2t^2 + 2z_0x_1t + z_0^2 - 1\} = 0 \tag{3.3}$$

where $t = \tan\theta$. The solution of the quadratic equation (3.3) along with Eq.(3.2) gives the coordinates of the intersecting points C and C$'$. Point C is identified as a part of the patch and point C$'$ is discarded. In the case of a ray intersecting multiple spheres the point closest to the source is identified as a patch point (e.g., point D).

The exact patch boundary is calculated by taking into account the rays tangent to the circles ($x - z$ cross section of a sphere). For example, rays terminating at points such as point O (Figure 3.3) are used to calculate the coordinates of the points lying on the patch boundaries of both the spheres (e.g., A$'$ and B). For a tangent to a sphere with the center (x_{00}, y_{00}, z_{00}) the x-coordinate of point O (x') is calculated as

$$x' = x_{00} - \frac{1}{\tan(\theta/2)} \tag{3.4}$$

From the triangle $\triangle$ A′EO using trigonometry the coordinates of point A′ are calculated as

$$x'' = \cos(\theta)(x_{00} - x') + x' = \frac{\cos(\theta)}{\tan(\theta/2)} + x' \tag{3.5}$$

$$y'' = y_1 \tag{3.6}$$

$$z'' = \sin(\theta)(x_{00} - x') = \frac{\sin(\theta)}{\tan(\theta/2)} \tag{3.7}$$

The coordinates of the point B can be obtained by simultaneously solving the equation of the ray terminating at O and the sphere with the center (x_{00}, y_{00}, z_{00}) as described earlier.

Patch area calculations The geometry of the patches obtained using the mathematical model is used to calculate the patch area. The area of the patches is calculated by numerical integration using the points on the patch boundary. The patch is divided in stripes along the zenith angle. The area of a stripe is calculated by assuming the stripe to be a rectangular stripe and the summation over the areas of all stripes is used to approximate the area of the patch.

3.1.3 Results

Vapor deposition at an angle of incidence, θ, creates patches on the particles depending on θ and the monolayer orientation of the close-packed domains, α. Figure 3.4 shows 2D arrays of 2.4 μm Au patterned sulfated PS particles at different angles of incidence, $\theta = 30$, 10, and 2° and varying monolayer orientation, α. As θ is decreased from 90° to 2°, the shadow effect caused by the neighboring particles within the close-packed monolayer takes effect. The shadow effect determines the size and the shape of the Au patch created on each particle. As the angle θ becomes smaller, the shadow effect becomes stronger and smaller patches are formed. As shown in Figure 3.4, the Au patch size diminishes considerably as θ varies from 30° to 10° and

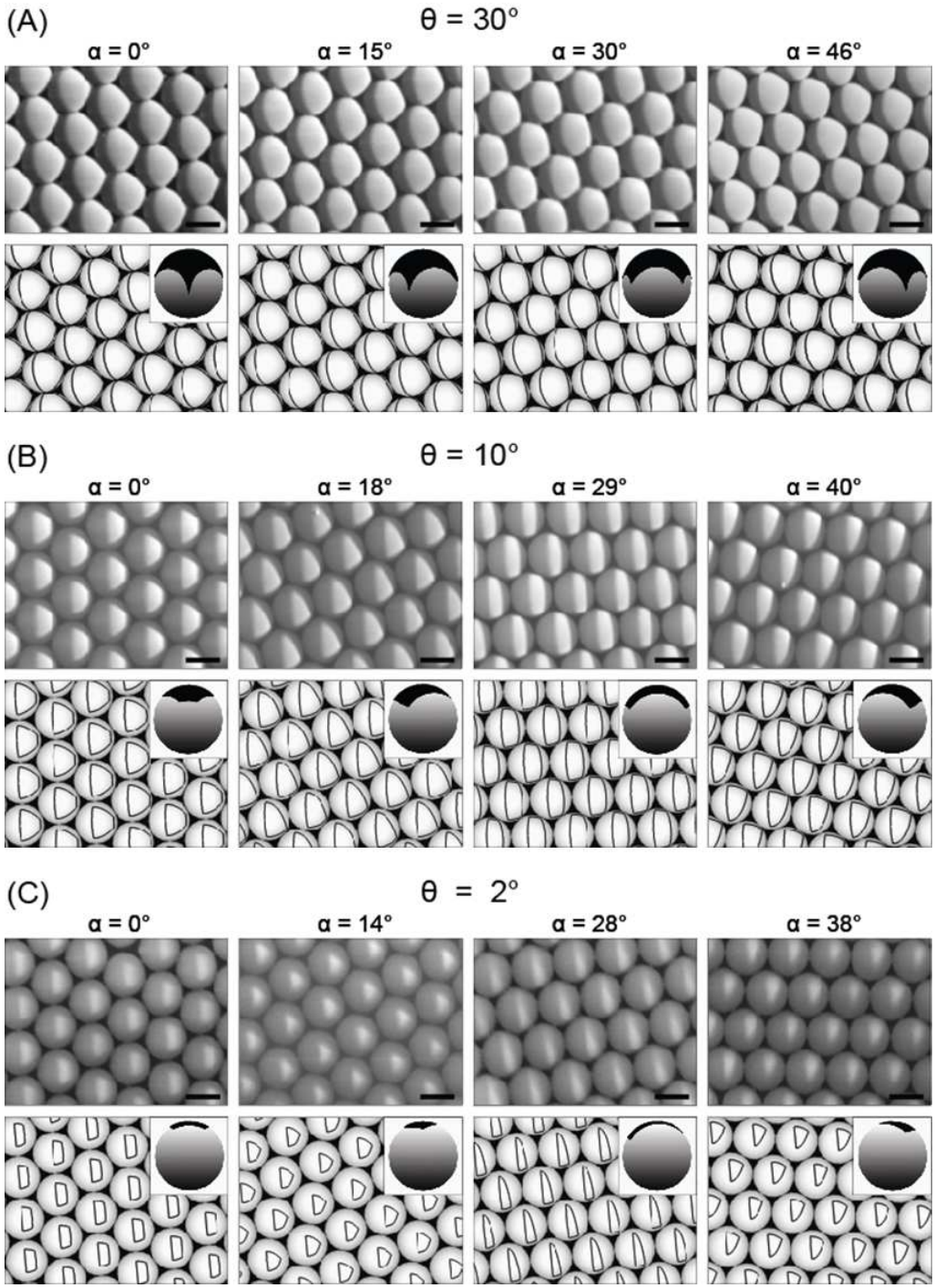

Figure 3.4: Comparison of experimental (top) and calculated (bottom) gold patches on 2.4 μm sulfated polystyrene particles as a function of angle of incidence, θ, and monolayer orientation, α. The images show the top view (x-y view) of the monolayer. (A) Patches obtained at an angle of incidence $\theta = 30°$ and a monolayer orientation of $\alpha = 0°$, 15°, 30°, and 46°. (B) Patches obtained at $\theta = 10°$ and $\alpha = 0°$, 18°, 29°, and 40°. (C) Patches obtained $\theta = 2°$ and $\alpha = 0°$, 14°, 28°, and 38°. Bottom panel insets: y-z view (i.e., view from source side) of a single patchy particle in the monolayer obtained with the mathematical model. Scale bars in experimental images correspond to 2 μm.

further decreases as θ is reduced to 2°. Scanning electron microscopy (SEM) images depict the top view (x-y view with respect to Fig. 3.2) of the PS particle monolayers patterned with gold.

The geometry of each patch obtained with the mathematical model is shown below each of the experimental SEM images with the corresponding angles. Experimental patch shapes and mathematically obtained patch shapes show very good agreement. The insets in the bottom panels of Figure 3.4 show the corresponding images of a single particle and its patch in a side view (y-z view).

The particle side facing the incidence Au rays is partially shadowed by neighboring particles from the next rows of particles closer to the source. The other side of the particle, i.e., the side away from the source, is partially shadowed due to the tangency of the incident rays to the particle itself. The boundary of the patch on the side of the particle facing away from the source (lagging boundary) is thus only determined by the angle of incidence θ, while the boundary on the side facing the incidence rays (leading boundary) is effected by θ as well as the monolayer orientation, α. As illustrated in Figure 3.4, the effect of monolayer orientation on the geometry of the patch is more pronounced at lower θ (10° and 2°) than at $\theta = 30°$. The pictures shown as insets indicate that as θ increases from 2° to 30°, patches with sharper corners are observed on the particles ($\theta = 30°$). The sharp corners disappear as θ increases further ($\theta > 30°$) due to a diminished shadow effect.

3.1.4 Discussion

As observed in Figure 3.4, at a fixed angle of deposition, θ, particles with variable patch sizes and shapes are obtained. When the monolayer orientation is such that $\alpha = 30°$, the leading boundary is flattened, which leads to rectangular patches with a curved surface (Figure 3.4). The flattening of the leading boundaries is due to the fact that these boundaries are caused by particles that are aligned exactly with

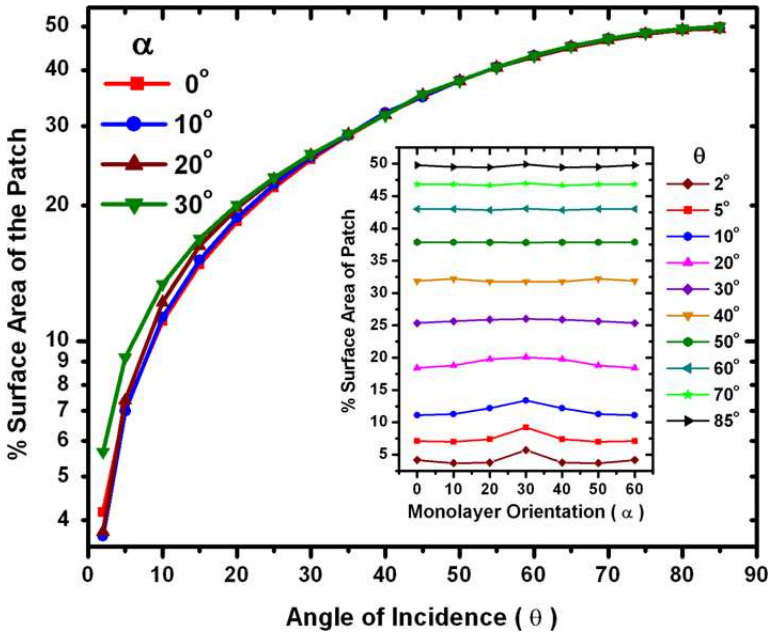

Figure 3.5: Patch area in % surface area of the particle plotted as a function of angle of incidence θ. Inset: Patch area in % surface area of the particle as function of monolayer orientation (α).

the particle they shadow. Flattening of the leading boundary is also observed when $\alpha = 0°$ but only at lower θ values (e.g., 10 and 2°). In case of $\alpha = 0°$, flattening of the leading boundary is caused by particles aligned in alternate rows. Thus, the flat leading boundary is observed only when alternate rows of particles take part in the shadow effect (e.g., $\theta = 10$ or 2°). If the shadow effect is restricted only by the next row of particles (e.g., $\theta = 30°$), sharp cornered leading boundaries are observed. The lagging boundary is caused due to the tangency of the incident Au rays to the particle itself. The location of the lagging boundary on particles is independent of the monolayer orientation α and is always flat. Also, patches are symmetric about the x-axis passing through the particle center for monolayer orientations $\alpha = 0°$ and $\alpha = 30°$. Such patch symmetry is not observed for any other monolayer orientation. Looking at the particles form the source position, the patch geometries are mirror images of each other around $\alpha = 30°$, i.e., the patch geometries for $\alpha = 15°$ and $\alpha = 45°$ are mirror images of each other.

Figure 3.5 shows the plot of the percentage sphere area patterned with Au as a function of the angle of incidence, θ, at different monolayer orientations. The area of the patches is calculated from the patch geometries obtained using the mathematical model. We expect the patch areas to be accurate within $\pm$ 0.5 %. The error is due to the numerical calculation of the areas. As mentioned before, the Au patch area behaves symmetrically around $\alpha = 30°$, i.e., the area of the patches are equal at $\alpha = 20°$ and $40°$, $\alpha = 10°$ and $50°$, and $\alpha = 0°$ and $60°$ for any θ. The plot shows that all monolayer orientations follow a similar trend of increase in patch area with an increase in θ. The increase in patch area flattens at higher θ. The inset shows a plot of the percentage patch area modified as a function of monolayer orientation, α, at various θ. At lower angles of incidence (e.g., $\theta = 2°$), the change in the Au patch area is significant with the change in the monolayer orientation. The patch area varies from 3.7 % to 5.7 % as the monolayer orientation is varied in between 0° and 30°. At higher θ the change in the patch area with the monolayer orientation is negligible ($<$ 1 %). At lower θ, the shadow effect is dominant and thus, the monolayer orientation determines the Au patch area and geometry. As θ is increased, the shadow effect is diminished, which in turn makes the patch area independent of the monolayer orientation at high θ.

In summary, we are able to produce particles with patches as small as 3.7 $\pm$ 0.5 % of the total particle surface area employing the glancing angle deposition technique. We find that the geometry of the patch is dependent on the angle of incidence of the vapor, θ and the monolayer orientation, α. The following section describes the extension of GLAD to produce particles with multiple patches also referred to as "multifunctional patchy particles".

3.2 Multifunctional patchy particles by GLAD

Patchy particles with a well-defined patch size and shape, are produced successfully by changing the angle of the vapor deposition as described in the previous section. The GLAD technique is further extended to produce "multifunctional patchy particles" or particles with unique patches. A particle stamping technique is developed to gain access to the entire particle surface, which allows fabricating patchy particles with patches on either side of the particle surface. The flexibility of GLAD in combination with the particle stamping technique lies in producing particles with variable patch sizes, patch shapes, and respective patch orientations on the particle surface. Figure 3.6 shows a schematic of single patchy particles and multifunctional patchy particles with patches on opposite poles and on the same hemisphere that can be fabricated by sequential vapor deposition. The previously mentioned computational model is extended to verify the patch geometries and relative patch orientations for the multifunctional patchy particles. The patch area calculations based on the patch geometries obtained from our computational model are used to decide on the experimental conditions needed to produce particles with the desired type of functionality.

3.2.1 Sequential multiple vapor depositions

Patchy particles with multiple patches on the same hemisphere of a particle are produced by sequential vapor depositions on a close-packed monolayer of colloids. The schematic of the sequential vapor depositions is shown in Figure 3.7. After the first vapor deposition (right arrow), the second vapor deposition is carried out from a different direction. The angle between the two vapor depositions is labeled as ξ and Figure 3.7 shows two examples of (a) $\xi = 180^\circ$ and (b) $\xi = 60^\circ$. For the second vapor deposition at $\xi = 180^\circ$ (Figure 3.7(a)), the glass slide is simply turned upside down,

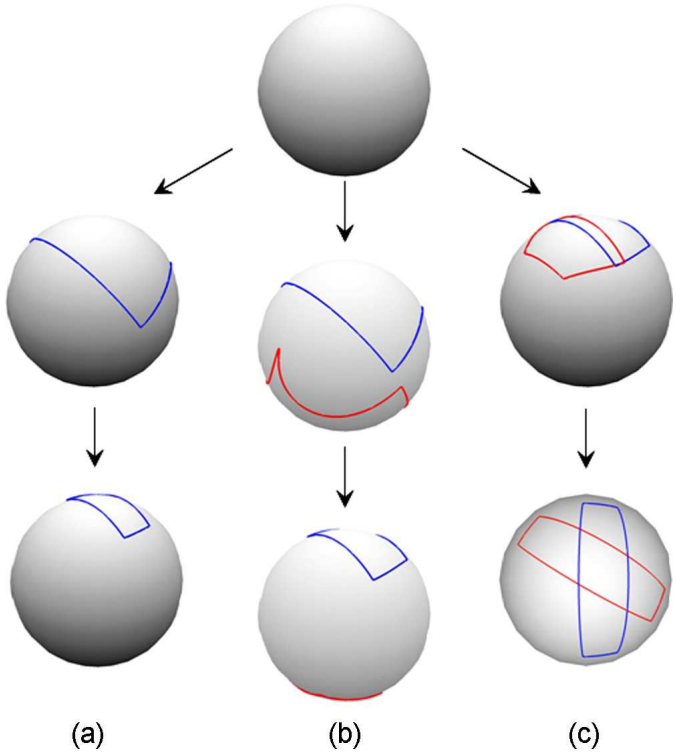

Figure 3.6: Schematic of patchy particles with (a) single patch, and (b) and (c) multifunctional patchy particles with patches on opposite poles and on the same hemisphere, respectively.

which rotates the monolayer by 180°. For other desired angles between the sources, the sample is rotated by the desired angle and is mounted on a new glass slide. The dark grey spheres in Figure 3.7 represent the spheres involved in the shadow effect for the patch on the representative particle during GLAD. The thickness of the patches is $\sim$ 20 nm measured during the deposition by a quartz crystal microbalance mounted in the evaporator. Following the evaporation, the samples are imaged using a variable pressure (vp) scanning electron microscope (EVO40 Zeiss).

The mathematical model described in the previous section is extended to predict the patch geometries of the multifunctional patchy particles produced as a result of sequential vapor depositions using the solutions for the single-patch case. When the source is rotated by the angle ξ for the second vapor deposition (Figure 3.7), the particles in a domain with a monolayer orientation of α experience a change of the

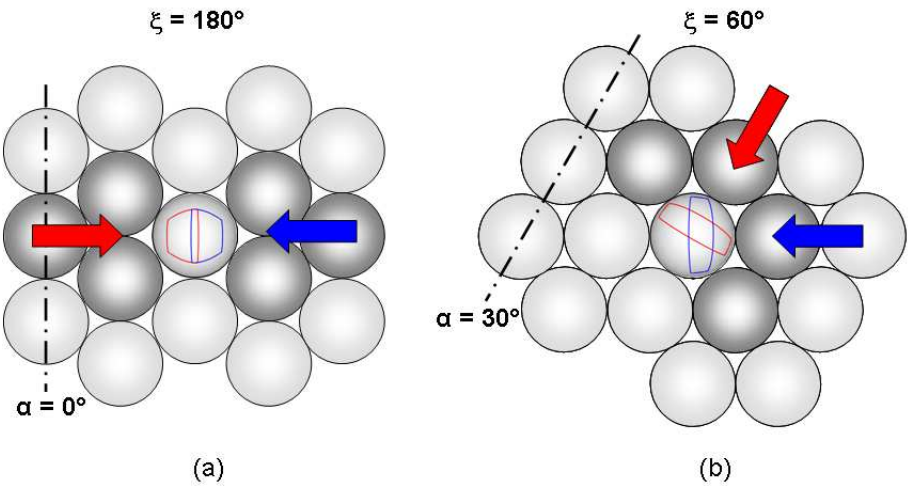

Figure 3.7: Schematic top view of particle monolayer during sequential vapor depositions. (a) Sequential vapor depositions at $\xi = 180°$, and (b) $\xi = 60°$. The blue and red arrows represent the direction of the vapor depositions with the resulting patch geometries shown on a single particle. Patch geometries correspond to patches obtained at a vapor deposition angle ($\theta = 5°$) for both sequential depositions and monolayer orientations of (a) $\alpha = 0°$, and (b) $\alpha = 30°$. The dark grey spheres are the representative spheres associated in the shadowing effect for the patchy particle shown.

monolayer orientation to $\acute{\alpha}$ where $\acute{\alpha} = \alpha + \xi$. The orientation of the patches obtained in the second vapor deposition is predicted by the mathematical model by rotating the patch geometry corresponding to the monolayer orientation $\acute{\alpha}$ on the particle surface by the angle ξ with respect to the first patch. Placement of both patches on the surface leads to overlapping patches. The predicted patch geometries are used to calculate the overlapping area of the patches. It should be noted that due to the hexagonal symmetry of the particles, the monolayer orientation repeats itself every 60°. Thus, any monolayer orientation can be represented by a value between 0° and 60° as (α - (60 × n)) where n = 0,1,2 and $\alpha \geq$ (60 × n).

Figure 3.8 shows a monolayer of patchy particles fabricated with GLAD carrying two patches. Figures 3.8(a) and (b) show 2.4 μm colloids modified with silver (left patch) and gold (right patch). The angle between the silver and the gold vapor deposition is ξ= 180°. The vapor deposition angle (θ) is set to 5°, which leads to gold and silver patches covering $\sim$ 8 % of the particle surface. The monolayer orientations

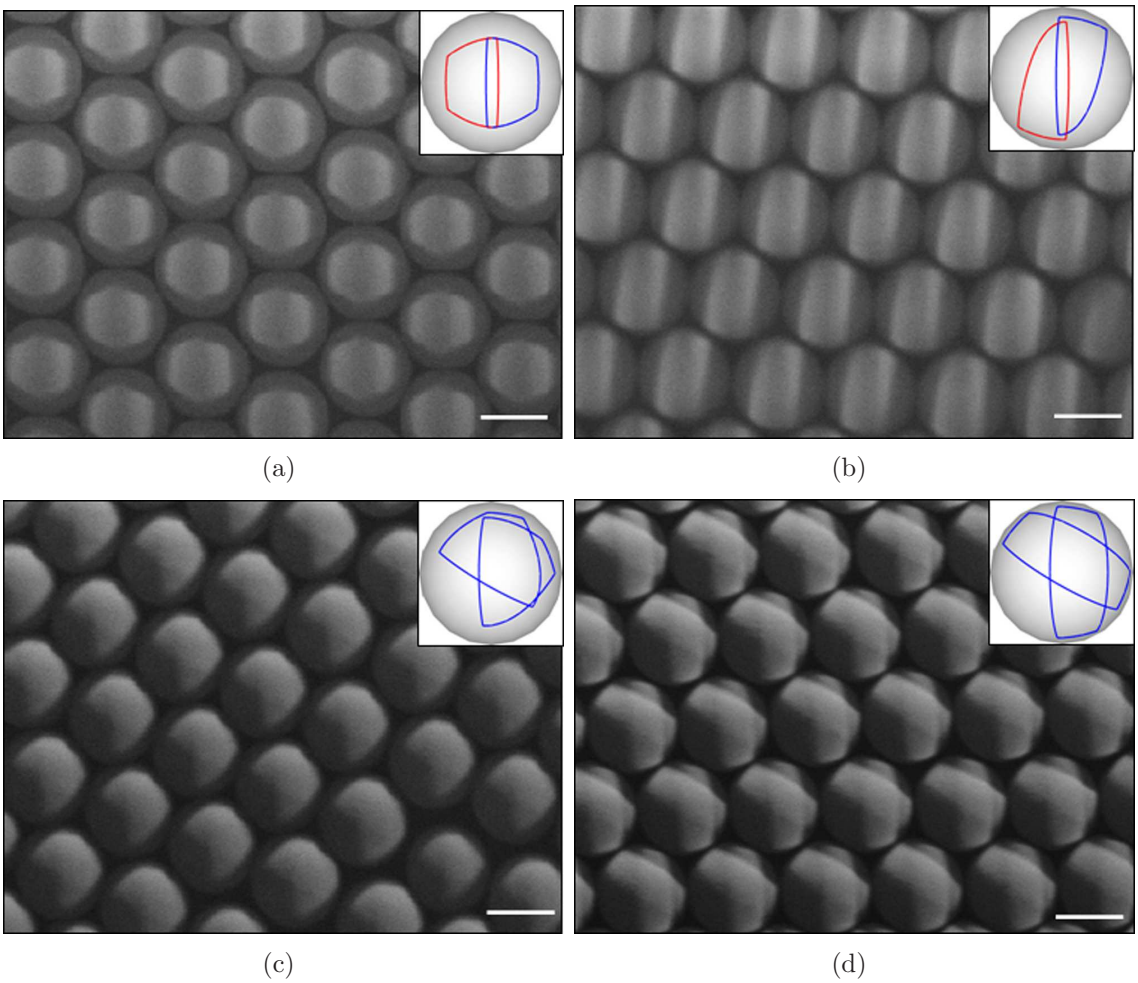

Figure 3.8: SEM images of the multi-functional patchy particles obtained by sequential vapor depositions at an angle of $\xi = 180°$ (a and b) and $\xi = 60°$(c and d) between vapor depositions. (a) and (b) are images of particles with a gold (right) and a silver (left) patch, at a vapor deposition angle of $\theta = 5°$ and monolayer orientations of $\alpha = 0°$ and $35°$, respectively. The insets are images obtained with the mathematical model with the red patch corresponding to silver and the blue patch corresponding to the gold patch. (c) and (d) are multifunctional patchy particles with two gold patches with $\theta = 10°$ while $\alpha = 53°$ and $30°$, respectively. The insets are the patch geometries obtained with the mathematical model. Scale bar is 2 μm.

$\alpha = 0°$ and $35°$ are represented in Figure 3.8(a) and (b), respectively. The insets show the patch geometries obtained using the mathematical model with variables (θ, α, and ξ) identical to the parameters used in the experimental deposition. The patch with the red boundary (left patch) corresponds to the silver patch, while the blue boundary (right patch) corresponds to the gold patch. Note, the two-dimensionality of the SEM image makes the patches appear to cover more than 8 % of the particle surface, but the mathematical models shown for a single particle in the insets of Figures 3.8(a) and (b) confirm a patch size of $\sim$ 8 % of the particle surface. Figures 3.8(c) and (d) show the patch geometries obtained when the angle between the two sequential gold depositions, ξ, is $60°$ and the vapor deposition angle, θ, is $10°$, which results in patches covering $\sim$ 11 - 12 % of the particle surface. Two different monolayer orientations ($\alpha = 53°$ and $30°$) are shown in Figures 3.8(c) and (d), respectively. The insets show the patch geometries obtained using the mathematical model.

As seen in the SEM images (Figure 3.8) and more clearly visualized in the mathematically calculated patch geometries (insets), the two patches on individual particles overlap with each other. The extent of the overlap varies with the monolayer orientation, α, as well as the angle between successive vapor depositions, ξ. The area of overlap between the patches is calculated numerically from the patch geometries obtained by the mathematical model and is $\sim$ 1.7 % of the particle surface for the particles depicted in Figure 3.8(a) and $\sim$ 7.6 % for the particles in Figure 3.8(c).

The degree of the patch overlap can be manipulated by controlling the angle of vapor deposition (θ) and the angle between the vapor depositions (ξ). While GLAD cannot produce particles with separate patches on the same hemisphere, the controlled degree of overlap of the patches gives a new engineering dimension. For example, in cases where both patches are metallic such as gold and silver patches, the overlap between the patches can be used to achieve electrical connectivity between the patches. Due to the possible electron transport from one patch to the other, the

electrically connected patches can be employed as, for example, autonomously moving particles (colloidal motors) in solvents. Such an autonomous motion of electrically connected doublets of gold and silver particles in hydrogen peroxide solution has been demonstrated elsewhere.[76] The overlap between the two patches is calculated to be as small as $\sim$ 1.7 % of the particle surface (overlapping area in Figure 3.8(a)) and increases quadratically between $\theta = 5^\circ$ and 20° and linearly afterwards between $\theta = 20^\circ$ and 80°, to as high as 44.5 % at $\theta = 80^\circ$. Eventually the patches will overlap completely and cover 50 % of the particle at $\theta = 90^\circ$. The overlapping area between the patches can also be used to form an alloy, which could then act as a third patch separating the left patch from the right patch. For example, the 1.7 % overlapping area separates and reduces the two individual gold and silver patches from 8 % to 6.3 % of the particle surface. It should be noted that during multiple vapor depositions, the patches produced from the initial vapor deposition may act as an additional shadow mask during subsequent vapor depositions. The shadow effect of the patch can be neglected in the examples reported here because the patch thickness ($\sim$20 nm) used is much smaller than the actual particle size (2.4 μm) and no more than two overlapping patches are deposited.

3.2.2 Two-pole patchy particles by particle stamping

Multi-functional patchy particles with patches on opposite poles are produced by vapor deposition on the inverted monolayer of particles with a single patch.

The schematic of the technique is shown in Figure 3.9. After the first vapor deposition (Figure 3.9(a)), the close-packed monolayer of particles with one patch is inverted using a PDMS stamp (Figures 3.9(b) and (c)). The second vapor deposition is performed on the inverted monolayer of particles (Figure 3.9(d)) leading to particles with patches on opposite poles. Patchy particles resulting from a second vapor deposition on the inverted monolayer at $\xi = 180^\circ$ are schematically shown in Figure

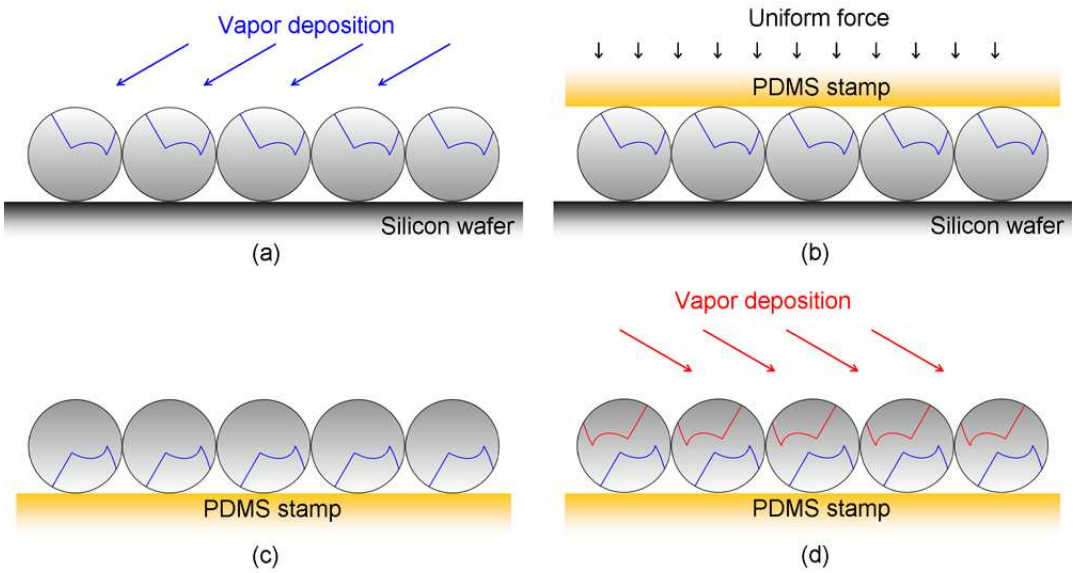

Figure 3.9: Cross-sectional schematic of the GLAD and particle stamping technique. (a) Close-packed particle monolayer obtained with GLAD at $\theta = 30°$ and $\alpha = 30°$. The blue lines on the particles are the patch boundaries obtained by the mathematical model. (b) Schematic of the patchy-particle monolayer being stamped with a uniform force by the PDMS stamp. (c) Inverted close-packed monolayer on the PDMS stamp with patches from the first vapor deposition facing down. (d) Second vapor deposition, leading to two-pole patchy particles at $\xi = 180°$.

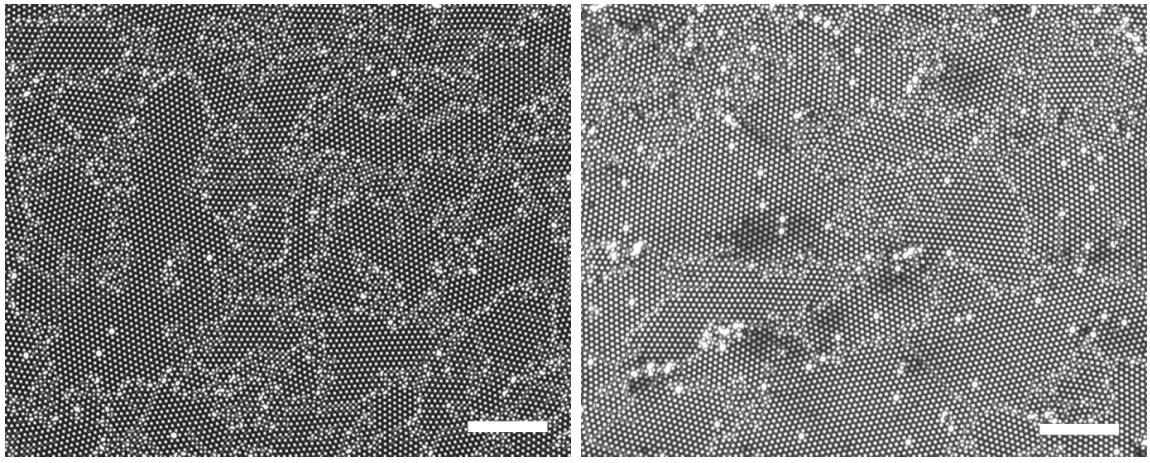

(a) (b)

Figure 3.10: Optical microscope images of 2.4 μm PS particles. (a) Close packed monolayer of particles on a glass slide before particle stamping. (b) Inverted particle monolayer on a PDMS stamp after particle stamping, schematically shown in Figure 3.9(c). Scale bar = 35 μm.

3.9.

The PDMS stamps for inverting the particle monolayer are produced by curing the elastomer and curing agent (10:1 w/w) (from Dow Corning) at 70° C in an oven overnight. In order to make PDMS stamps with flat surfaces, the viscous mixture of PDMS is poured onto a glass slide and precured for $\sim$ 25 minutes at 70° C. After 25 minutes the PDMS stamp is partially cured and viscous enough not to flow on the glass slide, but is still able to deform.[14] At this time another glass slide is placed on the precured PDMS stamp with a uniform force (100 $\sim$ 200 g/cm^2) and is left to cure at 70° C overnight. After curing the PDMS stamp, the top glass slide is removed leaving behind a flat PDMS stamp (2 $\sim$ 3 mm thick) sticking to the bottom glass slide. The top (flat) surface of the PDMS stamp is used for stamping the particle monolayer by applying a uniform pressure of $\sim$ 500 g/cm^2.

The close-packed monolayer of particles is accurately inverted with the particle stamping technique (Figure 3.10). Figure 3.10 shows representative optical transmission microscope images of a 2.4 μm PS latex particle monolayer on a glass slide before monolayer inversion (a) and after inversion with the PDMS stamp (b). The particles of the inverted monolayer in Figure 3.10(b) are deposited with a 25 % Au patch prior to the monolayer inversion. The features of the close-packed monolayer of particles before stamping such as grain boundaries between monolayer domains, point vacancies, and most importantly the hexagonal close-packing of particles in the domains are accurately transferred to the inverted monolayer on the PDMS stamp. The variation in image contrast of the point vacancies results from the different optical properties of the substrates used for imaging, i.e., a glass slide for Figure 3.10(a) and a PDMS stamp for Figure 3.10(b).

The second vapor deposition is performed on the inverted monolayer of particles on the PDMS stamp as discussed earlier and yields two-pole patchy particles. The modified particles are re-dispersed in water by sonicating the PDMS stamp for $\sim$

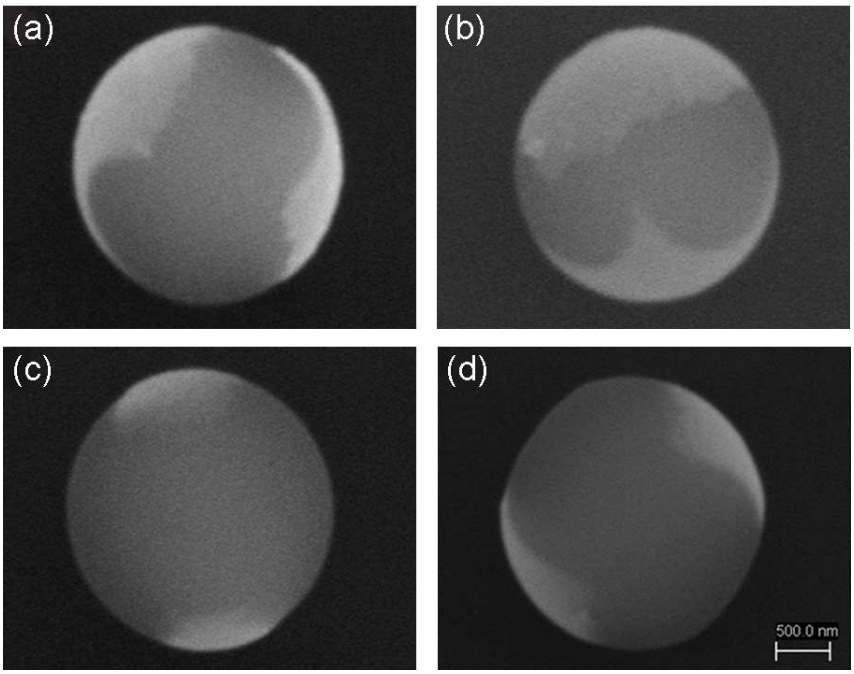

Figure 3.11: SEM images of multi-functional two-pole patchy particles with gold patches on opposite poles. (a) and (b) are 2.5 μm PS particles with two patches, each patch covers $\sim$ 25 % of the particle surface. (c) and (d) are the images of 2.5 μm PS particles with two patches, each patch covers $\sim$ 11 % of the particle surface.

45 minutes in a 1 wt. % aqueous solution of Tween20 surfactant. The particles are washed several times with DI water to remove excess Tween20 surfactant by centrifuging the particle solution and replacing the supernatant solution with pure DI water. The samples for SEM imaging are prepared by drying a diluted ($<$ 1 % w/v) drop of particle solution on a silicon wafer.

The mathematical model is used to predict the geometries of patches obtained on two-pole patchy particles. The patch geometries due to a second vapor deposition on an inverted monolayer of particles are obtained by inverting and rotating the single patch geometry with respect to the first patch. The orientation of an inverted monolayer during the second vapor disposition changes from α to $\acute{\alpha}$ where $\acute{\alpha} = (60 - \alpha) + \xi$.

Figure 3.11 shows images of four representative patchy particles with patches on opposite poles (two-pole patchy particles) obtained using the particle stamping

method followed by GLAD. Figures 3.11(a) and (b) depict the images of 2.5 μm plain PS particles where each of the gold patches covers $\sim$ 25 % of the particle surface ($\theta = 30°$). Figures 3.11(c) and (d) are the images of 2.5 μm PS particles with each of the gold patches covering $\sim$ 11 % of the particle surface ($\theta = 10°$). For imaging of the two-pole patchy particles, a diluted drop of particle solution ($<$ 1 % w/v) is dried on a wafer. This low concentration of particles is used to avoid clustering and multilayers of particles caused by the convective assembly of particles because of immersion capillary forces during droplet drying.[77] Thus after drying the two-pole patchy particles are randomly oriented on the substrate wafer as seen in Figure 3.11. The leading and the lagging segments of the patch boundaries can be identified in the SEM images of the particles. The leading boundary (LDB) caused by the shadow effect of neighboring particles within the particle monolayer is sharp, whereas the lagging boundary (LGB) is diffuse due to the tangency of the metal vapor rays to the particles.

The particle stamping technique allows us to produce two-pole patchy particles, particles with two independent, non-overlapping patches. The accuracy of the stamping technique lies in efficiently inverting the close-packed particle monolayer and is evaluated by comparing the experimentally observed patch geometries of two-pole patchy particles with the mathematically predicted ones. The angle of vapor deposition, θ, the monolayer orientation, α, and the angle between the two depositions, ξ, are the essential parameters to obtain the mathematically modeled patch geometries for the two-pole patchy particles. The angles θ and ξ are known from the experimental conditions and from the assumption that the monolayer is accurately inverted. The random orientation of the individual particles prevents the identification of the exact monolayer orientation, α, the particles had in the original monolayer prior to removal from the PDMS stamp. Thus, α is guessed and fitted by overlaying of the modeled patch geometries with SEM images of fabricated two-

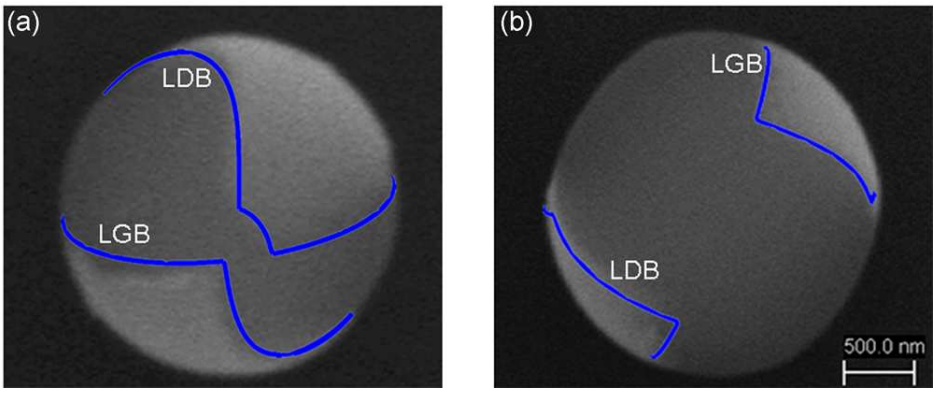

Figure 3.12: Mathematical predictions of patch orientations for two-pole patchy particles overlaid on two-pole patchy particles obtained experimentally. The mathematically obtained patch geometries are indicated by a solid line and are matched with the experimental patch geometries through manual rotation. The SEM images show two-pole patchy particles obtained from a deposition at (a) $\theta = 30^\circ$ and $\xi = 180^\circ$ and (b) $\theta = 10^\circ$ and $\xi = 180^\circ$. The respective mathematically modelled patch geometries are obtained with (a) $\theta = 30^\circ$, $\alpha = 15^\circ$, and $\xi = 180^\circ$ and (b) $\theta = 10^\circ$, $\alpha = 0^\circ$, and $\xi = 180^\circ$.

pole patchy particles. The diffusiveness and sharpness of patch boundary segments is used to distinguish between the lagging and the leading boundary of the individual patches in the SEM images. The orientation of the monolayer from which the particle originated is estimated by observing the symmetry of the leading boundary of the individual patches. Monolayer orientations of $\alpha = 0^\circ$ and $\alpha = 30^\circ$ always lead to symmetric leading boundaries and thus, individual patches of particles from 0° and 30° orientations are symmetric with respect to the axis passing through the center of the sphere, while the patch geometries of particles from all remaining monolayer orientations are asymmetric. The estimated monolayer orientation, α, of the first patch dictates the patch geometry calculated for the second patch. The orientation of the inverted monolayer ($\acute{\alpha}$) for the second vapor deposition at $\xi = 180^\circ$ does not change for $\alpha = 0^\circ$ and $\alpha = 30^\circ$ but changes to (60 - α)$^\circ$ for all other α values. The estimated monolayer orientation, α, with the resulting orientation of the inverted monolayer $\acute{\alpha}$ (assuming the monolayer is accurately inverted) is used to predict the geometries of the two-pole patchy particles mathematically. Figure 3.12 shows such a prediction from the mathematical model used on two representative two-pole

patchy particles. The mathematically obtained geometries of the patchy spheres are then rotated manually to match the orientations observed experimentally. If the experimental and the modeled spheres with patches cannot be matched, a new α is used in the mathematical model for calculating the first patch and the matching procedure is repeated. The accuracy of the predicted monolayer orientation obtained in this manner is $\pm$ 3° of α.

3.2.3 Summary

In summary, we have reported the fabrication of patchy particles with controllable patch size and shape employing the GLAD technique. Particles with a patch size as small as 3.7 % of the particle surface are fabricated. The experimentally observed patch geometries show good agreement with the mathematically predicted geometries. GLAD is further extended to produce multifunctional patchy particles with a controllable overlap of the patches. The particle stamping technique along with GLAD is used to fabricate patchy particles with patches on opposite poles. The experimental technique developed to produce patchy particles has a potential to produce a wide variety of patchy particles with easily controllable experimental parameters such as the angle of vapor deposition, the angle between successive vapor depositions, and the number of vapor depositions.

Chapter 4

Application of Patchy Particles

4.1 Dielectrophoretic assembly of patchy particles

This chapter demonstrates the directed assembly of patchy particles by application of external electric fields. The AC (Alternating Current) dielectrophoretic (DEP) assembly of patchy particles into a variety of 2D crystals is investigated. Patchy particles possess metallo-dielectric properties due to the presence of metallic (Au) patches on dielectric (PS) particles. The crystal structures assembled from these particles are strongly dependent on the dielectric properties of the particles used in the system. Thus, controlling the metallic and the dielectric properties of patchy particles can be implemented to direct their assembly into a variety of controlled, predefined structures. The metallo-dielectric properties of particles can be easily tuned by controlling the amount of metal patch on the particles. In the following, we show that as the size of the patch is varied from 50 %[17] to 25 % to 11 % of the particle surface, we can tune the DEP assembled crystal structure from staggered chains (50 %[17] and 25 %) with a variable chain width to network structures of particles (11 %). Further, we show that patchy particles with patches on opposite poles lead to the formation of a network of diagonal chains. This work is performed in collaboration with Mr. S. Gangwal and Dr. O. D. Velev at NC State University.

4.1.1 Introduction

The fabrication of 2D crystals or 3D structures of particles has been an area of interest for research in the past few years. Particle assembly can be directed into well-defined structures by external agents such as organic linker molecules or external fields such as electric or magnetic fields.[78–80] Application of an external electric field has the clear advantage that the experimental parameters such as intensity and frequency of the applied field can be easily varied. Thus, precise tuning of the forces exerted on the particles in a DEP experiment is achievable.

A suspension of dielectric particles when subjected to an external electric field, E_0, leads to polarization of the particles. For a dielectric particle suspended in a dielectric fluid, charge of opposite sign accumulates at either side of the particle when an electric field is applied. This charge separation gives rise to a dipole moment around the particle. The induced dipole moment of a spherical particle (radius r) in an electric field is dependent on the dielectric properties of the particle and the medium in which the particle is suspended and is given as[81]

$$p = 4\pi r^3 \varepsilon_1 \left\{ \frac{\tilde{\varepsilon_2} - \tilde{\varepsilon_1}}{\tilde{\varepsilon_2} + 2\tilde{\varepsilon_1}} \right\} E_0 \tag{4.1}$$

where subscripts 1 and 2 refer to medium and particle respectively. The *complex dielectric constant* ($\tilde{\varepsilon}$) is defined as

$$\tilde{\varepsilon} = \varepsilon + \frac{\sigma}{i\omega} \tag{4.2}$$

where $\omega = 2\pi f$ is the angular frequency of the external electric field, $i = \sqrt{-1}$, and σ is the conductivity. The significant characteristic of the complex dielectric constant is that it is frequency dependent (i.e., it contains an ω term). At higher frequencies ($\omega \to \infty$), the imaginary term vanishes and $\tilde{\varepsilon}$ is dominated by the permittivity, while

at lower frequencies ($\omega \to 0$), $\tilde{\varepsilon}$ is dominated by the conductivity. The bracketed term in Eq.(4.1) is called the Clausius-Mossotti factor ($\underline{K}$).

Colloidal particles when subjected to an external electric field experience electrokinetic phenomena due to the electrostatic interactions of the particles with the environment. The well-known electrokinetic phenomena, *electrophoresis*, is produced as an effect of the force exerted on a charged particle due to the attraction between the electrodes and the charged particle. Another important electrokinetic force, known as *dielectrophoresis*, is the force exerted on particles due to a non-uniform electric field. Application of an AC electric field across a colloidal suspension is the most commonly used technique to manipulate particles since in an AC electric field, particles are not directly attracted towards the electrodes as the sign of the electrode polarization is changing continuously. The induced dipoles within the particles interact with the non-uniform external electric field, which results in a dielectrophoretic (DEP) force acting on them. The exerted DEP force is proportional to the gradient of the field square, $\nabla \mathrm{E}^2$, and is given as:

$$F = (p \cdot \nabla)E \tag{4.3}$$

where p is the dipole moment given by Eq.(4.1). Thus the DEP force can be expressed as:

$$F_{DEP} = 2\pi r^3 \varepsilon_1 Re|\underline{K}(\omega)|\nabla E^2 \tag{4.4}$$

The sign and the magnitude of the polarizability of the particles is given by the real part of the Clausius-Mossotti factor, $\underline{K}$,

$$Re|\underline{K}| = \frac{\varepsilon_2 - \varepsilon_1}{\varepsilon_2 + 2\varepsilon_1} + \frac{3(\varepsilon_1\sigma_2 - \varepsilon_2\sigma_1)}{\tau_{MW}(\sigma_2 + 2\sigma_1)^2(1 + \omega^2\tau_{MW}^2)} \tag{4.5}$$

where ε_1 and σ_1 are the dielectric permittivity and conductivity of the medium

and ε_2 and σ_2 are that of the particle. τ_{MW} is the Maxwell-Wagner charge relaxation time. If the particles are more polarizable than the medium, they are attracted towards a region of maximum field intensity, which is referred to as positive DEP. On the other hand, if the particles are less polarizable than the medium, it is referred to as negative DEP. The polarizability of the particles and the medium is dependent on the field frequency. Thus, for a particle it is possible to experience either positive DEP or negative DEP depending on the frequency of the applied field.

The induced dipoles within the particles not only interact with the external electric field but also interact with other induced dipoles of neighboring particles. The interaction between the induced dipoles results in an attractive chaining force given as:

$$F_{chain} = -C\pi\varepsilon_1 r^2 K^2 E^2 \tag{4.6}$$

The chaining force is always attractive and positive. The attractive chaining force leads to the assembly of dielectric particles into chains. The chains attract each other (attractive force between chains) leading to 2D crystals of the particles with hexagonal close packing.

The assembly of particles in an AC electric field is controlled by physical parameters such as field strength and field frequency. Apart from these external forcing parameters, the intrinsic dielectric properties of patchy particles play an important role in governing the assembly. The phenomenon of the assembly of metallo-dielectric patchy particles in AC electric fields is more complex than that of regular plain particles, as patchy particles have both metallic and dielectric properties. Assembly of patchy, metallo-dielectrophoretic particles into staggered chains and network structures is reported and the proposed model is discussed in the section following the experimental results.

4.1.2 Experimental Setup for the DEP assembly

The schematic of the DEP experimental cell is shown in Figure 4.1. The cell consists of two co-planar gold electrodes deposited on the same side of a glass slide. The width between the two electrodes is $\sim$ 2 - 3 mm. The gold electrodes are deposited on a glass slide in a metal evaporator (Cressington 308 R, Ted Pella, Inc.). A thin titanium layer (4 - 6 nm) is deposited prior to gold deposition as an adhesion layer. The thickness of the gold electrodes is $\sim$ 80 nm. The glass slide is precleaned with sulfuric acid and Nochromix solution prior to use. A liquid blocker pen marker is used to draw a hydrophobic spacer well on the electrodes. The well is drawn such that it covers $\sim$ 1 cm^2 area. A concentrated drop (2 - 3 μl) of patchy particle solution in water is placed inside the well. The concentration of the suspension is adjusted to cover the entire well-area with a particle monolayer. A glass coverslip is then directly placed onto the suspension spreading the drop inside the hydrophobic well.

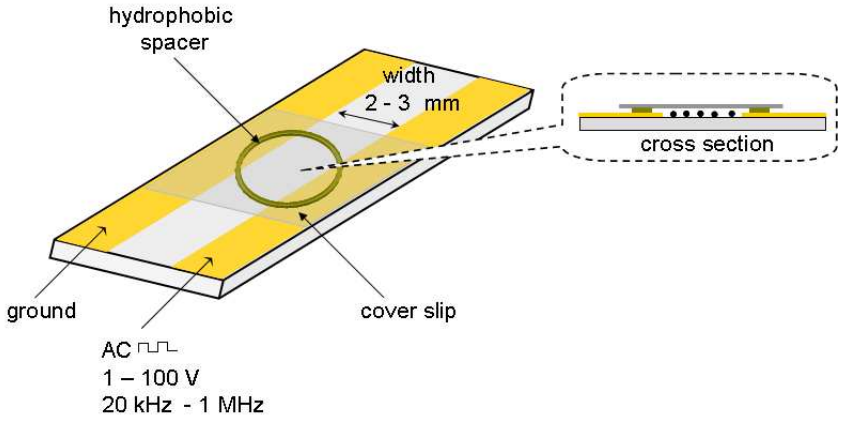

Figure 4.1: Schematic of the experimental cell for DEP experiments with cross sectional view.

An alternating electric field is generated by an Agilent 33220A function generator, which can generate a square waveform up to 20 MHz and is connected to a high voltage amplifier (Tegam-2350). For our experiments, alternating electric fields varying from 20 V to 100 V and frequencies from 20 kHz to 1 MHz are applied to the particle suspension. The assembly of particles is observed using an Olympus microscope BX

51 and the images are recorded by a u-eye camera model 2240c, which is mounted on the microscope. A suspension of patchy particles, with gold patches covering 50 %, 25 %, and 11 % of particle surface are used for the DEP experiments.

4.1.3 DEP assembly of patchy particles

This subsection describes the experimental results of the DEP assembly of patchy PS particles with 50 %, 25 %, and 11% gold caps. First, the assemblies observed for different types of particles are presented. Then, a unifying model for the observed assemblies is discussed.

Staggered chains of Janus (50 % gold-coated) particles Dielectrophoretic assembly of Janus particles into staggered chains and 2D metallo-dielectric crystals has been previously reported by Gangwal and Velev.[17] For our experiments with patchy particles, we first reproduced the results obtained with the Janus particles and then moved on to the patchy particles. Figure 4.2 shows the assembly of Janus particles in staggered chains at low particle concentrations (Fig. 4.2(a)) and 2D crystals at higher particle concentrations (Fig. 4.2(b)). The assembly of staggered chains is verified for two different sizes of particles 5 μm and 2.4 μm, respectively. The assembly of Janus particles into staggered chains is described in detail by Velev et.al.[17] and a brief description is given here.

When subjected to an AC electric field, the metallic (gold) half of a Janus particle is infinitely polarized as compared to the bare polystyrene half. In an electric field Janus particles orient in such a way that the plane between the gold and the polystyrene section is parallel to the external electric field (for schematic see Figure 4.7). This orientation of Janus particles is preferred as it leads to the largest induced dipole moment in the direction of the electric field. Such a preferred orientation of Janus particles is understood by the minimum energy of such orientations over the

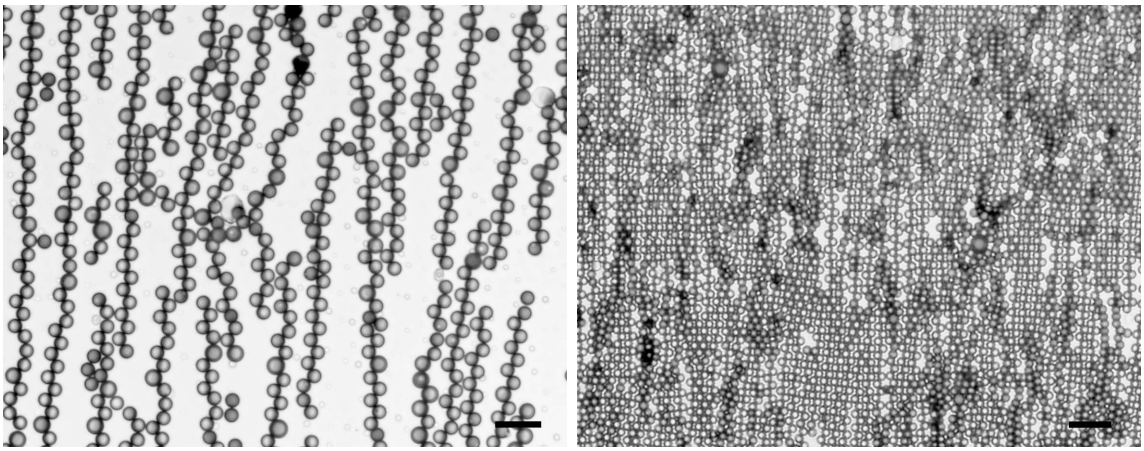

(a) (b)

Figure 4.2: Optical microscope images of (a) staggered chains of 5 μm Janus particles in an AC electric field of 14.67 Vcm^{-1} and 75 kHz, and (b) 2D metallo-dielectric crystal of 2.4 μm Janus particles in an AC electric field of 23.33 Vcm^{-1} and 150 kHz. The direction of the electric field is from top to bottom and the scale bars are 20 μm.

other orientations in simulations.[17] Once the preferred orientation of the particles is established, the double stranded chains of Janus particles are assembled in such a way that the gold caps are in contact with each other and the polystyrene halves of the particles are facing outward. Such an assembly of staggered chains is depicted in Figure 4.2(a). In optical images, the gold caps of particles in contact with each other can be identified as a lane of black gold lines along the chain in the direction of the applied electric field. Increasing the particle concentration in the experimental cell leads to 2D crystals of Janus particles (Figure 4.2(b)). Such a behavior of Janus particles in an AC electric fields is observed at higher frequencies ($>$ 10 kHz) and at electric field strengths of 1 - 100 Vcm^{-1}. At lower frequencies either straight chains of particles or motion of Janus particles perpendicular to the electric field due to ICEP (Induced Charge electrophoresis) are observed.[58]

Staggered chain assembly of 25 % gold-coated patchy particles Dielectrophoretic assembly of 25 % gold-coated patchy particles leads to the formation of staggered chains and 2D metallo-dielectric crystals (Figure 4.3) similar to the behavior

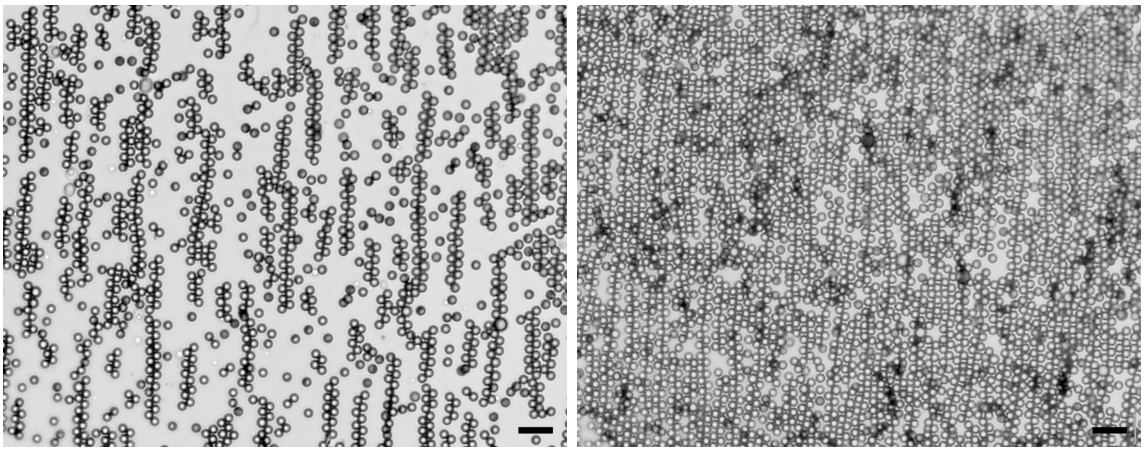

(a) (b)

Figure 4.3: Optical microscope images of (a) staggered chains of 2.4 μm patchy particles (25 %) in an AC electric field of 33.33 Vcm^{-1} and 175 kHz and (b) 2D metallo-dielectric crystal of 2.4 μm Janus particles in an AC electric field of 66.66 Vcm^{-1} and 75 kHz. The direction of the electric field is from top to bottom and the scale bars are 10 μm.

observed for Janus particles. Lower concentrations of particles lead to staggered chains of 25 % gold-coated patchy particles and increasing the particle concentration leads to 2D crystals. The orientations of the gold caps of the patchy particles is similar to that found for Janus particles, i.e., the particles are oriented such that the caps are oriented perpendicular to the direction of the electric field. The staggered chains are assembled in a way to form a gold lane of caps along the chain. A higher concentration of particles (Fig. 4.3(b)) assembles the staggered chains into 2D crystals of patchy particles.

Analysis of staggered chains obtained using 50 % (Janus) and 25 % patchy particles, reveals the difference between the two configurations. Figure 4.4 shows two exemplary staggered chains and the schematic of assembled Janus and 25 % gold-coated patchy particles. Although the chains are assembled in a similar arrangement with respect to the gold caps, the width of two staggered chains varies between the two configurations. The width of the chains is determined to be $\sim$ (1.65 $\pm$ 0.5) D in case of Janus particles and $\sim$ (1.8 $\pm$ 0.5) D in case of 25 % gold-coated patchy particles (image analysis of 10 - 15 chains). When subjected to an AC electric field,

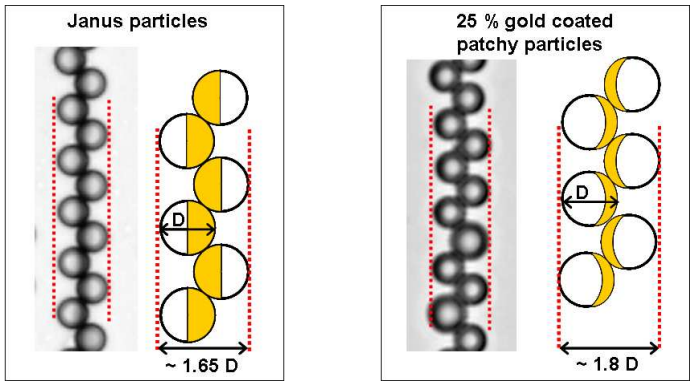

(a) (b)

Figure 4.4: Optical microscope images and schematics of staggered chains of 5 μm (a) Janus particles and (b) 25 % gold-coated patchy particles in an AC electric field. The direction of the electric field is from top to bottom and D is the particle diameter.

metallo-dielectric patchy particles are polarized. The gold-coated part of particles is infinitely polarized compared to the remaining dielectric polystyrene particle. The assembly of the patchy particles into staggered chains is governed by the infinitely polarized gold-coated part of the particles. The Janus/patchy particles assemble in such a way that the largest dipole (inside the gold cap) is aligned in the direction of the applied electric field. As a result, staggered chains with a conductive central lane of gold caps are formed in the direction of the electric field.[17]

In the case of a 25 % gold-coated patchy particle, the portion of the particle having a gold cap is concentrated towards the pole rather than extending towards the equator of the particle as is the case for a Janus particle. Thus, the largest dipole induced within the gold-coated part of the particle is concentrated at the gold-capped pole. Concentration of the dipole at the particle pole, leads to an increase of the chain width of the staggered chain formed by 25 % gold-coated patchy particles to enable the dipole alignment in the direction of the electric field while allowing the gold caps to touch each other for formation of a conductive lane along the center of the staggered chains.

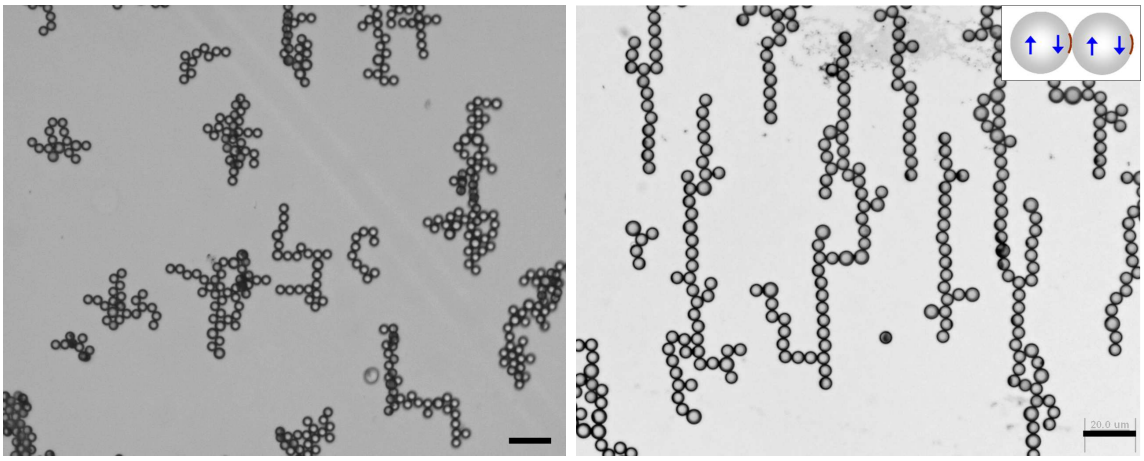

(a) (b)

Figure 4.5: Optical microscope images of (a) horizontal and vertical chains of 11 % gold-coated 5 μm patchy particles in an AC electric field of $\sim$ 50 Vcm^{-1} and 500 kHz and (b)* Network structure of 11 % gold coated particles at $\sim$ 30 Vcm^{-1} and 400 kHz. The direction of the electric field is from top to bottom and the scale bars are 20 μm. (* obtained from Gangwal from Expts. done at NCSU)

DEP assembly of 11 % gold-coated patchy particles DEP assembly of 50 % (Janus) and 25 % gold-coated patchy particles leads to staggered chains and 2D metallo-dielectric crystals of patchy particles. Further reduction of the patch size to 11 % of the particle surface leads to the assembly of such particles into chains vertical and horizontal to the external electric field. Figure 4.5(a) shows such vertical and horizontal chains assembled with the 11 % gold-coated 5 μm PS particles in an AC electric field of $\sim$ 50 Vcm^{-1} and 500 kHz. A few staggered chains of particles are also observed in addition to the vertical and horizontal chains. The vertical and horizontal chains connect to each other to form a 2D network structure of particles (Figure 4.5(b)). The orientation of the gold patches of the particles in the horizontal or vertical chains can not be determined from the optical microscope images. However, preliminary experiments with instantaneous field removal show rotation of particles, which hints at a patchy particle orientation where the gold patches are aligned in the horizontal direction of the chains. This observation of patch orientation is in good agreement with the FEMLAB calculations of a stationary particle orientation

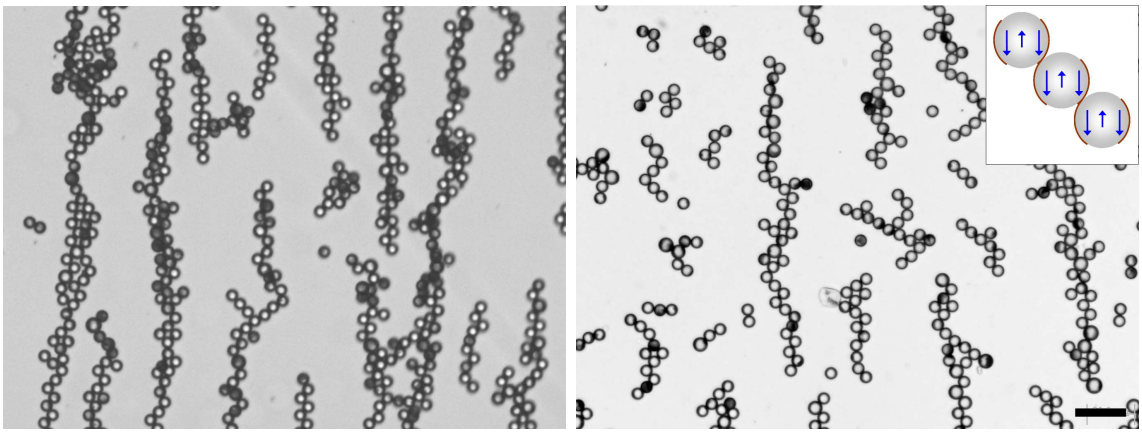

(a) (b)

Figure 4.6: Optical microscope images of diagonal chains of two-pole patchy particles in an AC electric field of (a) $\sim$ 40 Vcm^{-1} and 400 kHz and (b)* $\sim$ 30 Vcm^{-1} and 400 kHz. Inset shows schematic of the two-patch particle assembly. The direction of electric field is from top to bottom and the scale bars are 20 μm. (* obtained from Gangwal from Expts. done at NCSU)

performed by our NCSU collaborators.

DEP assembly of patchy particles with patches on opposite poles. Patchy particles with two patches on opposite poles are prepared as mentioned in Chapter 3. The dielectrophoretic assembly of two-pole patchy particles with patches of $\sim$ 25 % of the particle surface is shown in Figure 4.6. The two-pole patchy particles assemble into diagonal chains.

The schematic of the DEP assembly of two-pole patchy particles is shown as an inset in Figure 4.6(b). As indicated in the schematic, the gold caps on the poles are infinitely polarized compared to the bare polystyrene particle core. At higher frequencies, the dipoles in the caps are oriented in the direction of the electric field, while the dipoles within the PS cores experience negative DEP and are oriented in the opposite direction. Thus, the infinitely polarized gold caps control the assembly of the two-pole patchy particles. Similar to the Janus and 25 % patchy particle case, the two-pole patchy particles are assembled in such a way that the dipoles within the gold caps are aligned and connected, leading to the assembly of diagonal chains.

4.1.4 Discussion

In order to understand the differences between the assembly behavior of different kinds of patchy particles, it is important to understand the frequency dependence of the DEP force for dielectric particles.

The sulfate terminated latex particles have ionizable sulfate (SO_4^-) groups on their surface. In an electrolyte (e.g., water), at neutral pH these groups are negatively charged and in order to maintain the charge neutrality, ions of opposite charge (+ ve) are attracted to the particle surface forming a thin layer of counter ions, which is called a *double layer*. The double layer is composed of a *bound* or *stern* layer and a *diffuse* layer. In the presence of an external electric field, the charges in the *bound* layer move around the particle towards the opposite electrode and accumulate at the interface between the particle and the bulk electrolyte. However, the ions in the outside diffuse layer can exchange with the bulk, attempting to maintain the electroneutrality by accumulating on the other side of the particle. Thus, the induced dipole moment at lower field frequencies is attributed to the polarization of the double layer.

Now, if the field direction is reversed, the induced dipole must reverse by the movement of mobile ions in the double layer. Following the application of the field the charges do not move instantaneously but the diffusion of charges has a characteristic time required for electro-migration, which is $O(l^2/D)$ where D is characteristic ion diffusivity. At low frequencies, the transport rates (movement of free charge) are fast relative to the external forcing by the alternating field. Thus, at low frequencies, the induced dipoles follow the imposed field exactly and are attributed to the polarized double layer. At higher frequencies, the ion transport can no longer match the frequency of the change in the direction of the imposed electric field. Thus, the free charge movement is no longer a dominant mechanism responsible for the charging at the interface, instead polarization of the bound charges (permittivity) dominates.

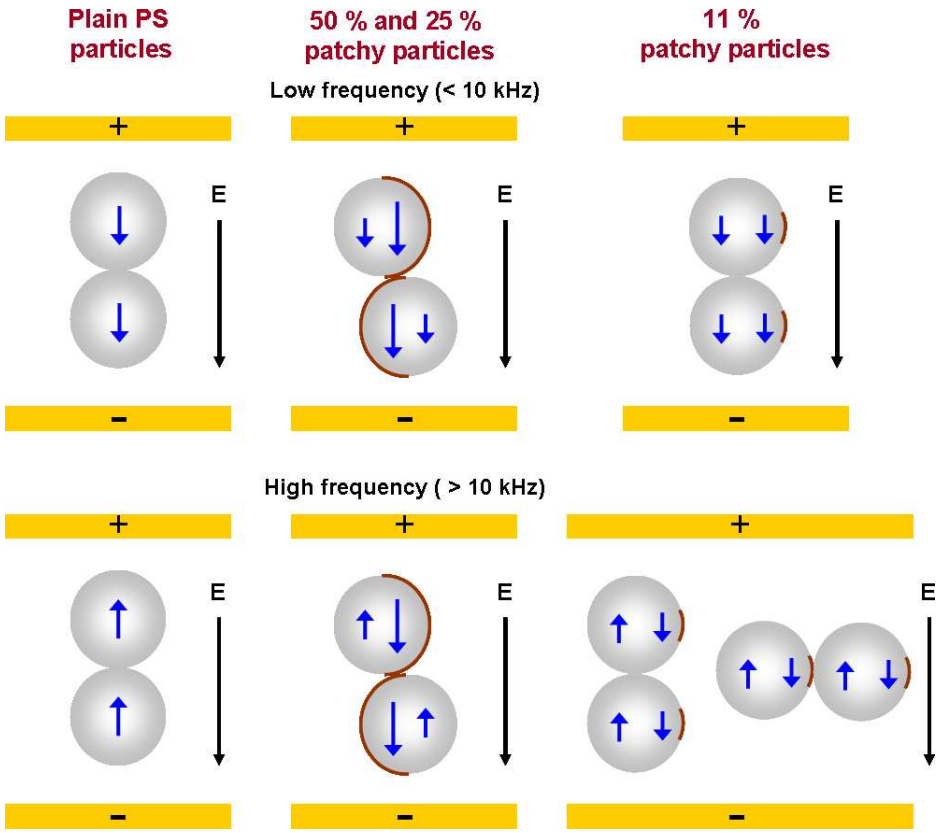

Figure 4.7: Proposed model for DEP assembly of (a) 50 %, (b)25 %, and (c) 11 % patchy particles in AC electric field at low and high frequency.

Because the dielectric constant of polystyrene (2.4 - 2.7) is much smaller than the dielectric constant of water (80 - 88 at 25°C), PS particles experience negative DEP, where the induced dipoles are aligned opposite to the direction of the external electric field.

Figure 4.7 depicts our proposed model for DEP assembly of patchy particles. Plain polystyrene particles experience positive DEP at low frequencies and then negative DEP at higher frequencies (Fig. 4.7(a)). The frequency at which the transition takes place is referred to as Maxwell-Wagner cross over frequency.[82,83] In the case of patchy particles, the gold-coated part of the metallo-dielectric polystyrene particles is infinitely polarized due to the free electron transport through the metal. Thus, the cross over frequency of the gold-coated half is well above the operating frequency range of the experiments. As a result the free electron transport in metals always dominates

the external forced switching of the AC electric field. At lower field frequencies, both the metal-coated and uncoated parts of patchy particles experience positive DEP, where the dipoles are oriented in the external field direction. However, at higher field frequencies the uncoated polystyrene part experiences negative DEP and the gold-coated part still experiences positive DEP. Owing to the fact that the induced dipole within the gold-coated part is larger than that of the PS part, the assembly of such particles is governed by the gold-coated portion of the spheres. As a result Janus (50 % coated) and 25 % gold-coated particles assemble into staggered chains to align the dipoles of their gold caps.

In order to understand the assembly of 11% gold-coated patchy particles into chains perpendicular to the direction of the external electric field, a review of DEP assembly of mixtures of particles experiencing positive (particles more polarizable) and negative (particles less polarizable) DEP is helpful. Figure 4.8 shows the electric field distribution for two different particles, one more polarizable (dark sphere) and the other less polarizable (white sphere) than the medium, when aligned along or perpendicular to the external field. Figure 4.8(a) suggests that the more polarizable particle is attracted to the high-field regions around the less polarizable particle, which are located at the poles along the axis perpendicular to the field direction. Similarly, the less polarizable particle is attracted to the low-field regions of the more polarizable particle, which are located at the poles perpendicular to the field direction. Thus, the assembly in Figure 4.8(a) represents an unstable configuration and the one in panel 4.8(b) is the stable configuration, which is in the direction perpendicular to the direction of the external field.[83] Note, the direction of the electric field is from left to right.

Such perpendicular chains have been observed experimentally by Giner et. al. in the mixture of particles.[84] Exactly the same mechanism is observed in the case of 11 % patchy particles, i.e., the particles behaves as “quadrapoles”. To minimize the field

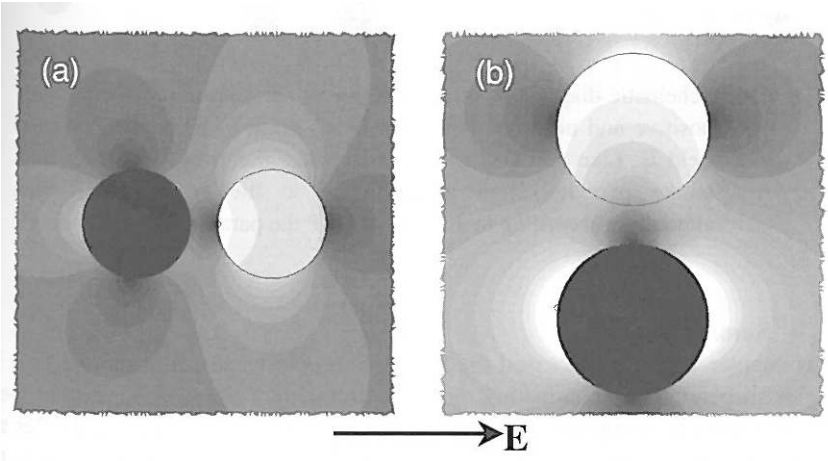

Figure 4.8: Magnitude of electric field around two particles, one more polarizable (dark) and the other less polarizable (light) than the medium. Particles aligned (a) parallel and (b) perpendicular to the field.[83]

potential, such quadrapoles assemble into vertical and horizontal chains as shown in Figure 4.7 and lead to a network structure of patchy particles. Apart from these structures simulations have also suggested that the staggered chains of 11 % patchy particles are the next favorable configurations at a slightly higher energy, which occurs due to aligning of gold-cap dipoles. The DEP assembly of two-pole patchy particles into diagonal chains can be explained in a similar fashion, where the two caps on the opposite poles of the particles are polarized infinitely. The two caps experience positive DEP at higher field frequencies, which leads to diagonal chains as shown schematically in the inset of Figure 4.6.

4.1.5 Summary

In this section we have presented the directed assembly of patchy particles in the presence of an external AC electric field. The dielectrophoretic assembly of patchy particles in AC electric fields is qualitatively different from that of plain polystyrene particles. The metallo-dielectric properties of the patchy particles lead to their assembly into unique crystal structures such as staggered chains or network structures, which are not accessible via regular plain PS particles.

The DEP assembly depends on physical parameters such as the field strength and the field frequency. Our studies indicate that the assembly can be controlled not only by these experimental conditions but also by controlling the metallo-dielectric properties, i.e., the patch size of the patchy particles. Janus particles (50 % patch) and 25% gold-coated patchy particles assemble into staggered chains with variable chain widths. Further reduction of the patch size to 11 % of particle surface leads to horizontal and vertical chains of particles and the formation of particle network structures. The assembly of patchy particles is explained by a simple theoretical model taking into account that the highly polarizable gold patches of the patchy particles govern the DEP particle assembly.

4.2 Patchy particles as osmotic motors

This chapter demonstrates an application of patchy particles as autonomously moving osmotic motors. The autonomous motion of polystyrene particles coated with platinum (Pt) patches in hydrogen peroxide (H_2O_2) solution is analyzed. The trajectories of the particles obtained from particle-tracking are used to determine the particle velocities. Our studies show that the velocity of particles can be controlled by varying the Pt patch-size on the particle surface. The particle velocity increases exponentially as the patch-size increases from 11 % to 25 % to 50 % of the particle surface. The particle motion is analyzed mathematically using a model proposed by Anderson et. al.,[85] which had been previously developed to study the motion of particles in a concentration gradient of non-electrolyte solutes. Our extended model solves the Stokes equation of flow analytically with an additional body force term generated by the concentration gradient due the surface reaction.

4.2.1 Motion of particles in chemical gradients

When a particle is placed in a fluid with a non-uniform solute concentration, the particle moves towards higher or lower concentration depending on the specific interaction of the solute with the particle. A detailed theoretical analysis of the motion of particles placed in a non-uniform solute concentration has been reported by Anderson.[63,85] The analysis solves the equations of mass and momentum balance in the vicinity of the particle.

The concentration gradient of the solute does not necessarily have to be imposed on the particle by the surrounding medium, but the particle itself can generate such a gradient through a reaction on part of its surface. Such a motion of particles caused by a solute gradient generated by the particle itself is also referred to as self-diffusiophoresis. Self-diffusiophoretic motion of Pt-Au nanorods[60,61] and Janus particles coated with 50 % Pt[45] has been reported recently. Various mechanisms such as an interfacial tension gradient,[60] a propulsion mechanism,[62] and an effective slip velocity model[86] have been proposed to explain the motion. Recently, Figueroa and Brady proposed an osmotic pressure model to explain the self-propulsion of colloidal particles immersed in a dispersion of bath particles.[87]

In our study, we analyze the motion of patchy particles with platinum patches in a 3 % (v/v) H_2O_2 solution. The effect of the patch size on the particle motion is studied for two particle sizes. The platinum patch covering a part of the particle surface decomposes hydrogen peroxide into water and oxygen, which generates a solute (H_2O_2) and O_2 gradient around the particle. The H_2O_2 concentration gradient leads to an imbalance of body force acting on the particle, resulting in their autonomous motion. The experimental study of the motion of patchy particle is reported in the next subsection. Following the experimental subsection, a mathematical model is presented, which has been developed to describe the autonomous motion of the particles.

4.2.2 Experimental details

Patchy particles (5 μm and 2.4 μm sulfate latex PS) with Pt patches covering 50 %, 25 %, and 11 % of the particle surface are fabricated using GLAD. After deposition, the particles are redispersed in DI water. The experimental cell for studying the particle motion is comprised of a glass slide and a silicone isolator well (Invitrogen Corp.). The silicone well (9 mm dia. and 0.5 mm depth) adheres to the precleaned glass slide with the help of an adhesive present on the well surface. 6 % (v/v) H_2O_2 solution is prepared from a stock solution of 30 % H_2O_2. For the experiments, 10 μl of the 6 % (v/v) H_2O_2 solution is mixed with the 10 μl of the patchy particle solution in the well, which results in a 3 % (v/v) or 4.3 % (w/v) H_2O_2 solution. The cell is covered with a cover slip to avoid any motion within the liquid due to air currents and to reduce evaporation.

The particle motion is observed using an Olympus BX-51 microscope with a $\times$20 objective and is recorded with a u-eye 2240c camera at a rate of 10 frames per second. A movie of 500 frames (50 s) is recorded for each particle. ImageJ software is used to adjust the contrast threshold of the frames obtained from the movie and to obtain the particle positions (x,y) in each frame. The particle trajectories (x,y,time) are then obtained using a modified Matlab program originally written by John C. Crocker. The trajectories of the particles are used to calculate the particle velocities. For each type of patchy particle, at least 15 separate particle trajectories are tracked and analyzed. Only the particles sitting in the proximity of the glass slide are used for the analysis. Particles in solution away from the glass surface cannot be tracked as their random motion takes them out of focus of the microscope hindering image analysis. Using the $\times$ 20 and $\times$ 50 objectives of the microscope, no evolution of oxygen bubbles is observed on the particle surface. After $\sim$ 10 minutes, oxygen bubbles of about 10 μm size are observed on the glass slide. Following the appearance of oxygen bubbles in the cell, the particle tracking is stopped as the particle motion might be affected

by the bubbles in the solution.

4.2.3 Analysis of particle motion by particle tracking

All the experiments of the particle tracking are performed at a fixed 4.3 % (w/v) H_2O_2 concentration. Figure 4.9 shows a representative overlay of optical microscope images at different time intervals ($\triangle$t = 10 s) representing the autonomous motion of 25 % Pt-coated 5 μm patchy particles in a 4.3 % (w/v) H_2O_2 solution. The autonomous motion of 5 μm and 2.4 μm Pt-coated patchy particles is studied varying the patch size from 50 % to 11%.

Figure 4.10 shows 50 s trajectories of four 2.4 μm particles as the patch size is varied from (a) 50 %, to (b) 25 %, to (c) 11 % of the particle surface. Figure 4.10(d) shows the trajectories of four particles without Pt modification exhibiting Brownian motion. The trajectories of the 4 particles per patch size shown in Fig. 4.10 are scaled to start from the same origin. The velocity of the particles is obtained by calculating the mean square displacement of the trajectories. The Brownian motion of a particle with a radius a shows a linear mean square displacement in time with the slope controlled by the diffusion coefficient, $D = k_BT/(6\pi\mu a)$, where μ is the viscosity and k_BT is the thermal energy.

The particles also undergo rotational diffusion with a rotational diffusion coefficient $\tau_R^{-1} = k_BT/(8\pi\mu a^3)$. Brownian diffusion is a completely random motion of particles. On the other hand, the motion observed in the case of patchy particles is a directional motion at small time scales and becomes random over time. A particle propelled with a velocity V leads to the coupling of rotational and translational diffusion. The 2D mean square displacement is given as,[45,88]

$$\Delta L^2 = 4D\Delta t + \frac{V^2\tau_R^2}{2}\left\{\frac{2\Delta t}{\tau_R} + e^{-2\Delta t/\tau_R} - 1\right\} \tag{4.7}$$

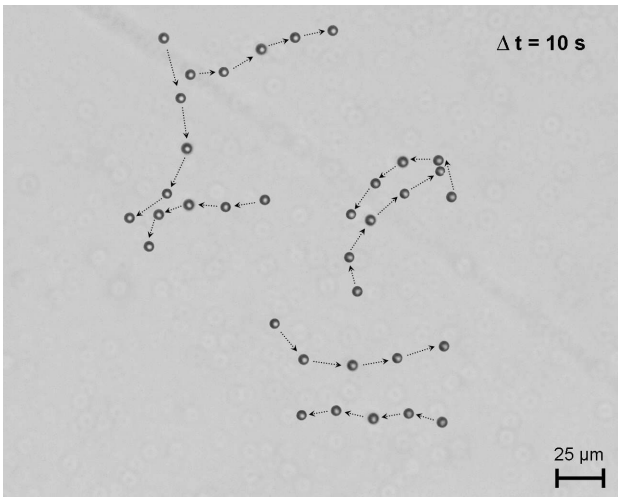

Figure 4.9: Overlay of optical microscope images from different frames (10 s time interval) of seven autonomously moving 5 μm PS particles coated with 25 % Pt. The displacement of particles between two subsequent frames is represented by arrows.

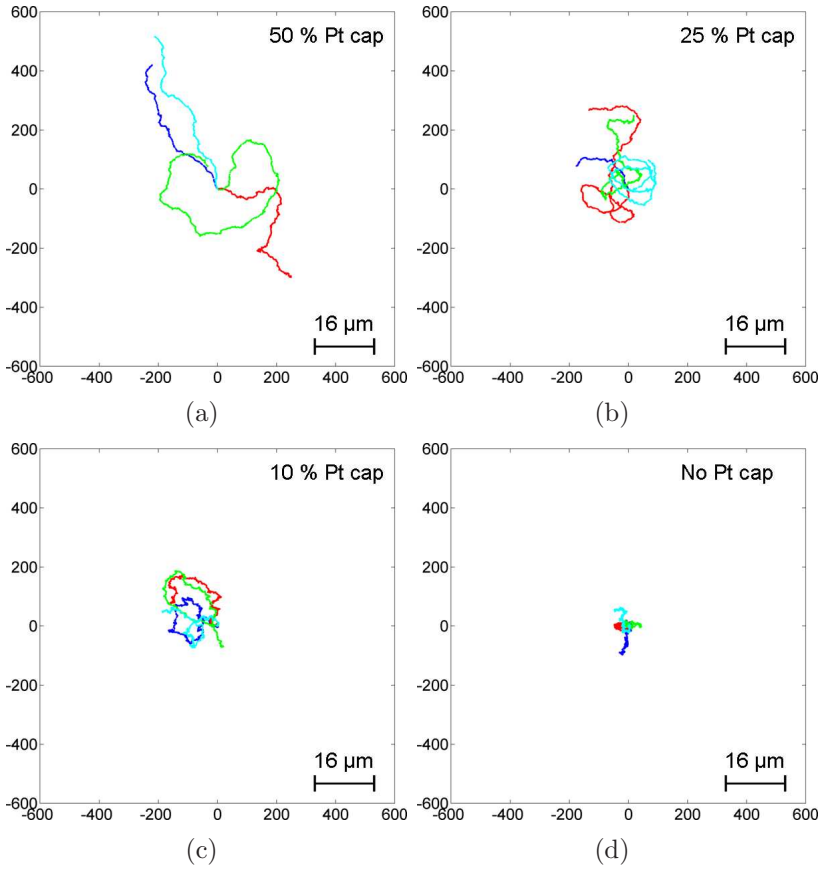

Figure 4.10: 50 s trajectories of four representative (a) 50 %, (b) 25 %, (c) 11 % Pt-coated and (d) unmodified 2.4 μm PS particles. The x and y axes represent a pixel scale with 200 pixels = 16 μm. Particle trajectories of different particles are differentiated by colors.

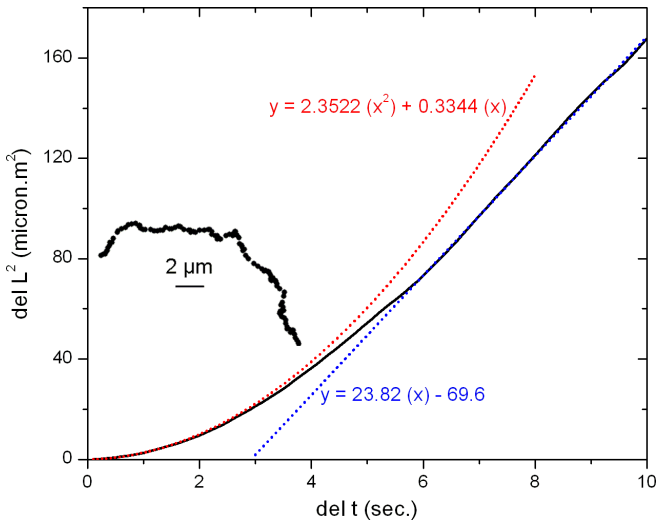

Figure 4.11: Mean squared displacement as a function of time for 25 % Pt-coated patchy particle with trajectory shown as the inset. The trajectory is fitted to Eq.(4.7), resembling a parabola (red dotted line) at $\Delta t << \tau_R$ and a straight line (blue dotted line) at $\Delta t >> \tau_R$.

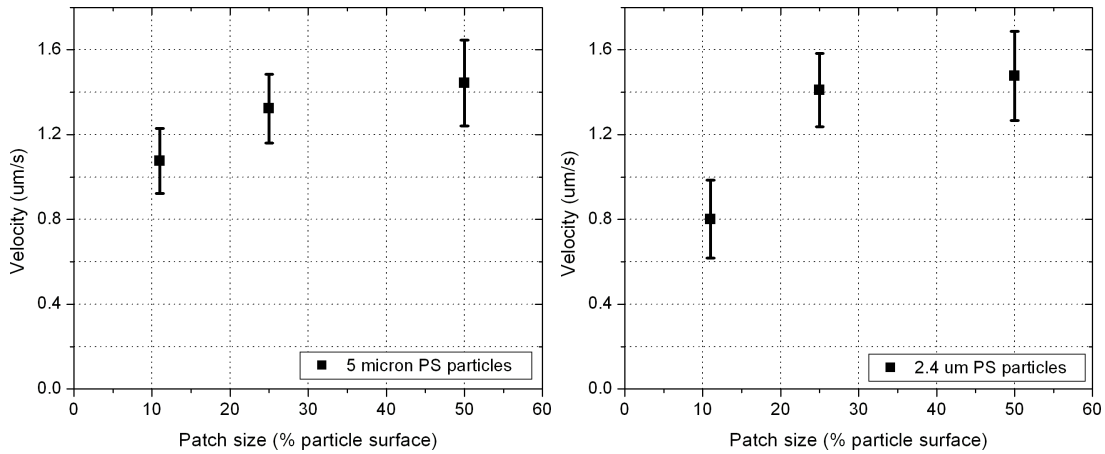

(a) (b)

Figure 4.12: Velocities of patchy (a) 5 μm, and (b) 2.4 μm PS particles determined from their $t << \tau_R$ behavior as a function of patch size (50 %, 25 %, and 11 % of the particle surface).

$$\Delta L^2 = 4D\Delta t + V^2\Delta t^2 \qquad \Delta t << \tau_R \tag{4.8}$$

$$\Delta L^2 = (4D\Delta + V^2\tau_R)\Delta t \qquad \Delta t >> \tau_R \tag{4.9}$$

The limiting forms of Eq.(4.7) indicate that at short times ($\Delta t << \tau_R$) the displacement is linear in time, while at higher times ($\Delta t >> \tau_R$) the displacement is

random with an effective diffusivity $D_{eff} = D + (1/4)V^2\tau_R$.[45] Figure 4.11 shows a plot of the mean square displacement of a 25 % Pt-coated 2.4 μm PS particle, as a function of time fitted to equations (4.8) and (4.9). The particle trajectory is shown in the inset. The parabolic nature of the plot during short times is explained by the propulsion due to the particle velocity V. The plot is fitted to determine $V, D_{particle}$, and τ_R. For each type of particle at least 15 particle trajectories are tracked and analyzed to find out the effect of the patch size on the particle velocity. Figure 4.12 shows the particle velocity plotted as a function of the patch size for (a) 5 μm and (b) 2.4 μm particles. The velocities represented in Fig. 4.12 are the average velocities obtained from 15 - 20 particles and the error bars indicate the standard deviation of the measured velocities. The velocity plots indicate that for both 5 μm and 2.4 μm PS particles the velocity increases with the patch size. The velocity behavior shows that as the patch size becomes larger and larger, the effect of the patch size on the velocity is diminished.

4.2.4 Autonomous particle motion due to a self-inflicted concentration gradient

Different possible hypotheses have been postulated to describe the motion of Janus particles including, models based on an interfacial tension gradient,[60] a slip velocity on the particle surface,[86] or an osmotic force propulsion.[87] Since oxygen bubbles are not observed on the platinum caps in our studies, we can neglect the interfacial tension gradient and describe the motion of the patchy particles based on the concentration gradient of the H_2O_2 solute. The sharp concentration gradient across the particle is generated due to the surface-catalyzed decomposition of H_2O_2 only on the part of the particle surface covered with platinum. The motion of the particles is attributed to an imbalance in the *body force* of H_2O_2 and O_2 around the particle. A comparable kind of particle motion caused by an imbalanced body force but in a linear concentration

gradient has been analyzed by Anderson et. al.[85] In our study, we have a non-linear H_2O_2 concentration profile around the patchy particles, which is a function of the patch size. Owing to the H_2O_2 decomposition catalyzed by Pt, the concentration profile determines the imbalanced body force. The Stokes equation at small Reynolds numbers including the body force term is solved analytically to determine the particle velocity. The analytical solution is briefly discussed in this sub-section and a detailed derivation of all the equations is provided in Appendix A.

The diffusion equation in the absence of convective transport (low Péclet number) for hydrogen peroxide can be written as:

$$D\nabla^2 C = 0 \tag{4.10}$$

Assuming the azimuthal symmetry, the axisymmetric Laplace equation in spherical coordinates can be written as:

$$D\left\{\frac{\partial}{\partial r}\left(r^2\frac{\partial C(r,\theta)}{\partial r}\right) + \frac{1}{\sin(\theta)}\frac{\partial}{\partial \theta}\left[\sin(\theta)\frac{\partial C(r,\theta)}{\partial \theta}\right]\right\} = 0 \tag{4.11}$$

subject to the boundary conditions:

$$\lim_{r\to\infty} C(r,\theta) = C_\infty \tag{4.12}$$

and

$$C(a,\theta) = 0, \qquad 0 \le \theta < \alpha_{Pt} \tag{4.13}$$

$$\frac{\partial}{\partial r}C(a,\theta) = 0, \qquad \alpha_{Pt} < \theta \le \pi \tag{4.14}$$

where a is the particle radius and α_{Pt} is the platinum cap angle. The platinum cap angle, α_{Pt}, is the percentage circumference covered by the Pt cap expressed in an angle, assuming an azimuthal symmetry. The boundary condition (4.13) is based on the assumption of an instantaneous reaction and Eq.(4.14) represents a no-flux boundary condition at the particle surface. The radial coordinate and the

concentration are non-dimensionalized by,

$$R = \frac{r}{a}, \qquad \bar{C}(R,\theta) = \frac{C(r,\theta)}{C_\infty}. \tag{4.15}$$

Separation of variables gives the solution of the Laplace Eq.(4.11) in terms of a non-dimensionalized concentration as:

$$\bar{C}(R,\theta) = \sum_{n=0}^{\infty} \left[B_n R^n + A_n R^{-(n+1)} \right] P_n(\cos\theta) \tag{4.16}$$

where $P_n(\cos\theta)$ are Legendre polynomials of the order n. Using the non-dimensionalized form of the boundary condition (4.12), we get

$$B_0 = 1, \qquad B_n = 0, \quad n > 0 \tag{4.17}$$

$$\therefore \quad \bar{C}(R,\theta) = 1 + \sum_{n=0}^{\infty} A_n R^{-(n+1)} P_n(\cos\theta) \tag{4.18}$$

Substituting Eq.(4.18) into the boundary conditions (4.13) and (4.14) yields the dual Fourier-Legendre series

$$\sum_{n=0}^{\infty} A_n P_n(\cos\theta) = -1, \quad 0 \le \theta < \alpha_{Pt} \tag{4.19}$$

and

$$\sum_{n=0}^{\infty} (n+1) A_n P_n(\cos\theta) = 0, \quad \alpha_{Pt} < \theta \le \pi \tag{4.20}$$

The constants A_n are obtained by solving the dual series (4.19) and (4.20), which gives the concentration distribution (4.18). The analytical solution for the dual Fourier-Legendre series is adopted from the literature.[89] Figure 4.13 depicts a non-dimensionalized concentration profile of hydrogen peroxide around the patchy particles with patch sizes of 50 %, 25 %, and 11 %, respectively. The blue-colored region indicates low H_2O_2 concentration (near Pt cap on the particle surface) and

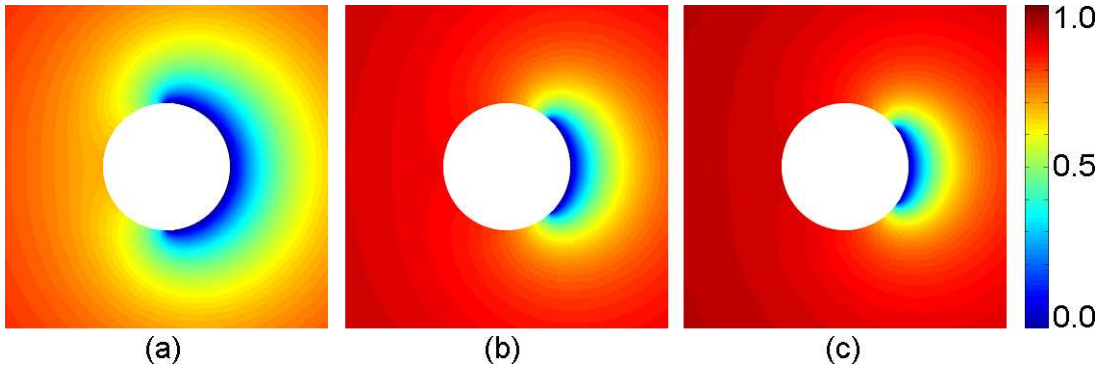

Figure 4.13: Non-dimensionalized concentration profile ($\bar{C}(R,\theta)$) of H_2O_2 around a patchy particle coated with Pt (a) 50 % patch (cap angle = 0.5 π), (b) 25 % patch (cap angle = 0.26 π), and (c) 11 % patch (cap angle = 0.2 π). The blue-colored region indicates low H_2O_2 concentration (near Pt cap on the particle surface) and the red-colored region indicates the uniform bulk concentration far away from the particle.

the red-colored region indicates the uniform bulk concentration far away from the particle.

The short range physical interaction between the solute (hydrogen peroxide) and the particle is described by a potential of mean force ϕ. The solute molecules experience a force of $-\nabla\phi$ in the proximity of the particle within a thin interfacial layer. In our analysis ϕ is assumed to be only a function of r. The coupling of the concentration field near the particle and the force field $-\nabla\phi$ produces stresses near the particle surface, which results in the motion of the fluid. The continuity and the Naiver-Stokes equation at low Reynolds number are

$$\nabla \cdot \mathbf{v} = 0, \tag{4.21}$$

$$\mu\nabla^2\mathbf{v} - \nabla p - C\nabla\phi = 0, \tag{4.22}$$

$$\mathbf{v} = 0 \qquad (r = a), \tag{4.23}$$

$$\mathbf{v} \to -U\mathbf{e}_\phi \qquad (r \to \infty), \tag{4.24}$$

where U is the unknown particle velocity. A stream function (ψ) is defined by

$$\mathbf{v} = \frac{\mathbf{e}_\phi}{r\sin\theta} \times \nabla\psi(r,\theta) \tag{4.25}$$

The pressure gradient term in Eq.(4.22) is eliminated by taking the curl of both sides of the equation.[90,91] Simplification of Eq.(4.25) gives,

$$\therefore \quad \mu \frac{\mathbf{e}_\phi}{r \sin\theta} E^4 \psi = (\nabla C) \times (\nabla \phi) = \left(-\frac{1}{r} \frac{\partial C(r,\theta)}{\partial \theta} \frac{\partial \phi}{\partial r} \right) \mathbf{e}_\phi \tag{4.26}$$

The simplified non-dimensionalized form of the Eq.(4.26) is given as

$$E^4 \Psi = -\Lambda \sum_{n=1}^{\infty} \frac{A_n}{R^{(n+1)}} Q_n(\eta)(n)(n+1) \frac{\partial \Phi}{\partial R} \tag{4.27}$$

$$\Lambda = \frac{C_\infty akT}{\mu U} \tag{4.28}$$

where $R = r/a$, $\Psi = \psi/Ua^2$, and $\Phi = \phi/kT$. For convenience, we replace $\cos(\theta) = \eta$ and $C_{n+1}^{-1/2} = -Q_n$ in Eq.(4.27) where polynomial functions $C_{n+1}^{-1/2}$ are called Gegenbauer polynomials of degree (-1/2). The solution to Eq.(4.27) leads to the particle velocity U. Eq. (4.27) can be split into two second-order equations.

$$E^2 \Psi = \omega, \tag{4.29}$$

$$E^2 \omega = F. \tag{4.30}$$

$$F = -\Lambda \sum_{n=1}^{\infty} \left[\frac{A_n}{R^{(n+1)}} (n)(n+1) \frac{\partial \Phi}{\partial R} \right] Q_n(\eta) \tag{4.31}$$

where the E^2 operator takes the simplified form

$$E^2 = \frac{\partial}{\partial R^2} + \frac{(1-\eta^2)}{R^2} \frac{\partial^2}{\partial \eta^2} \tag{4.32}$$

The homogeneous solution of Eq.(4.30) is obtained by the method of separation of variables.[92]

$$\omega_{homo} = \sum_{n=1}^{\infty} (a_n R^{n+1} + b_n R^{-n}) Q_n(\eta) \tag{4.33}$$

The non-homogeneous solution is obtained through a substitution of the form[93]

$$\omega_{non-homo} = \sum_{n=1}^{\infty} H_n Q_n(\eta) \tag{4.34}$$

Applying the operator E^2 to ω ($\omega = \omega_{homo} + \omega_{non-homo}$) and substituting in Eq.(4.30), we obtain a second order equation for H_n as:

$$R^2 \frac{\partial^2 H_n}{\partial R^2} - (n)(n+1)H_n = -\Lambda \frac{A_n(n)(n+1)}{R^{n+1}} \frac{\partial \Phi}{\partial R} R^2 \tag{4.35}$$

The method of variation of parameters is used to obtain a non-homogeneous solution of H_n, which leads to the complete solution of ω as, $\omega = \omega_{homo} + \omega_{non-homo}$,

$$\omega = \sum_{n=1}^{\infty} \left\{ A_n R^{n+1} + B_n R^{-n} - \tilde{\Lambda} \int_{R_0}^{R} (s^{-(2n+1)} R^{n+1} - R^{-n}) \frac{\partial \phi}{\partial s} ds \right\} Q_n(\eta) \tag{4.36}$$

$$\tilde{\Lambda} = \Lambda \frac{A_n(n)(n+1)}{(2n+1)} = \frac{A_n C_\infty akT(n)(n+1)}{\mu U(2n+1)} \tag{4.37}$$

Substituting ω in Eq.(4.29), we get a non-homogeneous equation for Ψ, which is similar in structure to Eq.(4.30). Following the same solution procedure from (4.33) to (4.36), we get the solution for Ψ as:

$$\Psi = \sum_{n=1}^{\infty} \left\{ A_n R^{n+3} + B_n R^{-n+2} + C_n R^{n+1} + D_n R^{-n} - g_n(R) \right\} Q_n(\eta) \tag{4.38}$$

$$g_n(R) = \frac{1}{(2n+1)} \int_{R_0}^{R} (t^{-n} R^{n+1} - R^{-n} t^{n+1}) f_n(t) dt \tag{4.39}$$

$$f_n(t) = \tilde{\Lambda} \int_{R_0}^{t} (s^{-(2n+1)} t^{n+1} - t^{-n}) \frac{\partial \Phi}{\partial s} ds \tag{4.40}$$

The solution to Eq.(4.38) is sought with respect to the boundary conditions

$$\Psi(1) = \Psi'(1) = 0 \tag{4.41}$$

$$\Psi(\infty) \rightarrow \frac{1}{2}R^2 \sin^2\theta \tag{4.42}$$

Substituting the boundary conditions (4.41) and (4.42) in (4.38) and matching the powers of $\sin\theta$, we get the constants as:

$$A_n = 0, \ (n \geq 1) \tag{4.43}$$

$$C_1 = -1, \qquad C_n = 0, \ (n > 1) \tag{4.44}$$

$$B_1 = -\frac{3}{2}C_1 + \frac{1}{2}\left(g_1 + \frac{\partial g_1}{\partial R}\right)_{R\rightarrow 1}, \qquad B_n = \frac{1}{2}\left(g_n + \frac{\partial g_n}{\partial R}\right)_{R\rightarrow 1}, (n > 1) \tag{4.45}$$

$$D_1 = \frac{1}{2}C_1 + \frac{1}{2}\left(g_1 - \frac{\partial g_1}{\partial R}\right)_{R\rightarrow 1}, \qquad D_n = \frac{1}{2}\left(g_n - \frac{\partial g_n}{\partial R}\right)_{R\rightarrow 1}, (n > 1) \tag{4.46}$$

Thus, the solution for Ψ is given as:

$$\begin{aligned}\Psi &= \left(B_1 R + C_1 R^2 + D_1 R^{-1} - g_1(R)\right) Q_1(\eta) \\ &\quad + \sum_{n=2}^{\infty}\left\{B_n R^{-n+2} + D_n R^{-n} - g_n(R)\right\} Q_n(\eta)\end{aligned} \tag{4.47}$$

The drag on the particle in a non-dimensional form is calculated as :[93,94]

$$\frac{F_z}{2\pi\mu U a} = \int_0^{\pi}\left\{R^4 \frac{\partial}{\partial R}\left(\frac{E^2\Psi}{R^2}\right)\frac{-Q_1(\eta)}{\sin\theta} d\theta\right\} \tag{4.48}$$

Eq.(4.48) does not contain a term for the body force, because of the assumption that $-\nabla\Phi$ is only a function of R and not of θ. Note, $E^2\Psi = \omega$ and is given by Eq.(4.36). Also, using the orthogonality of $Q_n(\eta)$ polynomials, Eq.(4.48) can be simplified to,

$$\frac{F_z}{2\pi\mu U a} = B_1 + \frac{1}{3}\left[R^4 \frac{\partial}{\partial R}\left(\frac{f_1(R)}{R^2}\right)\right]_{R\rightarrow 1} \tag{4.49}$$

where $f_1(R)$ is described by Eq.(4.40).

In order to obtain an expression for U in terms of known parameters, another physical constraint is needed. This is achieved by equating the net drag force to zero. Thus from Eq. (4.49):

$$U = -\frac{1}{3}\left\{\left(\tilde{g_1}(R) + \frac{\partial \tilde{g_1}(R)}{\partial R}\right)_{R\to 1}\right\} - \frac{2}{9}\left\{R^4 \frac{\partial}{\partial R}\left(\frac{\tilde{f_1}(R)}{R^2}\right)\right\} \tag{4.50}$$

where $\tilde{g}_n$ and $\tilde{f}_n$ are obtained from Eq.(4.39) and Eq.(4.40) by multiplying g_n and f_n by U.

$$\tilde{g_1}(R) = \frac{1}{3}\int_{R_0}^{R} (t^{-1}R^2 - R^{-1}t^2)\tilde{f_1}(t)dt \tag{4.51}$$

$$\tilde{f_1}(t) = \Upsilon_1 \int_{R_0}^{t} (s^{-3}t^2 - t^{-1})\frac{\partial \Phi}{\partial s} ds \tag{4.52}$$

$$\Upsilon_n = \frac{A_n C_\infty akT(n)(n+1)}{\mu(2n+1)} \tag{4.53}$$

It should be noted that the velocity obtained using Eq.(4.50) is based on the H_2O_2 concentration gradient only. The velocity is corrected by taking into account the drag exerted by the concentration gradient of oxygen in Eq.(4.48). The concentration gradient of water generated due to the reaction is negligible as the solvent is water itself. Then it can be easily shown that the corrected particle velocity is,

$$\begin{aligned} U \;=\; & -\frac{1}{3}\left\{\frac{1}{2}\left(\tilde{g_1}(R) + \frac{\partial \tilde{g_1}(R)}{\partial R}\right)_{R\to 1} + \frac{1}{3}\left(R^4 \frac{\partial}{\partial R}\frac{\tilde{f_1}(R)}{R^2}\right)_{R\to 1}\right\}_{H_2O_2} \\ & -\frac{1}{3}\left\{\frac{1}{2}\left(\tilde{g_1}(R) + \frac{\partial \tilde{g_1}(R)}{\partial R}\right)_{R\to 1} + \frac{1}{3}\left(R^4 \frac{\partial}{\partial R}\frac{\tilde{f_1}(R)}{R^2}\right)_{R\to 1}\right\}_{O_2} \end{aligned} \tag{4.54}$$

Eq.(4.54) can be used to calculate the particle velocity for a given potential function Φ, which appears in $\tilde{g_1}(r)$ and $\tilde{f_1}(r)$ through equations (4.51) and (4.52). The direction of the particle motion is governed by the contributions from the H_2O_2 and O_2 concentration gradients in Eq.(4.54).

4.2.5 Validation of the proposed theory using the experimental results

In order to explain the motion of the patchy particles through the proposed theory, it is essential to correlate the experimentally observed particle velocities (Fig. 4.12) with the theoretically derived expressions for the particle velocities (Eq.(4.54)). More precisely, the theory can be validated by determining the direction of the particle motion and the measured velocity of the particles.

The direction of the motion of the patchy particles has not yet been confirmed experimentally but can be determined by labeling the Pt patches with fluorescent probes. Such fluorescently labeled patchy particles can visualize the direction of the particle motion using fluorescence microscopy.

The correct choice of the potential function in the theoretical model will yield both the direction and the magnitude of the velocity of the patchy particles. Although, the exact potential functions cannot be determined experimentally, Lennard-Jones ($R^{-9} + R^{-3}$)or exponential potential function can be used in these equations. Unfortunately, the Lennard-Jones potential goes to infinity at $R = 1$ (at the surface) and the integrals in Eq.4.54 go to infinity. Thus, the velocity of the particle has to be determined using another form of a potential such as an exponential potential.

4.2.6 Summary

In this section we demonstrated the application of patchy particles as autonomously moving osmotic motors. The autonomous motion is attributed to the solute concentration-gradient produced by the catalytic activity of the patches on the particle surface. The motion of the Pt-coated patchy particles in an oxidative environment of H_2O_2 is investigated as the patch size is varied from 11 % to 25 % to 50 % of the particle surface. Our study demonstrates that as the patch size increases,

the particle velocity increases accordingly.

The motion of the patchy particles is analyzed mathematically using the hypothesis that the imbalance of the solute concentration leads to an imbalance of the body force experienced by the particle, which in turn propels the particle. The concentration gradient of the solute is obtained around a patchy particle by solving the diffusion equation. Note, the concentration gradients obtained here are based on the assumption that the reaction is instantaneous on the patch surface. The Stokes equation of motion with an additional body force term arising from the concentration gradient is solved analytically to obtain an expression for the particle velocity. The expression for the particle velocity, when fitted with the potential energy function, can be implemented to estimate the particle velocity produced due to the concentration gradient.

4.3 Self-assembly of T-structures using an Ising lattice model

In this chapter we discuss a computational approach towards self-assembly of specific target structures using patchy particles. The thermodynamic Ising lattice model with principles of lattice Density Functional Theory (DFT) is employed to describe the equilibrium self-assembly of anisotropic particles into a target T-structure (Figure 4.14) as a function of interaction energies, concentration of particles, and temperature. The T-structure is chosen as it represents an interesting model structure for plasmonic waveguides,[95] three-way connectors,[96,97] and spin filters.[98] The thermodynamic model shows the possibility of formation of the T-structure at equilibrium but does not take into account the dynamics involved in the self-assembly. The Dynamic Mean Field (DMF) model is employed to account for the dynamics involved in the assembly. This section emphasizes the results obtained from the

lattice DFT approach on assembling the T-structure with concluding remarks on the implications of preliminary DMF calculations for future simulations.

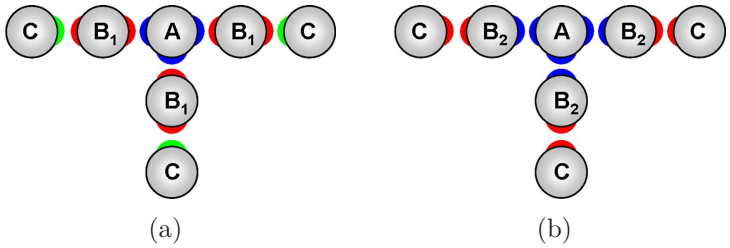

Figure 4.14: The model T-structures. (a) Symmetric middle particle : B_1, and (b) Asymmetric middle particle : B_2

4.3.1 Ising Lattice model with principles of lattice DFT

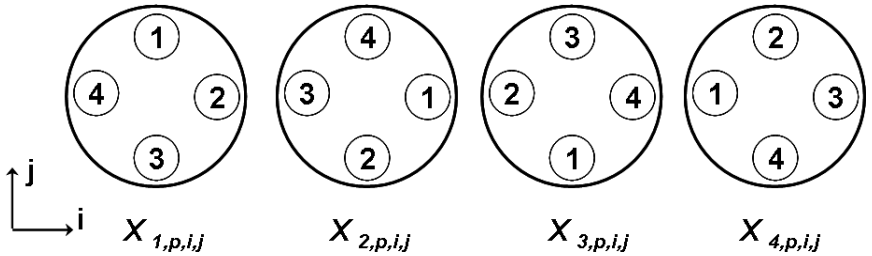

Figure 4.15: The four orientations a four-pole particle can assume on each site of a planar lattice. $x_{k,p,i,j}$ (p = A, B_n, or C and $k = 1 - 4$) is the probability that the lattice site (i, j) is occupied by a p type particle with orientation k.

The model used in the simulations is an Ising lattice model employing a lattice density functional approach with anisotropic interactions between particles, as developed by Aranovich and Donohue (AD).[28] The Initial AD model (based on a single anisotropic particle) is extended for a mixture of three types (A, B_n, and C) of anisotropic particles. For generalization, the model is developed based on anisotropic particles having four patches on their poles (Fig. 4.15). In the present model, particles having three (A), two (B_n), and one (C) patches are used and the remaining pole patches are considered as particle surfaces. Such four-pole patchy particles can orient themselves in any of the four orientations on a lattice site (i, j) ($i = -10$ to 10 and $j = -10$ to 10) as illustrated in Figure 4.15. The lattice site is either occupied by a

particle or empty (i.e., occupied by a solvent molecule). The interactions between the solvent molecule and the particle are neglected in the analysis. The order parameters $x_{k,p,i,j}$ give the probability that the lattice site (i, j) is occupied by a p type particle ($p =$ A, B_n, C) with the kth orientation ($k = 1-4$). The probability for the site to be occupied by a specific particle (A, B_n, or C) comes from the contribution of the four orientations at the site and hereafter is referred to as the total density distribution of this particle ($\rho_p(i, j)$) as given by Eq.(4.55):

$$\rho_p(i, j) = x_{1,p,i,j} + x_{2,p,i,j} + x_{3,p,i,j} + x_{4,p,i,j} \tag{4.55}$$

The anisotropic interactions between the particles are incorporated in the model by assigning different interactions between different patches. The total Hamiltonian of the system is calculated based on the interaction energy between two particles sitting on neighboring sites. The Hamiltonian for two neighboring lattice sites in the mean field approximation is given by Eq.(4.56):

$$E = \left(\frac{1}{2}\right) \sum_{a=particle1}^{particle3} \sum_{b=particle1}^{particle3} \sum_{m=orientation1}^{orientation4} \sum_{n=orientation1}^{orientation4} (\epsilon_{abmn} p(a, m)p(b, n)) \tag{4.56}$$

where ϵ_{abmn} is the interaction energy between the ath and bth type of particle (a,b = 1 - 3) with contact points m and n (m,n = 1 - 4). $P(a, m)$ and $P(b, n)$ are the respective probabilities for the neighboring lattice sites being occupied by an ath and bth type of particle in such a way that they have a contact point m on the ath particle and n on the bth particle. The Helmholtz free energy, F, is calculated based on the total Hamiltonian, U, and the entropy (per site), S.

$$F = U - TS \tag{4.57}$$

For an open system the grand potential, Ω, must be minimized at equilibrium, which

gives a variational Eq.(4.59) in the absence of an external potential.[99]

$$\Omega[x_{k,p,i,j}] = F[x_{k,p,i,j}] - \sum_{p=1}^{p=3} \mu_p \Bigg\{ \sum_{i=-i^*}^{i^*} \sum_{j=-j^*}^{j^*} \sum_{k=1}^{k=4} x_{k,p,i,j} \Bigg\} \tag{4.58}$$

$$\frac{\delta F[x_{k,p,i,j}]}{\delta x_{k,p,i,j}} - \mu_p = 0 \tag{4.59}$$

where μ_p is the chemical potential of the species p. Using the equation for the intrinsic Helmholtz free energy, F, a set of equations given by Eq.(4.59) can be solved for the equilibrium density distribution of the A, B_n, and C particles.

The bulk densities of the particles, $x_{\infty A}$, $x_{\infty B_n}$, and $x_{\infty C}$ referred to as the concentrations of A, B_n, and C particles, respectively, are themselves solutions for the equilibrium density distribution equations (4.59) due to the self-consistent nature of the lattice density functional equations. In order to obtain non-uniform density profiles, the system is perturbed by placing an A particle with a particular orientation at the center point $(0, 0)$ of the lattice. The equilibrium density distributions of A, B_n, and C particles are studied around the A particle at $(0, 0)$ and are calculated based on the equality of the chemical potentials, which result from classical Ono - Kondo theory. The non-linear simultaneous lattice density functional equations for the equilibrium density distribution are solved using the method of successive substitution with an initial guess of a random density distribution at all lattice sites. The initial random density distributions at all lattice sites represent the mathematical starting point for the successive substitution calculations and are not related to the density distributions in the real system evolving towards equilibrium. The details of the equations and the solution procedure are given in Appendix B.

Table 4.1: Range of Parameters Explored in Calculations

Parameter	**Case 1**[a]	**Case 2**[b]
Temperature [K]	$275 - 375$	300
Interactions [eV]		
Specific interactions in the T-structure	*strong* attractive : 1.0 - 8.0 *weak* attractive : 0.5 - 7.5	*strong* attractive : 2.5 - 3.5 *weak* attractive : n.a.
Non-specific interactions	*rest all* attractive : 0 - 0.047 *rest all* repulsive: n.a.	*weak* attractive: 1.0 - 2.0 *rest all* repulsive 0.3 - 2.0
Concentration		
A	0.001	0.0001 - 0.0005
B_n	0.003	0 - 0.0031
C	0.003	0 - 0.016

[a] T-structure with symmetric B_1 particle. [b] T-structure with asymmetric B_2 particle

4.3.2 Effect of parameters on the self-assembly of the T-structure

Choice of parameters in the mathematical model : A system of three types of particles with four poles gives rise to 82 independent parameters in three sets; i.e., concentration (3), inter-particle interactions including only distinguishable pairs (78), and temperature (1). The inter-particle interactions can be categorized as (i) the interactions that lead to the formation of the T-structure including A - B_n and B_n - C particle patch interactions, and (ii) the interactions that do not take part in the formation of the T-structure and are responsible for uncontrolled particle condensation such as A - C particle patch interactions and non-specific interactions between patches and bare particle surfaces. The large number of parameters (82) would require numerous calculations. Thus, we have reduced the parameter space to 8 parameters using the arguments given in the following subsection. The parameter space investigated is summarized in Table 4.1.

Case 1. Symmetric two-patch particle (B_1): To form the T-structure shown in Figure 4.14(a), both the A - B_1 and B_1 - C particle patch interactions must be attractive. To ensure the binding of C particles to B_1 particles in the T-shape precursor, the B_1 - C particle patch interaction should not only be attractive but has to be more attractive than a certain threshold in order to avoid formation of an A and B_1 particle network. Thus, for Case 1 the B_1 - C particle patch interaction is defined as a *strong* attractive interaction, the A - B_1 particle patch interaction is defined as a *weak* attractive interaction. All other non-specific interactions between non-binding patches and bare surfaces are summarized under the term *rest all* interactions. Since *rest all* interactions account for attractive physical interactions, e.g., van der Waals interactions (0.02 - 1.3 eV), the maximum attractive *rest all* interaction the system can tolerate without non-specific condensation of particles are calculated.

Case 2. Asymmetric two-patch particle (B_2) : In Case 2 (Figure 4.14(b)), attractive interactions between identical patches are used to form the T-structure. The asymmetry of the B_2 particle patches ensures that the A particles will not bind to the B_2 particles in the T-shaped precursor formed by attractive interactions between identical patches; therefore both the A - B_2 and B_2 - C particle patch interactions are defined as *strong* attractive interactions. Note the *strong* attractive interactions between identical patches not only allow binding of A - B_2 and B_2 - C particles but also allow interaction of same-type particles (A-A, B_2-B_2, and C-C) leading to various structures such as dimers, trimers, and chains (Figure 4.16). Thus, the relative concentrations of A, B_2, and C particles play an important role in the formation of the T-structure. The equilibrium density distributions around the A particle at (0,0) are studied with varying concentrations of A (0.0001 - 0.0005), B_2 (0 - 0.0031), and C (0 - 0.016) particles. In contrast to Case 1, two groups of non-specific interactions; (i) *weak* attractive interactions between non-identical patches and (ii) *rest all* interactions

between patch/bare and bare/bare surfaces are defined.

4.3.3 Results and Discussion

This subsection describes the computational results of the effect of different parameters such as concentration of (A, B_n, C) particles , interaction energies (*strong* attractive, *weak* attractive, and *rest all* interactions), and temperature on finite structures assembled at low concentrations of particles (< 1 %). The term "finite structures" refers to structures formed by covalent interactions. An increase in either the attractive interactions between the finite structures or the concentrations of particles, can lead to a network of finite structures, hereafter referred to as phase of non-specific condensation. The equilibrium density distributions of A, B_n, and C particles around the A particle at (0,0) are used to differentiate the structure phase, which can be either the finite structure or the non-specific condensation phase, from the solvent-rich phase. Lattice sites with equilibrium density distributions of particles of ~ 1 (sites occupied by particles) constitute the structure phase, while the sites with equilibrium density distributions of particles similar to the bulk density of particles belong to the solvent-rich phase. Structural phase diagrams indicating regions with particular structures observed in the simulations are constructed form the obtained results. Figure 4.16 summarizes all the structures that form in Case 1 (Figure 4.16(a)-(b)) and Case 2 (Figure 4.16(c)-(h)). The dotted ovals indicate binding sites that are accessible to more than one particle. Note that in structures with more than one oval all possible combinations of particles are accessible, i.e., 8 possible structures for the T-structure in Figure 4.16(d).

Phase transition between different structures Multiple solutions of the equilibrium density distribution equations are expected at the phase boundaries between two structure phases and in the phase of non-specific condensation of particles

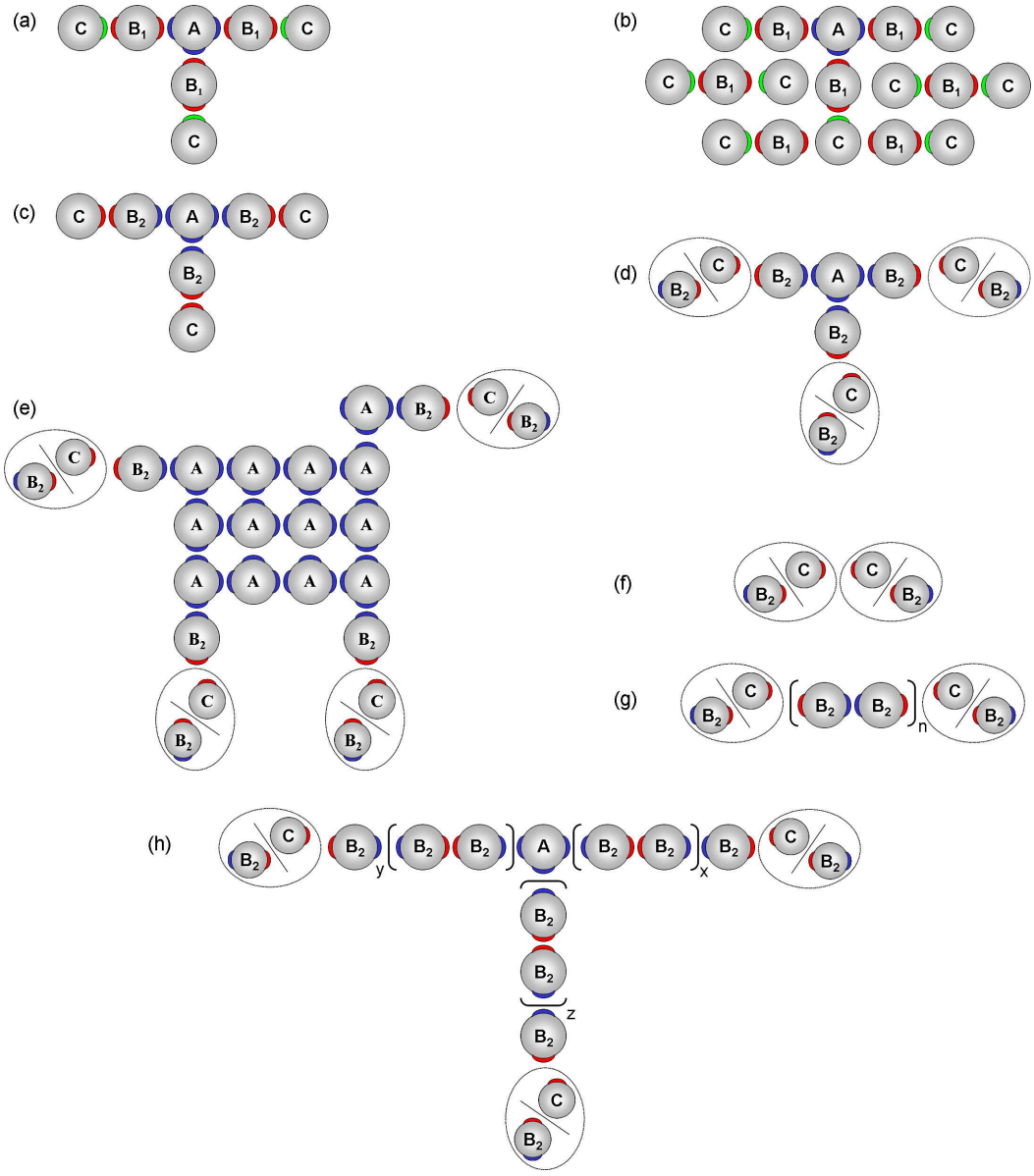

Figure 4.16: Schematic representation of all structures observed in the two systems of particles. Case 1: (a) T-structure and (b) non-specific condensation of particles. Case 2: (c) T-structure, (d) incorrect T-structure, (e) condensation of A particles, (f) dimers of B_2/C particles, (g) chains of B_2 particles, and (h) extended T-structure.

each corresponding to a local minimum. The existence of such a large number of degenerate low-energy states has been previously shown by Witman and Wang.[34] The successive substitution method used to solve the density distribution equations fails when multiple solutions to the equations exist and a different algorithm is required.[100] Thus, the phase boundaries described are not defined by the equality of the chemical potential of the two adjacent phases with our method, but rather report phase transition regions within which the exact transition boundary is located.

Case 1. Symmetric two-patch particle (B_1): In all calculations performed either T-structure formation in the finite structure phase (Fig. 4.16(a)) or non-specific condensation (Fig. 4.16(b)) is observed. Within the T-structure, the positions in the T-structure are occupied specifically by A, B_1, and C particles, i.e., no distributions of particles are observed at those lattice sites. An increase of the attractive *rest all* interactions above a certain threshold results in a phase transition from the T-structure to non-specific condensation, which is propagated through the *strong* attractive B_1 - C particle patch interactions. The attractive *rest all* interactions the system can tolerate without the non-specific condensation can be determined and are ploted in Figure 4.17 as *strong* and *weak* attractive interactions are varied.

Figure 4.17(a) shows that the attractive *rest all* interactions required for transition from the T-shaped structure to non-specific condensation decrease with increasing *strong* and *weak* attractive interactions. The attractive *rest all* interactions calculated represent the maximum *rest all* interactions the system can tolerate without non-specific condensation of particles. Every parameter combination below the line, where *strong* and *weak* attractive interactions are equal (y = x), leads to a network of A and B_1 particles due to the competition of A and C particles for the terminal positions in the T-shaped precursor. Figure 4.17(b) illustrates the effect of temperature and *strong* attractive interactions on the maximum attractive *rest all* interaction

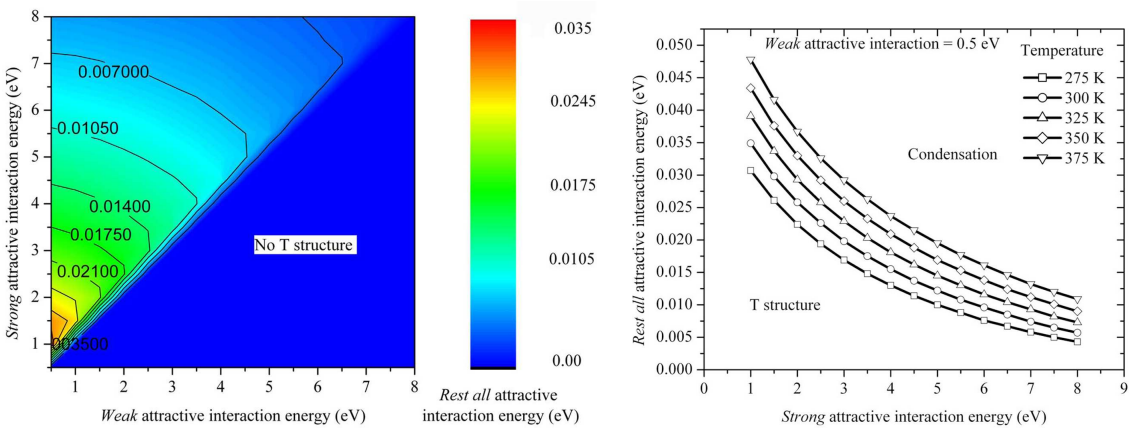

Figure 4.17: (a) Effect of *strong* and *weak* attractive energies on maximum *rest all* attractive interaction energy for Case 1 at T = 300 K. The color bar indicates the magnitude of attractive *rest all* interactions in eV., and (b) Effect of *strong* interaction energy at various temperatures (275-375K) in Case 1 on maximum *rest all* attractive interaction energy. The *weak* attractive interaction energy is kept constant at 0.5 eV.

leading to the transition. Parameter combinations below the curves lead to the T-shaped structure, while those above lead to non-specific condensation. Lower *strong* attractive interaction energies and higher temperatures allow the system to tolerate higher attractive *rest all* interactions without particle condensation. Further, the larger the *strong* attractive interactions, the smaller the effect of temperature on the attractive *rest all* interaction is.

Case 2. Asymmetric two-patch particle (B_2): The non-specific condensation due to attractive *rest all* interactions as observed in Case 1 is avoided due to repulsive *rest all* interactions in Case 2. In contrast to Case 1 where only the T-structure is observed, several structures are found within the finite structure phase in Case 2 such as (i) a mixture of T-structures (Figs. 4.16(c) and (d)), (ii) chains and extended T-structure (Figs. 4.16(g) and (h)), (iii) condensation of A particles (Fig. 4.16(e)), and (iv) dimers of C/B_2 particles (Fig. 4.16(f)). Analysis of the density distribution plots for the T-structure in Case 2 shows that the positions in the T-shaped precursor surrounding the center A particle, are occupied specifically by A or B_2 particles, while

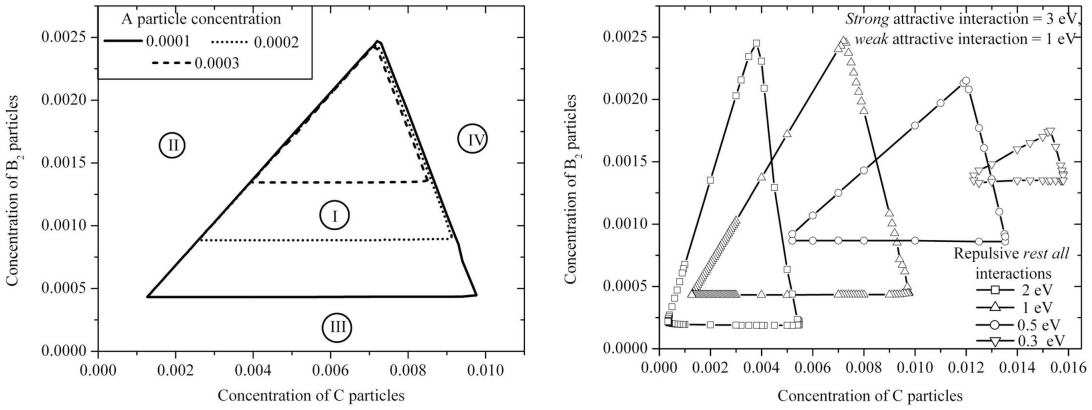

Figure 4.18: Phase diagrams for system of particles in Case 2 at T = 300 K, showing (a) the effect of the A particle concentration at constant interaction energies (*strong* = -3 eV, *weak* = -1 eV and *rest all* = +1 eV) (b) the effect of repulsive *rest all* interactions at $X_{\infty A}$ = 0.0001.

a distribution of C and B_2 particles is observed at the lattice sites corresponding to the terminal positions in the T-structure as indicated by the dotted ovals in Figure 4.16(d). Thus, the density distribution of the T-structure is referred to as a mixture of T-structures (Fig. 4.16(d)) since the terminal positions of the T-structure can either be occupied by C or B_2 particles.

Variation of both the relative particle concentrations of B_2 and C particles and the interaction energies at various A particle concentrations enables the construction of structure phase diagrams within the finite structure phase (Fig. 4.18). Four structured phase regions are identified and labeled I, II, III, and IV in Figure 4.18(a). The regions correspond to phases with a mixture of T-structures (Figs. 4.16(c) and (d)), extended T-structure and chains (Fig. 4.16(g) and (h)), condensation of A particles (Fig. 4.16(e)), and formation of particle dimers (Fig. 4.16(f)), respectively. The region where T-structures are formed is region I, which includes correct (terminated by C, Fig. 4.16(c)) and incorrect (terminated by B_2, Fig. 4.16(d)) T-structures and is delimited by a triangle in the B_2 - C particle concentration plane. Note, the solid lines indicate density distributions corresponding to a new structure phase and not the exact phase boundary between two adjacent phases.

The boundary between region I and region II corresponds to the change of the equilibrium density distributions at the terminal positions of the T-structure from a distribution of C/B_2 particles to B_2 particles only. The transition occurs at high B_2 particle concentration with increasing C particle concentration. The boundary between region III and region I represents the transition where the equilibrium density distribution at the lattice sites adjacent to (0,0) changes from an A (region III) to a B_2 particle (region I). The III-I transition is independent of the C particle concentration. At high C and B_2 particle concentrations, dimers of B_2/C particles form (region IV). An increase in the C particle concentration favors the $(B_2)_2$, C_2, and (B_2C) dimer formation near the A particle at (0,0), thus limiting the formation of T-structures (region I). Figure 4.18(a) also shows the effect of the absolute A particle concentration on region I at constant *strong* attractive, *weak* attractive, and repulsive *rest all* interactions of -3, -1, and +1eV, respectively. As the A particle concentration is increased from = 0.0001 (solid line) via = 0.0002 (dotted line) to = 0.0003 (dashed line) the T-structure phase (region I) is reduced. Figure 4.18(b) shows the effect of the repulsive *rest all* interactions (0.3-2 eV) on region I. As the repulsive *rest all* interactions increase from 0.3 to 1 eV, region I increases by a tenfold, whereas repulsive *rest all* interactions above 1 eV reduce the phase space for the T-structure by approximately 40 %. In the range of parameters used for our calculations, no evidence of the T-structure formation is found when attractive *rest all* interactions are used in the calculations.

As mentioned above, a mixture of correct (C-terminated) and incorrect (B_2-terminated) T-structures is formed in region I. Figure 4.19 investigates the relative distribution of the two structures within region I. The C/B_2 concentration ratio is optimized as a function of the A particle concentration such that a maximum percentage of C-terminated T-structures is obtained. We find that lower A particle concentrations enable larger amounts of correct, C-terminated T-structures at higher

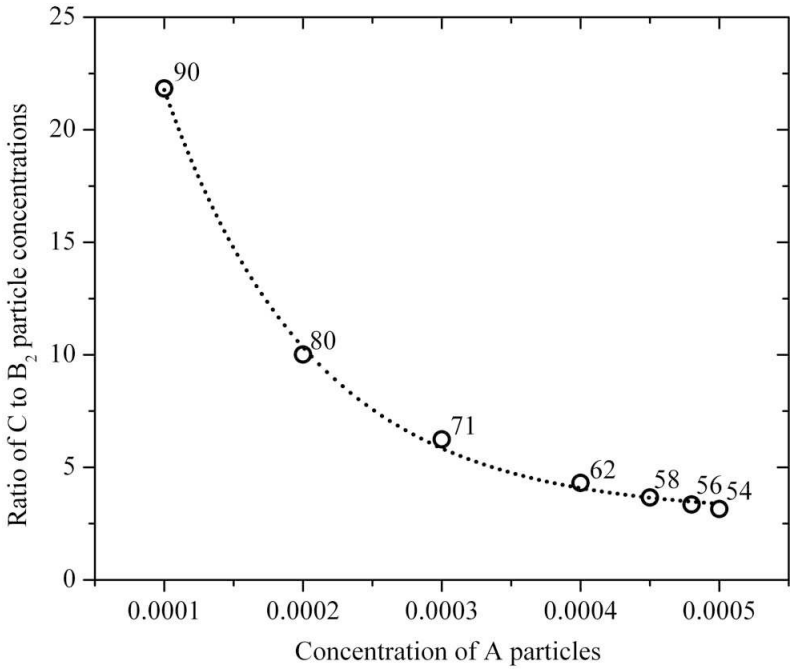

Figure 4.19: Plot of C/B_2 particle concentration ratio leading to maximum percentage of correct T-structure (numbers at each point) within region I as a function of A particle concentration.

C/B_2 particle ratios, i.e., bottom-right corner of region I.

Comparison of Case 1 and Case 2: The inherent difference between both cases is that in Case 1 either the T-structure is formed or non-specific condensation occurs owing to the carefully chosen patch interactions. In contrast, the patch interactions for Case 2 enable the formation of chains, extended T-structures, dimers, incorrect T-structures, and the targeted T-structure in the structured phase, while non-specific condensation is avoided because of repulsive *rest all* interactions.

In Case 1, each of the three particles (A, B_1 and C) has patch(es) specific to the particle. The A and C particle patches can only interact with the two identical B_1 particle patches thereby enforcing the formation of the T-structure. The parameter sets leading to T-structure formation can be found for the complete temperature range accessible to water (275 to 375 K), which is a potential solvent for the assembly. A wide range of *strong* (1 - 8 eV) and *weak* attractive interactions (0.5 -7.5 eV) between

B_1-C and A-B_1, respectively, lead to the formation of the T-structure with attractive *rest all* interactions ranging from 0 to 0.047 eV. The magnitude of the attractive *rest all* interactions overlaps sufficiently with the range of known van der Waals interactions (0.02 to 1.3 eV).[71]

Case 2 is based on the strong attractive identical patch interactions, where the B_2 particle carries two different patches. The patch anisotropy of the B_2 particle leads to chain formation and B_2-terminated T-structures, while the *strong* attractive interaction between identical patches is the cause for A particle condensation and B_2/C particle dimerization. As can be seen in Figure 4.18, structure-phase diagrams with a complex dependence on B_2 and C particle concentration and repulsive *rest all* interactions result. Within the T-structure phase space, the C- and B_2-terminated T-structures compete. Formation of the correct, C-terminated T-structure is favored by the highest possible C/B_2 ratio and the lowest possible A particle concentration. A high C/B_2 ratio leads to a higher probability of C-termination and a lower A particle concentration decreases the threshold for condensation/T-structure transition.

Although for both cases, Case 1 and Case 2, the synthetic scenarios are possible,[35] Case 1 requires a much more involved synthesis steps than Case 2. However, Case 1 has the clear advantage of resulting only in T-structures, when the attractive *rest all* interactions are chosen carefully, and neither chain nor dimer formation occurs.

Limitations of the Ising lattice DFT model: The lattice DFT model is one of the simplest approaches to understand the self-assembly of anisotropic particles. This model enables determination of thermodynamic equilibrium structures at the cost of very little computational time. However, the model makes several assumptions; (i) the dynamics of the self-assembly process are not considered in the model, (ii) the calculated density distributions are local density distributions around a center A particle at (0,0) and thus do not represent all assembled structures in the system, (iii)

particle-particle, particle-solvent molecule, and solvent-solvent molecule interactions are restricted to four specific points ignoring solvation and drag forces, and (iv) the effect of kinetic factors such as reaction rates are not included.

Including the dynamics in the calculations is a major challenge and sophisticated techniques such a molecular dynamics (MD) simulations are needed to understand the more realistic details of the assembly. As an extension of the current DFT model, we have implemented the dynamic lattice model with dynamic mean field (DMF) approximations for our system of particles. The proposed dynamic lattice model presents a simple extension of the DFT model which, by construction, evolves towards a free-energy minimum using a Monte Carlo (MC) method.[34]

4.3.4 The dynamic lattice model : dynamic mean field simulations

The lattice DFT model as discussed in subsection 4.3.1 yields equilibrium density distributions of particles on lattice sites, that correspond to the equilibrium self-assembled structures. The equilibrium density distributions are obtained by solving the coupled non-linear equations, that are the solutions for the density distributions at minimum free energy. Since multiple solutions are expected for the equilibrium density distributions Eq.(4.59), the calculated equilibrium density distributions are the density distributions representing a local free energy minimum and not the global minimum. Within the energy landscape, the transition path from initial random configurations to the equilibrium density distribution is not included in the DFT analysis. This time evolved transition of the initial state to the final equilibrium state is accounted when the dynamic DMF model is used.[66]

The DMF simulations are similar to the DFT method and include dynamic rules of motion for the particles on the lattice sites. The dynamic rules evolve the mean-field probabilities for the lattice sites from a given initial condition towards equilibrium.

The application of DMF simulations to the study of the structural phase behavior of anisotropic T-shaped molecules has been reported earlier.[34] We adopt the same technique to study the self-assembly of a mixture of three types of anisotropic particles (A, B_2 and C) into a T-structure.

Details of the calculations [34,66] A lattice model with an identical nomenclature (subsection 4.3.1) to the DFT model is used for the DMF simulations. Dynamic rules of motion are defined for the time evolution from the initial state to the final state. The particles can undergo translational and rotational diffusion at each time step. During rotation, the particles can interchange between four orientations (Figure 4.15) at a lattice site. The translational diffusion takes into account the self diffusion to the neighboring sites or exchange between neighboring particles.

The probability that a lattice site (i, j) is occupied by a p type of particle (p = A, B_2, and C) with orientation k (k = 1 - 4) at time t is given by $x_t(k, p, i, j)$. The master dynamic equation under the mean field approximation including rotation and translation is written as:

$$\begin{aligned} x_{t+1}(k,p,i,j) &= x_t(k,p,i,j) + \\ &\sum_{l\neq k}\Big\{q_t(i,j;p,l\rightarrow p,k)x_t(l,p,i,j) - q_t(i,j;p,k\rightarrow p,l)x_t(k,p,i,j)\Big\} + \\ &\sum_{\acute{i},\acute{j}}\sum_{s}\sum_{l}\Big\{q_t(\acute{i},\acute{j},p,k\leftrightarrow i,j,s,l)x_t(k,p,\acute{i},\acute{j})x_t(l,s,i,j) \\ &-q_t(\acute{i},\acute{j},s,l\leftrightarrow i,j,p,k)x_t(l,s,\acute{i},\acute{j})x_t(k,p,i,j)\Big\} \end{aligned} \tag{4.60}$$

In the above equation (4.60) the summation over l includes the four orientations, the summation over s includes different types of particles in the system (A, B_2, and C), and the summation over $\acute{i}, \acute{j}$ includes the neighboring sites of i, j. The term $q_t(i, j; p, l \rightarrow p, k)$ is the transition probability by rotation from orientation l to orientation k for the p particle. The transition probability for translation $q_t(\acute{i}, \acute{j}, p, k \leftrightarrow i, j, s, l)$ involves exchanging the states between a p particle in orientation k at the

nearest neighbor site $(\acute{i}, \acute{j})$ and an s particle in orientation l at site (i, j). In particular, the positive term in the second summation contributes to an increase in $x_t(k, p, i, j)$ due to the event that the $\acute{i}, \acute{j}$ site is occupied by a p particle with a k orientation and the i, j site is occupied by an s particle with an l orientation and the two sites exchange states with a transition probability $q_t(\acute{i}, \acute{j}, p, k \leftrightarrow i, j, s, l)$. Similarly, the negative term indicates a decrease in $x_t(k, p, i, j)$ by exchanging the site i, j with a p particle in the orientation k with an s particle with orientation l at site $\acute{i}, \acute{j}$. Consistent with the mean field approximation, the transition probabilities can be written as:

$$q_t(i, j; p, l \rightarrow p, k) = \omega_1 \frac{\exp[-\beta E_t(k, p, i, j)]}{\exp[-\beta E_t(l, p, i, j)] + \exp[-\beta E_t(k, p, i, j)]} \tag{4.61}$$

$$q_t \quad (\acute{i}, \acute{j}, p, k \leftrightarrow i, j, s, l) = \tag{4.62}$$
$$\omega_2 \frac{\exp\big\{-\beta\big[E_t(k, p, i, j) + E_t(l, s, \acute{i}, \acute{j})\big]\big\}}{\exp\big\{-\beta\big[E_t(k, p, i, j) + E_t(l, s, \acute{i}, \acute{j})\big]\big\} + \exp\big\{-\beta\big[E_t(l, s, i, j) + E_t(k, p, \acute{i}, \acute{j})\big]\big\}}$$

In our calculations, we set ω_1 to be $1/6$ and ω_2 to be $1/88$. The temperature in the calculations is set to be the final temperature of the system. The energies appearing in the transition probabilities are calculated from the Hamiltonian of the system from the mean field approximations, for example:

$$E_t(k, p, i, j) = \frac{\partial H}{\partial x(k, p, i, j)} \tag{4.63}$$

The master equation given by Eq.(4.60) evolves with each time step till it reaches a stationary equilibrium state. The equilibrium stationary state is given by

$$q_t(i, j; p, l \rightarrow p, k) x_t(l, p, i, j) = q_t(i, j; p, k \rightarrow p, l) x_t(k, p, i, j) \tag{4.64}$$

$$q_t(\acute{i}, \acute{j}, p, k \leftrightarrow i, j, s, l) \qquad x_t(k, p, \acute{i}, \acute{j}) x_t(l, s, i, j) = \tag{4.65}$$
$$q_t(\acute{i}, \acute{j}, s, l \leftrightarrow i, j, p, k) x_t(l, s, \acute{i}, \acute{j}) x_t(k, p, i, j)$$

The deterministic nature of the DMF equations will evolve the initial configuration of particles towards the equilibrium or a metastable state. The steady-state solution of the DMF equations leads to a structural arrest of the solutions and ceases to evolve further. Thus, the DMF solutions can also be used for searching and locating the local free energy minima.[34]

4.3.5 Preliminary Results and discussion

The preliminary calculations for the mixture of A, B_2, and C particles (constituents of the T-structure for Case 2 as shown in Figure 4.14(b)) are done using the DMF simulations. Since Case 2 leads to a mixture of various structures (Figure 4.16), this systems of particles is chosen for calculations to demonstrate occurrence of such structures in calculations. The initial configuration of particles on the lattice is chosen with the assumption of an equal probability for any of the four orientations (Fig. 4.15) on a lattice site. Thus the initial condition states that the probability that a site (i, j) is occupied by a k orientation of the A particle is given by $x(k, A, i, j) = \mathrm{x}_{\infty A}/4$. Identical initial conditions for B_2 and C particles are used. The initial state can be identified as a liquid phase at high temperatures. The system is perturbed by an A particle at the center position $(0, 0)$. At lower temperatures, the system of particles evolves such that A, B_2, or C particles are strongly oriented in one of the four orientations at the lattice sites around the center A particle. This state is called an inhomogeneous phase. The probability of occupying the lattice sites with specific orientations of specific particles (A, B_2, or C) is governed by the interaction energies between the particles. The occurrence of such an inhomogeneous phase is identified as a structure phase. Note that there might be a number of other minimum free energy states and the obtained particular lowest energy state does not have any energetic advantage over the other lowest energy states. Occurrence of a particular inhomogeneous phase is a result of a system of particles following a particular path.

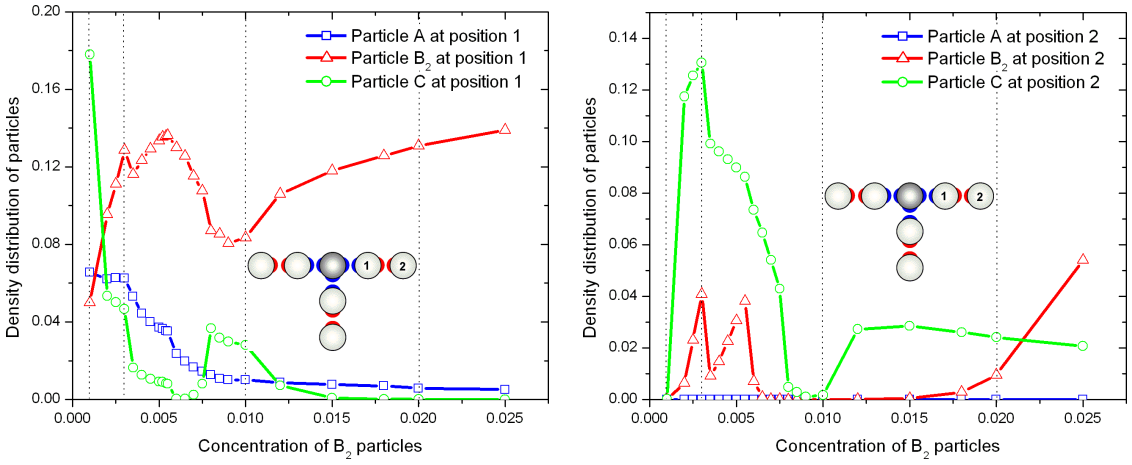

(a) (b)

Figure 4.20: Density distribution plots for A, B_2, and C particles at (a) position 1 and (b) position 2 as the concentration of B_2 particles is varied. The position 1 and position 2 in the T structure are shown in the inset T-structure. $x_{\infty A} = 0.0001$ and $x_{\infty C} = 0.0003$. *strong* attractive interaction energy = 3 eV, *weak* attractive energy = 0.5 eV and *rest all* attractive interaction energy = 0.1 eV. The surface density distribution plots corresponding to the dotted lines representing $x_{\infty B_2} = 0.003$, 0.01 and 0.02 are shown in Fig. 4.21

Figure 4.20 shows density distribution plots of A, B_2, and C particles at two positions (position 1 and position 2 indicated in Figure 4.20) in the T-structure. The parameters for the calculations are defined as *strong* attractive energy = 3 eV and *weak* attractive energy is 0.5 eV. Unlike the DFT calculations the *rest all* interactions are defined as attractive interactions (0.1 eV), which represents van der Waals interactions. The density distribution plots are obtained with increasing concentration of B_2 particles to study its effect on the inhomogeneous structure phase observed in the calculations. Figure 4.21 shows surface plots of the total density distribution ($x_A + x_{B_2} + x_C$) with parameters shown by dotted lines in Figure 4.20. The surface plots are used to understand the inhomogeneous structure phases existing in the calculations. The schematic of particle structures existing in the surface plots are shown in Figure 4.22.

The probability to form the T-structure is higher when the probabilities of position 1 occupied by a B_2 particle and position 2 occupied by a C particle are higher. Figures

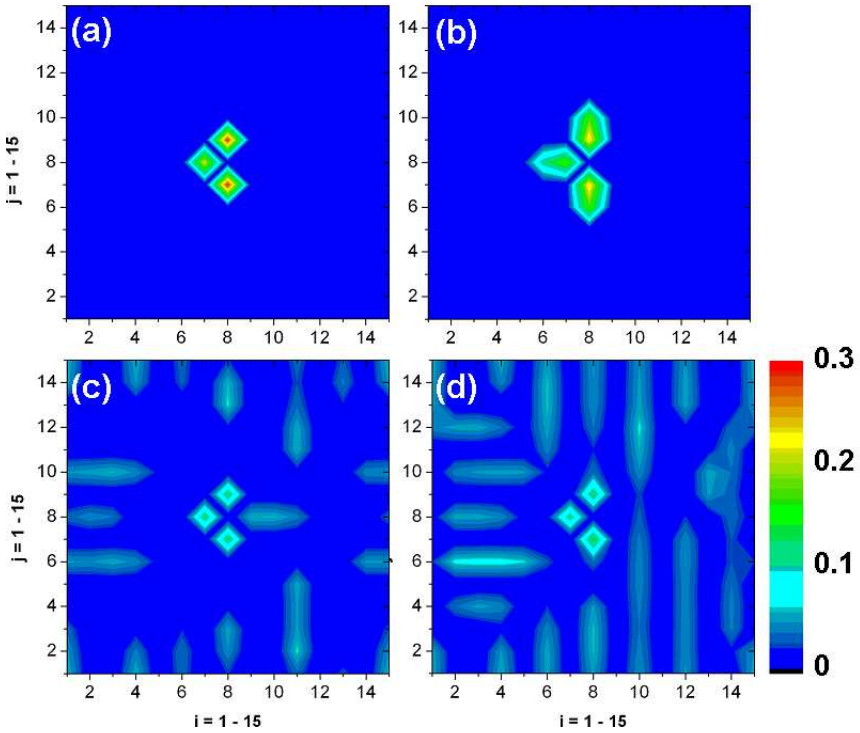

Figure 4.21: The total density distribution ($x_A + x_{B_2} + x_C$) surface plots around the center A particle at (0,0). The surface plots shows density distributions on 15 × 15 lattice. The plots corresponds to $x_{\infty A} = 0.0001$ and $x_{\infty C} = 0.0003$ and (a) $x_{\infty B_2} = 0.0001$, (b) $x_{\infty B_2} = 0.003$, (c) $x_{\infty B_2} = 0.01$, and (d) $x_{\infty B_2} = 0.02$. The (a) - (d) surface plots corresponds to the density distributions corresponding to the conditions shown by dotted lines in Fig. 4.20

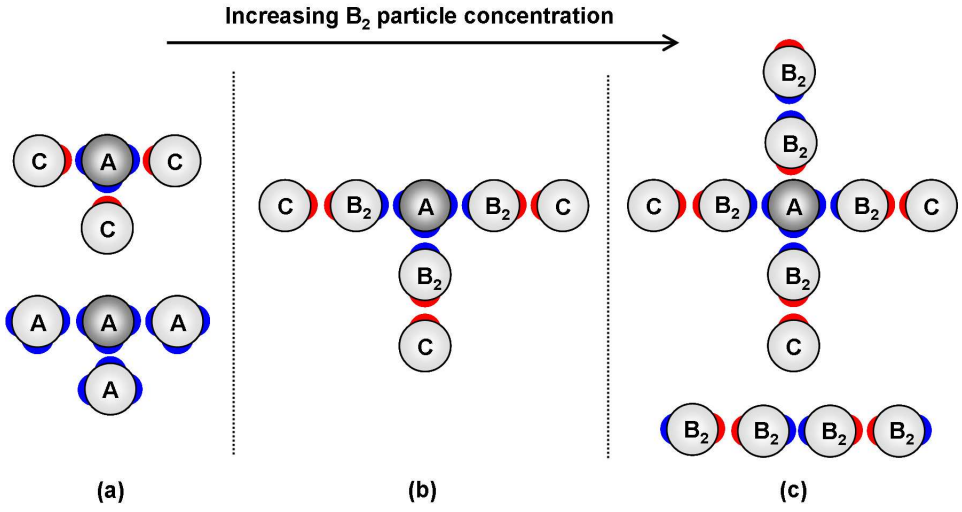

Figure 4.22: Schematic of structures existing in calculations representing the surface plots in Figure 4.21 around the center A particle shown in dark grey color. Figures (a)-(c) shows different structures observed as concentration of B_2 particles is increased.

4.20 (a) and (b) show that both probabilities are higher at $x_{\infty B_2} = 0.003$ and any increase or decrease in B_2 decreases the probability of forming the T-structure and leads to formation of other structures.

At lower concentration of B_2 particles ($x_{\infty B_2} = 0.0001$), the concentrations of A and C particles ($x_{\infty A} = 0.0001$ and $x_{\infty C} = 0.0003$) are high enough that attractive *weak* interactions dominate and lead to structures depicted in Figure 4.21(a) or as shown schematically in Figure 4.22(a). Increasing the B_2 particle concentration ($x_{\infty B_2} = 0.003$) favors position 1 for B_2 and position 2 for C particles through *strong* attractive interactions. Thus, the probability of T-structure formation is higher as shown in Figure 4.21(b). With further increase of the concentration of B_2 particles ($x_{\infty B_2} = 0.01$ and 0.02), the concentration of B_2 particles dominates the system leading to formation of chains of B_2 particles as observed in Figure 4.21(c) and (d) and schematically shown in Fig.4.22(c).

It should be noted that a similar trend in transition of structures from condensation of A particles to T-structure to chains of B_2 particles is observed in the static DFT model as the concentrations of A and C particles are fixed and the concentration of B_2 particles is increased (Figure 4.18(a)).

The main constraint in both the static DFT and the dynamic DMF simulations in our approach is that the local structure phase around a center A particle is studied. Thus, the density distributions obtained are the local distributions of particles around A particles and results do not represent the whole system dynamics or thermodynamics as the local structures around the B_2 or C particles are not accounted for in the calculations. Calculations with B_2 or C particles at the center position need to be considered to reflect the self-assembly in the entire system of particles. Our preliminary calculations with B_2 and C particles at the center position have shown that chains and dimers of B_2 and C particles are formed preferably. Also more sophisticated techniques such as MD simulations should be implemented in the future

for a more realistic study of the assembly of patchy particles.

Chapter 5

Conclusions and Future work

5.1 Concluding remarks

In this thesis, we have presented a systematic study of the fabrication of surface-anisotropic (patchy) particles. Exploring the applications of patchy particles in directed assembly by virtue of an external electric field, as osmotic motors, and the computational study of the assembly of a target T-structure, we have demonstrated the novelty of these materials.

The Glancing angle vapor deposition technique is successfully employed to fabricate metallo-dielectric patchy particles with gold patches on polystyrene particles. The versatility of the technique is demonstrated by fabricating patchy particles with patch size varying from 3.7 % to 50 % of the particle surface. We have further extended the GLAD technique to produce multifunctional patchy particles with identical or different patches. We have shown that the adjustment of simple vapor deposition parameters such as the deposition angle and the angle between two depositions can be used to control the overlap of multiple patches and the relative patch orientations on the particle surface. The particle stamping technique is successfully used to gain access to the entire particle surface for surface modification, which produces independent, non-overlapping patches.

The AC dielectrophoretic assembly of patchy particles is investigated towards the

fabrication of 2D metallo-dielectric crystals. Our findings suggest that the directed assembly of metallo-dielectric patchy particles is controlled by the relative proportion of metallic patch on the particle surface. We show that, as the patch size is varied from 50 % to 25 % to 11 % of the particle surface, the DEP assembled crystal structure can be tuned from staggered chains (50 % and 25 %) with a variable chain width to network structures of particles formed through horizontal and vertical chains (11 %). Further, network structures with diagonal chains have been demonstrated using patchy particles with two non-overlapping patches (25 % each) on opposite poles.

For the use of patchy particles as osmotic motors, we primarily focused on studying the effect of the patch size on the particle motion. The concentration gradient produced due to the surface-catalyzed decomposition of hydrogen peroxide by platinum patches on the surface of patchy particles leads to autonomous motion of such particles. As the patch size is increased from 11 % to 25 % to 50 % of the particle surface, the increase in the particle velocity is characterized experimentally. A concentration gradient model is proposed to understand the effect of the patch size on the particle motion. An analytical solution for the particle velocity is obtained in terms of the potential for solute - particle interaction.

A lattice density functional approach has been used to investigate the assembly of three types of patchy particles into a T-structure. The effect of particle concentration and particle interaction energies on the assembly has been elucidated. It has been shown that the careful choice of particle patch interactions can lead to desired target structures, such as a T-structure. Density distributions around a particle with three patches are used to analyze the structures formed. These distributions represent conditional probabilities of finding certain particles as neighbors to the three-patch particle. However, a detailed study including the dynamics of the assembly is needed.

In summary, this research suggests that patchy particles present a new challenging class of materials. Control of the surface-anisotropy provides a handle to tune their

properties. The demonstrated results indicate many interesting new avenues for the application of patchy particles.

5.2 Future work

Specific thoughts about the directions for the future work are discussed below.

1. In the present study we developed a technique to produce patchy particle using GLAD. The technique can be extended to produce a wide variety of patchy particles by changing simple experimental parameters. Thus, not limited to the particles described here, a variety of other patchy particles can be fabricated. For example, a simple extension of rotating the sample during vapor deposition will lead to azimuthally symmetric patches. Also, multiple vapor depositions (i.e., more than two), can lead to more complex patch geometries.

2. Secondly, the self-assembly of patchy particles by organic linker molecules that bind specifically to the patches presents an interesting proposal towards the practical application of these particles. For example, di-thiol molecules can be used to bind particles possessing gold patches together into dimers, trimers, or more complex structures such as a T-structure.

3. In future studies of patchy particles as osmotic motors, it is necessary to determine the direction of particle motion with respect to the patch. The direction of motion can be studied by labeling the platinum patches with fluorescent probes and using fluorescent microscopy for imaging. Also, determination of a potential function that can be fitted in the proposed model to determine the particle velocities as a function of patch size is necessary.

4. More detailed computational study of the self-assembly of patchy particles using sophisticated Monte-Carlo or Molecular Dynamics algorithms are essential

for understanding the dynamics behind the assembly. Based on the patch geometries obtained in the experiments various kind of model patchy particles can be implemented in the simulations to understand their assembly into specific target structures.

Appendix A

Osmotic motor : Calculations

The analytical solution for the concentration profile of hydrogen peroxide around the patchy particle and the particle velocity are described in this appendix.

Concentration gradient around the particle:

The diffusion equation in absence of convective transport (low Péclet number) for hydrogen peroxide can be written as:

$$D\nabla^2 C = 0 \tag{A.1}$$

subject to the boundary conditions:

$$\lim_{r\to\infty} C(r,\theta) = C_\infty \tag{A.2}$$

and

$$C(a,\theta) = 0, \qquad 0 \le \theta < \alpha_{Pt} \tag{A.3}$$

$$\frac{\partial}{\partial r} C(a,\theta) = 0, \qquad \alpha_{Pt} < \theta \le \pi \tag{A.4}$$

where a is the particle radius and α_{Pt} is the platinum cap angle. The radial co-ordinate and the concentration are non-dimensionalized by,

$$R = \frac{r}{a}, \qquad \overline{C}(R,\theta) = \frac{C(r,\theta)}{C_\infty}. \tag{A.5}$$

Separation of variables gives the axisymmetric solution of the Laplace Eq.(A.1) in

terms of non-dimensionalized concentration as

$$\overline{C}(R,\theta) = \sum_{n=0}^{\infty} \left[B_n R^n + A_n R^{-(n+1)} \right] P_n(\cos\theta) \tag{A.6}$$

where $P_n(\cos\theta)$ are Legendre polynomials of order n. Using the non-dimensionalized form of the boundary condition (A.2), we get

$$B_0 = 1, \qquad B_n = 0, \quad n > 0 \tag{A.7}$$

$$\therefore \quad \overline{C}(R,\theta) = 1 + \sum_{n=0}^{\infty} A_n R^{-(n+1)} P_n(\cos\theta) \tag{A.8}$$

Substituting Eq.(A.8) into the boundary conditions (A.3) and (A.4) yields the dual Fourier-Legendre series

$$\sum_{n=0}^{\infty} A_n P_n(\cos\theta) = -1, \quad 0 \le \theta < \alpha_{Pt} \tag{A.9}$$

and

$$\sum_{n=0}^{\infty} (n+1) A_n P_n(\cos\theta) = 0, \quad \alpha_{Pt} < \theta \le \pi \tag{A.10}$$

The constants A_n are obtained by solving the dual series (A.9) and (A.10), which gives the concentration distribution (A.8). The solution procedure for the dual series is adopted from the literature[89] and the constant A_n are obtained as:

$$A_n = -\frac{\sin(n\alpha_{Pt})}{n\pi} - \frac{\sin[(n+1)\alpha_{Pt}]}{(n+1)\alpha_{Pt}} + \frac{2}{\pi} \int_{\alpha_{Pt}}^{\pi} \psi(\tilde{\varphi}) cos\left[\left(n + \frac{1}{2} \right) \tilde{\varphi} \right] d\tilde{\varphi} \tag{A.11}$$

where $\psi(\tilde{\varphi})$ is obtained as:

$$\psi(\varphi) = -\frac{\gamma}{\pi} \int_0^{\alpha_{Pt}} \cos(\tilde{\varphi}/2) L(\tilde{\varphi}, \varphi) d\tilde{\varphi} + \frac{\gamma}{\pi} \int_{\alpha_{Pt}}^{\pi} \psi(\tilde{\varphi}) L(\tilde{\varphi}, \varphi) d\tilde{\varphi} \tag{A.12}$$

where γ = -1/2 and

$$L(\tilde{\varphi},\varphi) = \ln\left|\frac{\cos(\tilde{\varphi}/2)+\cos(\varphi/2)}{\cos(\tilde{\varphi}/2)-\cos(\varphi/2)}\right| \tag{A.13}$$

Eq.(A.12) is solved numerically by introducing n nodal points between α_{Pt} and π at $\varphi_i = \alpha_{Pt} + ih$ where $i = 0, 1, 2...., n-1$ and $n = (\pi - \alpha_{Pt})/n$. Then, Eq.(A.12) becomes

$$\psi(\varphi_i) - \frac{\gamma}{\pi}\int_{\alpha_{Pt}}^{\pi}\psi(t)L(t,\varphi_i)dt = -\frac{\gamma}{\pi}\int_{0}^{\alpha_{Pt}}\cos(t/2)L(t,\varphi_i)dt \tag{A.14}$$

The left hand side term is solved by numerical integration. Eq.(A.14) is solved to obtain $\psi(i)$, which when substituted in Eq.(A.11) gives the coefficients A_n.

Derivation of the particle velocity

The coupling of the concentration gradient near the particle and the force field $-\nabla\phi$ produces stresses near the particle surface, which results in the motion of the fluid. The continuity and the Naiver-Stokes equation at low Reynolds number are

$$\nabla\cdot\mathbf{v} = 0, \tag{A.15}$$

$$\mu\nabla^2\mathbf{v} - \nabla p - C\nabla\phi = 0, \tag{A.16}$$

$$\mathbf{v} = 0 \qquad (r = a), \tag{A.17}$$

$$\mathbf{v} \to -U\mathbf{e}_\phi \qquad (r \to \infty), \tag{A.18}$$

where U is the unknown particle velocity. A stream function ψ is defined by

$$\mathbf{v} = \frac{\mathbf{e}_\phi}{r\sin\theta}\times\nabla\psi(r,\theta) \tag{A.19}$$

The pressure gradient term in Eq.(A.16) is eliminated by taking the curl of both sides of the equation.[90,91] We know,

$$\nabla^2\mathbf{v} = \nabla(\nabla.\mathbf{v}) - \nabla\times(\nabla\times\mathbf{v}) \tag{A.20}$$

$$\therefore \qquad -\nabla\times(\nabla p)+\mu\Big[\nabla\times\nabla(\nabla.\mathbf{v})-\nabla\times\nabla\times(\nabla\times\mathbf{v})\Big]=\nabla\times(C\nabla\phi)$$

From the identities of vector algebra

$$\nabla\times(C\nabla\phi)=C(\nabla\times\nabla\phi)+(\nabla C)\times(\nabla\phi)$$

Noticing that the curl of divergence is 0, and

$$\nabla\times\nabla\times\nabla\times\mathbf{v}=-\frac{\mathbf{e}_\phi}{r\sin\theta}E^4\psi$$

$$\therefore \quad \mu\frac{\mathbf{e}_\phi}{r\sin\theta}E^4\psi=(\nabla C)\times(\nabla\phi)=\bigg(-\frac{1}{r}\frac{\partial C(r,\theta)}{\partial\theta}\frac{\partial\phi}{\partial r}\bigg)\mathbf{e}_\phi \tag{A.21}$$

Eq.(A.21) is non-dimensionalization by defining the variables as:

$$R=\frac{r}{a}, \qquad \Psi=\frac{\psi}{Ua^2}, \qquad \overline{C}(R,\theta)=\frac{C(r,\theta)}{C_\infty}, \qquad \Phi=\frac{\phi}{kT}. \tag{A.22}$$

substituting the non-dimensionalized $\overline{C}(R,\theta)$ from Eq.(A.8), we get

$$\begin{aligned}\frac{\partial C(r,\theta)}{\partial\theta} &= C_\infty\sum_{n=0}^{\infty}A_nR^{-(n+1)}\frac{\partial}{\partial\theta}P_n(\cos\theta)\\ &= C_\infty\sum_{n=1}^{\infty}A_nR^{-(n+1)}\bigg(-\frac{C_{n+1}^{-1/2}(\cos\theta)(n)(n+1)}{\sin\theta}\bigg)\end{aligned} \tag{A.23}$$

where polynomial functions $C_{n+1}^{-1/2}$ are called Gegenbauer polynomials of degree (-1/2). For convenience, we replace $\cos(\theta)=\eta$ and $C_{n+1}^{-1/2}=-Q_n$ in Eq. (A.23). Therefore, Eq.(A.21) leads to;

$$E^4\Psi=-\Lambda\sum_{n=1}^{\infty}\frac{A_n}{R^{(n+1)}}Q_n(\eta)(n)(n+1)\frac{\partial\Phi}{\partial R} \tag{A.24}$$

$$\Lambda = \frac{C_\infty akT}{\mu U} \tag{A.25}$$

The solution to Eq.(A.24) leads to the solution for the particle velocity U. Eq. (A.24) can be split into two second-order equations.

$$E^2\Psi = \omega, \tag{A.26}$$

$$E^2\omega = F. \tag{A.27}$$

$$F = -\Lambda \sum_{n=1}^{\infty} \left[\frac{A_n}{R^{(n+1)}}(n)(n+1)\frac{\partial \Phi}{\partial R} \right] Q_n(\eta) \tag{A.28}$$

The homogeneous solution of Eq.(A.27) is obtained by separation of variables. The homogeneous equation can be written as:

$$E^2\omega = 0 \tag{A.29}$$

where the operator E^2 is simplified as,

$$E^2 = \frac{\partial}{\partial R^2} + \frac{(1-\eta^2)}{R^2}\frac{\partial^2}{\partial \eta^2} \tag{A.30}$$

To solve (A.29), we assume that

$$\omega = S(R)H(\eta) \tag{A.31}$$

Hence substituting into (A.29) we obtain

$$\frac{R^2}{S^2}\frac{d^2S}{dR^2} + \frac{(1-\eta^2)}{H}\frac{d^2H}{d\eta^2} = 0 \tag{A.32}$$

The first term is a function of R only, whereas the second term is a function of η. Hence, we assume they both must be equal to a constant $n(n+1)$. The equation (A.32) thus splits into two equations,

$$R^2\frac{d^2S}{dR^2} - n(n+1)S = 0, \tag{A.33}$$

and

$$(1-\eta^2)\frac{d^2H}{d\eta^2}+n(n+1)H=0. \tag{A.34}$$

Equation (A.33) is a particular case of Euler's equation which gives two independent solutions of S as

$$S=R^{n+1},R^{-n}. \tag{A.35}$$

The later equation (A.34) is closely related to the Gegenbauer's equation of degree -1/2, solution to which can be written in term of Gegenbauer's polynomial or in terms of $Q_n(\eta)$. Thus the homogeneous solution of Eq.(A.29) can be written as

$$\omega_{homo}=\sum_{n=1}^{\infty}(a_nR^{n+1}+b_nR^{-n})Q_n(\eta) \tag{A.36}$$

The non-homogeneous solution is obtained through a substitution of the form[93]

$$\omega_{non-homo}=\sum_{n=1}^{\infty}H_nQ_n(\eta) \tag{A.37}$$

Applying the operator E^2 to ω ($\omega=\omega_{homo}+\omega_{non-homo}$) and substituting in Eq.(A.27), taking into account that $Q_n(\eta)$ satisfies Eq.(A.34), we obtain a second order equation for H_n as

$$R^2\frac{\partial^2H_n}{\partial R^2}-(n)(n+1)H_n=-\Lambda\frac{A_n(n)(n+1)}{R^{n+1}}\frac{\partial\Phi}{\partial R}R^2 \tag{A.38}$$

H_n has two independent homogeneous solutions of form $H_{n,homo}=R^{n+1}$ and R^{-n}, and the non-homogeneous solution obtained for Eq.(A.38) by method of variation of parameters gives the complete solution for H_n. The solution of ω is obtained as,

$$\omega=\omega_{homo}+\omega_{non-homo} \tag{A.39}$$

$$\omega = \sum_{n=1}^{\infty} \left\{ A_n R^{n+1} + B_n R^{-n} - \tilde{\Lambda} \int_{R_0}^{R} (s^{-(2n+1)} R^{n+1} - R^{-n}) \frac{\partial \phi}{\partial s} ds \right\} Q_n(\eta) \tag{A.40}$$

$$\tilde{\Lambda} = \Lambda \frac{A_n(n)(n+1)}{(2n+1)} = \frac{A_n C_\infty akT(n)(n+1)}{\mu U(2n+1)} \tag{A.41}$$

Substituting ω in Eq.(A.26), we get a non-homogeneous equation for Ψ which is of similar kind to Eq.(A.27). Following the same solution procedure from (A.29) to (A.40), we get the solution for Ψ as

$$\Psi = \sum_{n=1}^{\infty} \left\{ A_n R^{n+3} + B_n R^{-n+2} + C_n R^{n+1} + D_n R^{-n} - g_n(R) \right\} Q_n(\eta) \tag{A.42}$$

$$g_n(R) = \frac{1}{(2n+1)} \int_{R_0}^{R} (t^{-n} R^{n+1} - R^{-n} t^{n+1}) f_n(t) dt \tag{A.43}$$

$$f_n(t) = \tilde{\Lambda} \int_{R_0}^{t} (s^{-(2n+1)} t^{n+1} - t^{-n}) \frac{\partial \Phi}{\partial s} ds \tag{A.44}$$

The solution to Eq.(A.42) is sought with respect to the boundary conditions

$$\Psi(1) = \Psi'(1) = 0 \tag{A.45}$$

$$\Psi(\infty) \to \frac{1}{2} R^2 \sin^2 \theta \tag{A.46}$$

Substituting the boundary conditions (A.45) and (A.46) in (A.42) and matching the

powers of $\sin\theta$ we get the constants as:

$$\begin{aligned} & & A_n &= 0,\ (n \geq 1) \\ C_1 &= -1, & C_n &= 0,\ (n > 1) \\ B_1 &= -\frac{3}{2}C_1 + \frac{1}{2}\left(g_1 + \frac{\partial g_1}{\partial R}\right)_{R\to 1}, & B_n &= \frac{1}{2}\left(g_n + \frac{\partial g_n}{\partial R}\right)_{R\to 1}, (n > 1) \\ D_1 &= \frac{1}{2}C_1 + \frac{1}{2}\left(g_1 - \frac{\partial g_1}{\partial R}\right)_{R\to 1}, & D_n &= \frac{1}{2}\left(g_n - \frac{\partial g_n}{\partial R}\right)_{R\to 1}, (n > 1) \end{aligned} \quad \text{(A.47)}$$

Thus, the solution for Ψ is given as:

$$\begin{aligned} \Psi &= \left(B_1 R + C_1 R^2 + D_1 R^{-1} - g_1(R)\right) Q_1(\eta) \\ &\quad + \sum_{n=2}^{\infty} \left\{ B_n R^{-n+2} + D_n R^{-n} - g_n(R) \right\} Q_n(\eta) \end{aligned} \quad \text{(A.48)}$$

The drag on the particle in non-dimensional form is calculated as:[93,94]

$$\frac{F_z}{2\pi\mu U a} = \int_0^{\pi} \left\{ R^4 \frac{\partial}{\partial R}\left(\frac{E^2\Psi}{R^2}\right) \frac{-Q_1(\eta)}{\sin\theta} d\theta \right\} \quad \text{(A.49)}$$

Eq.(A.49) does not contain a term for the body force, because of the assumption that $-\nabla\Phi$ is only a function of R and not of θ.

$$E^2\Psi = \omega = \sum_{n=1}^{\infty} \left\{ A_n R^{n+1} + B_n R^{-n} - \tilde{\Lambda} \int_{R_0}^{R} (s^{-(2n+1)} R^{n+1} - R^{-n}) \frac{\partial \phi}{\partial s} ds \right\} Q_n(\eta) \quad \text{(A.50)}$$

The polynomial functions $Q_n(\eta)$ satisfy the orthogonality condition

$$\begin{aligned} \int_{-1}^{1} \frac{Q_n(\eta) Q_m(\eta)}{(1-\eta^2)} d\eta &= 0 && n \neq m \\ &= \frac{2}{n(n+1)(2n+1)} && n = m \end{aligned} \quad \text{(A.51)}$$

substituting $\eta = \cos\theta$, the orthogonality condition becomes

$$\int_0^{\pi} \frac{Q_n(\cos\theta) Q_m(\cos\theta)}{\sin\theta} d\theta = \frac{1}{3} \quad \text{(A.52)}$$

Substituting (A.50) into (A.49) and substituting the constants $A_n = 0$ from Eq.(A.47)

$$\frac{F_z}{2\pi\mu U a} = \int_0^\pi \left\{ R^4 \sum_{n=1}^{\infty} \left[(-n-2) B_n R^{-n-3} - \frac{\partial}{\partial R}\left(\frac{f_n(R)}{R^2} \right) \right] Q_n(\eta) \right\} \left\{ \frac{-Q_1(\eta)}{\sin\theta} \right\} d\theta \tag{A.53}$$

Using the orthogonality of Q_n's (A.52),

$$\frac{F_z}{2\pi\mu U a} = B_1 + \frac{1}{3}\left[R^4 \frac{\partial}{\partial R}\left(\frac{f_1(R)}{R^2} \right) \right]_{R\to 1} \tag{A.54}$$

In order to obtain an expression for U in terms of known parameters, another physical constraint is needed. This is achieved by equating the net drag force to zero. Thus, substituting B_1 from (A.47) in (A.54):

$$\frac{3}{2} + \frac{1}{2}\left(g_1 + \frac{\partial g_1}{\partial R} \right)_{R\to 1} + \frac{1}{3}\left[R^4 \frac{\partial}{\partial R}\left(\frac{f_1(R)}{R^2} \right) \right]_{R\to 1} = 0 \tag{A.55}$$

$$\therefore \qquad U = -\frac{1}{3}\left\{ \left(\tilde{g_1}(R) + \frac{\partial \tilde{g_1}(R)}{\partial R} \right)_{R\to 1} \right\} - \frac{2}{9}\left\{ R^4 \frac{\partial}{\partial R}\left(\frac{\tilde{f_1}(R)}{R^2} \right) \right\}_{R\to 1} \tag{A.56}$$

where $\tilde{g}_n$ and $\tilde{f}_n$ are obtained from (A.43) and (A.44) by multiplying g_n and f_n by U.

$$\tilde{g_1}(R) = \frac{1}{3}\int_{R_0}^{R} (t^{-1}R^2 - R^{-1}t^2)\tilde{f}_1(t)dt \tag{A.57}$$

$$\tilde{f_1}(t) = \Upsilon_1 \int_{R_0}^{t} (s^{-3}t^2 - t^{-1})\frac{\partial \Phi}{\partial s} ds \tag{A.58}$$

$$\Upsilon_n = \frac{A_n C_\infty akT(n)(n+1)}{\mu(2n+1)} \tag{A.59}$$

Accounting for the oxygen concentration gradient the corrected particle velocity

can be written as,

$$\begin{aligned} U &= -\frac{1}{3}\left\{\frac{1}{2}\left(\tilde{g_1}(R)+\frac{\partial\tilde{g_1}(R)}{\partial R}\right)_{R\to 1}+\frac{1}{3}\left(R^4\frac{\partial}{\partial R}\frac{\tilde{f_1}(R)}{R^2}\right)_{R\to 1}\right\}_{H_2O_2} \\ &\quad -\frac{1}{3}\left\{\frac{1}{2}\left(\tilde{g_1}(R)+\frac{\partial\tilde{g_1}(R)}{\partial R}\right)_{R\to 1}+\frac{1}{3}\left(R^4\frac{\partial}{\partial R}\frac{\tilde{f_1}(R)}{R^2}\right)_{R\to 1}\right\}_{O_2} \end{aligned} \tag{A.60}$$

Appendix B

Lattice DFT calculations

Details of the calculations:

$x_{1,p,i,j}$, $x_{2,p,i,j}$, $x_{3,p,i,j}$, and $x_{4,p,i,j}$ are the probabilities of finding a p type particle ($p = A$, B_n : $n = 1, 2$, or C) with a particular orientation at the lattice site (i, j). The total density $\rho(i, j)$ for a p type particle at site (i, j) is thus given by:

$$\rho_p(i,j) = x_{1,p,i,j} + x_{2,p,i,j} + x_{3,p,i,j} + x_{4,p,i,j} \tag{B.1}$$

The Hamiltonian for the two neighboring sites has contributions from the interactions between the same types of particles (AA, B_nB_n, and CC) as well as between different types of particles (AB_n, AC, and B_nC) and can be written as:

$$E = \left(\frac{1}{2}\right) \sum_{a=particle1}^{particle3} \sum_{b=particle1}^{particle3} \sum_{m=orientation1}^{orientation4} \sum_{n=orientation1}^{orientation4} (\epsilon_{abmn} p(a,m) p(b,n)) \tag{B.2}$$

where ϵ_{abmn} is the interaction energy between the ath and bth type of particle (a, b $= 1 - 3$) with the contact points m and n ($m, n = 1 - 4$). $p(a, m)$ and $p(b, n)$ are the respective probabilities of finding the ath and bth type of particle on neighboring sites to have a contact point m on the ath type of particle and a contact point n on

the bth type of particle. The total Hamiltonian thus can be written as:

$$
\begin{aligned}
U \;=\; & \left(\frac{1}{2}\right)\sum_{p=1}^{3}\sum_{q=1}^{3}\sum_{i=-i^*}^{i^*}\sum_{j=-j^*}^{j^*} \qquad\qquad (B.3)\\
& (x_{1,p,i,j}x_{1,q,i+1,j}\epsilon_{pq24} + x_{1,p,i,j}x_{2,q,i+1,j}\epsilon_{pq23} + x_{1,p,i,j}x_{3,q,i+1,j}\epsilon_{pq22} + x_{1,p,i,j}x_{4,q,i+1,j}\epsilon_{pq21}\\
& +x_{2,p,i,j}x_{1,q,i+1,j}\epsilon_{pq14} + x_{2,p,i,j}x_{2,q,i+1,j}\epsilon_{pq13} + x_{2,p,i,j}x_{3,q,i+1,j}\epsilon_{pq12} + x_{2,p,i,j}x_{4,q,i+1,j}\epsilon_{pq11}\\
& +x_{3,p,i,j}x_{1,q,i+1,j}\epsilon_{pq44} + x_{3,p,i,j}x_{2,q,i+1,j}\epsilon_{pq43} + x_{3,p,i,j}x_{3,q,i+1,j}\epsilon_{pq42} + x_{3,p,i,j}x_{4,q,i+1,j}\epsilon_{pq41}\\
& +x_{4,p,i,j}x_{1,q,i+1,j}\epsilon_{pq34} + x_{4,p,i,j}x_{2,q,i+1,j}\epsilon_{pq33} + x_{4,p,i,j}x_{3,q,i+1,j}\epsilon_{pq32} + x_{4,p,i,j}x_{4,q,i+1,j}\epsilon_{pq31})\\
& +(x_{1,p,i,j}x_{1,q,i-1,j}\epsilon_{pq42} + x_{1,p,i,j}x_{2,q,i-1,j}\epsilon_{pq41} + x_{1,p,i,j}x_{3,q,i-1,j}\epsilon_{pq44} + x_{1,p,i,j}x_{4,q,i-1,j}\epsilon_{pq43}\\
& +x_{2,p,i,j}x_{1,q,i-1,j}\epsilon_{pq32} + x_{2,p,i,j}x_{2,q,i-1,j}\epsilon_{pq31} + x_{2,p,i,j}x_{3,q,i-1,j}\epsilon_{pq34} + x_{2,p,i,j}x_{4,q,i-1,j}\epsilon_{pq33}\\
& +x_{3,p,i,j}x_{1,q,i-1,j}\epsilon_{pq22} + x_{3,p,i,j}x_{2,q,i-1,j}\epsilon_{pq21} + x_{3,p,i,j}x_{3,q,i-1,j}\epsilon_{pq24} + x_{3,p,i,j}x_{4,q,i-1,j}\epsilon_{pq23}\\
& +x_{4,p,i,j}x_{1,q,i-1,j}\epsilon_{pq12} + x_{4,p,i,j}x_{2,q,i-1,j}\epsilon_{pq11} + x_{4,p,i,j}x_{3,q,i-1,j}\epsilon_{pq14} + x_{4,p,i,j}x_{4,q,i-1,j}\epsilon_{pq13})\\
& +(x_{1,p,i,j}x_{1,q,i,j+1}\epsilon_{pq13} + x_{1,p,i,j}x_{2,q,i,j+1}\epsilon_{pq12} + x_{1,p,i,j}x_{3,q,i,j+1}\epsilon_{pq11} + x_{1,p,i,j}x_{4,q,i,j+1}\epsilon_{pq14}\\
& +x_{2,p,i,j}x_{1,q,i,j+1}\epsilon_{pq43} + x_{2,p,i,j}x_{2,q,i,j+1}\epsilon_{pq42} + x_{2,p,i,j}x_{3,q,i,j+1}\epsilon_{pq41} + x_{2,p,i,j}x_{4,q,i,j+1}\epsilon_{pq44}\\
& +x_{3,p,i,j}x_{1,q,i,j+1}\epsilon_{pq33} + x_{3,p,i,j}x_{2,q,i,j+1}\epsilon_{pq32} + x_{3,p,i,j}x_{3,q,i,j+1}\epsilon_{pq31} + x_{3,p,i,j}x_{4,q,i,j+1}\epsilon_{pq34}\\
& +x_{4,p,i,j}x_{1,q,i,j+1}\epsilon_{pq23} + x_{4,p,i,j}x_{2,q,i,j+1}\epsilon_{pq22} + x_{4,p,i,j}x_{3,q,i,j+1}\epsilon_{pq21} + x_{4,p,i,j}x_{4,q,i,j+1}\epsilon_{pq24})\\
& +(x_{1,p,i,j}x_{1,q,i,j+1}\epsilon_{pq31} + x_{1,p,i,j}x_{2,q,i,j-1}\epsilon_{pq34} + x_{1,p,i,j}x_{3,q,i,j+1}\epsilon_{pq33} + x_{1,p,i,j}x_{4,q,i,j-1}\epsilon_{pq32}\\
& +x_{2,p,i,j}x_{1,q,i,j-1}\epsilon_{pq21} + x_{2,p,i,j}x_{2,q,i,j-1}\epsilon_{pq24} + x_{2,p,i,j}x_{3,q,i,j-1}\epsilon_{pq23} + x_{2,p,i,j}x_{4,q,i,j-1}\epsilon_{pq22}\\
& +x_{3,p,i,j}x_{1,q,i,j-1}\epsilon_{pq11} + x_{3,p,i,j}x_{2,q,i,j-1}\epsilon_{pq14} + x_{3,p,i,j}x_{3,q,i,j-1}\epsilon_{pq13} + x_{3,p,i,j}x_{4,q,i,j-1}\epsilon_{pq12}\\
& +x_{4,p,i,j}x_{1,q,i,j-1}\epsilon_{pq41} + x_{4,p,i,j}x_{2,q,i,j-1}\epsilon_{pq44} + x_{4,p,i,j}x_{3,q,i,j-1}\epsilon_{pq43} + x_{4,p,i,j}x_{4,q,i,j-1}\epsilon_{pq42})
\end{aligned}
$$

i^* and j^* indicate the lattice size. The lattice site $(0,0)$ is occupied by a three patch particle (A particle) with the orientation 1 (i.e. $x_{1,A,0,0} = 1$).

The entropy of the system (per one site) in the mean field approximation can be

written as:

$$\begin{aligned} S &= k_B \sum \sum_{(i,j)\neq(0,0)} \Bigg\{ \Bigg[\sum_{p=1}^{3} (x_{1,p,i,j} \ln x_{1,p,i,j} + x_{2,p,i,j} \ln x_{2,p,i,j} + x_{3,p,i,j} \ln x_{3,p,i,j} \\ &\quad + x_{4,p,i,j} \ln x_{4,p,i,j}) \Bigg] + \Bigg[1 - \sum_{p=1}^{3} (x_{1,p,i,j} + x_{2,p,i,j} + x_{3,p,i,j} + x_{4,p,i,j}) \Bigg] \\ &\quad \Bigg[\ln \Big(1 - \sum_{p=1}^{3} (x_{1,p,i,j} + x_{2,p,i,j} + x_{3,p,i,j} + x_{4,p,i,j}) \Big) \Bigg] \Bigg\} \end{aligned} \tag{B.4}$$

The free energy, F, can be obtained from Eqs.(B.3) and (B.4) as:

$$F = U - TS \tag{B.5}$$

For an open system the Grand potential, Ω, Eq.(B.6) must be minimized at equilibrium, which gives a variational equation (B.7)[99] in the absence of an external potential.

$$\Omega[x_{k,p,i,j}] = F[x_{k,p,i,j}] - \sum_{p=1}^{3} \mu_p \Bigg\{ \sum_{i=-i^*}^{i^*} \sum_{j=-j^*}^{j^*} \sum_{k=1}^{k=4} x_{k,p,i,j} \Bigg\} \tag{B.6}$$

$$\frac{\partial \Omega[x_{k,p,i,j}]}{\partial x_{k,p,i,j}} = 0 \tag{B.7}$$

where μ_p is the chemical potential of the species p. Eq.(B.7) and Eqs.(B.3 -B.5) give:

$$E_{k,p} + k_B T \ln \left\{ \frac{x_{k,p,i,j}}{1 - \sum_{q=1}^{3} (x_{1,q,i,j} + x_{2,q,i,j} + x_{3,q,i,j} + x_{4,q,i,j})} \right\} = \mu_p \tag{B.8}$$

where the terms $E_{k,p}$ are defined by:

$$\begin{aligned} E_{1,p} = \sum_{q=1}^{3} \quad & \{ x_{1,q,i+1,j} \epsilon_{pq24} + x_{2,q,i+1,j} \epsilon_{pq23} + x_{3,q,i+1,j} \epsilon_{pq22} + x_{4,q,i+1,j} \epsilon_{pq21} \\ & + x_{1,q,i-1,j} \epsilon_{pq42} + x_{2,q,i-1,j} \epsilon_{pq41} + x_{3,q,i-1,j} \epsilon_{pq44} + x_{4,q,i-1,j} \epsilon_{pq43} \\ & + x_{1,q,i,j+1} \epsilon_{pq13} + x_{2,q,i,j+1} \epsilon_{pq12} + x_{3,q,i,j+1} \epsilon_{pq11} + x_{4,q,i,j+1} \epsilon_{pq14} \\ & + x_{1,q,i,j-1} \epsilon_{pq31} + x_{2,q,i,j-1} \epsilon_{pq34} + x_{3,q,i,j-1} \epsilon_{pq33} + x_{4,q,i,j-1} \epsilon_{pq32} \} \end{aligned} \tag{B.9}$$

$$E_{2,p} = \sum_{q=1}^{3} \quad \{x_{1,q,i+1,j}\epsilon_{pq14} + x_{2,q,i+1,j}\epsilon_{pq13} + x_{3,q,i+1,j}\epsilon_{pq12} + x_{4,q,i+1,j}\epsilon_{pq11}$$
$$+x_{1,q,i-1,j}\epsilon_{pq32} + x_{2,q,i-1,j}\epsilon_{pq31} + x_{3,q,i-1,j}\epsilon_{pq34} + x_{4,q,i-1,j}\epsilon_{pq33}$$
$$+x_{1,q,i,j+1}\epsilon_{pq43} + x_{2,q,i,j+1}\epsilon_{pq42} + x_{3,q,i,j+1}\epsilon_{pq41} + x_{4,q,i,j+1}\epsilon_{pq44}$$
$$+x_{1,q,i,j-1}\epsilon_{pq21} + x_{2,q,i,j-1}\epsilon_{pq24} + x_{3,q,i,j-1}\epsilon_{pq23} + x_{4,q,i,j-1}\epsilon_{pq22}\} \quad \text{(B.10)}$$

$$E_{3,p} = \sum_{q=1}^{3} \quad \{x_{1,q,i+1,j}\epsilon_{pq44} + x_{2,q,i+1,j}\epsilon_{pq43} + x_{3,q,i+1,j}\epsilon_{pq42} + x_{4,q,i+1,j}\epsilon_{pq41}$$
$$+x_{1,q,i-1,j}\epsilon_{pq22} + x_{2,q,i-1,j}\epsilon_{pq21} + x_{3,q,i-1,j}\epsilon_{pq24} + x_{4,q,i-1,j}\epsilon_{pq23}$$
$$+x_{1,q,i,j+1}\epsilon_{pq33} + x_{2,q,i,j+1}\epsilon_{pq32} + x_{3,q,i,j+1}\epsilon_{pq31} + x_{4,q,i,j+1}\epsilon_{pq34}$$
$$+x_{1,q,i,j-1}\epsilon_{pq11} + x_{2,q,i,j-1}\epsilon_{pq14} + x_{3,q,i,j-1}\epsilon_{pq13} + x_{4,q,i,j-1}\epsilon_{pq12}\} \quad \text{(B.11)}$$

$$E_{4,p} = \sum_{q=1}^{3} \quad \{x_{1,q,i+1,j}\epsilon_{pq34} + x_{2,q,i+1,j}\epsilon_{pq33} + x_{3,q,i+1,j}\epsilon_{pq32} + x_{4,q,i+1,j}\epsilon_{pq31}$$
$$+x_{1,q,i-1,j}\epsilon_{pq12} + x_{2,q,i-1,j}\epsilon_{pq11} + x_{3,q,i-1,j}\epsilon_{pq14} + x_{4,q,i-1,j}\epsilon_{pq13}$$
$$+x_{1,q,i,j+1}\epsilon_{pq23} + x_{2,q,i,j+1}\epsilon_{pq22} + x_{3,q,i,j+1}\epsilon_{pq21} + x_{4,q,i,j+1}\epsilon_{pq24}$$
$$+x_{1,q,i,j-1}\epsilon_{pq41} + x_{2,q,i,j-1}\epsilon_{pq44} + x_{3,q,i,j-1}\epsilon_{pq43} + x_{4,q,i,j-1}\epsilon_{pq42}\} \quad \text{(B.12)}$$

The values of μ_p can be obtained from the requirement that all $x_{k,p,i,j} = x_{\infty,p}/4$, as the distance from the center molecule goes to infinity. Thus from Eq.(B.8) we get:

$$E_{0,p} + k_B T \ln \left\{ \frac{x_{\infty,p}/4}{1 - \sum_{q=1}^{3} x_{\infty,q}} \right\} = \mu_p \quad \text{(B.13)}$$

where $E_{0,p}$ is obtained from Eqs.(B.9 - B.12) and $x_{k,p,i,j} = x_{\infty,p}/4$. Combining

Eq.(B.8) and Eq.(B.13) results in:

$$k_B T \ln\left\{\frac{x_{k,p,i,j}\Big(1-\sum_{q=1}^{3} x_{\infty,q}\Big)}{\Big(1-\sum_{q=1}^{3} x_{1,q,i,j}+x_{2,q,i,j}+x_{3,q,i,j}+x_{4,q,i,j}\Big)\Big(x_{\infty,p}/4\Big)}\right\}+E_{k,p}-E_{0,p}=0 \tag{B.14}$$

which can be represented in the following form:

$$x_{k,p,i,j}=\left\{\frac{x_{\infty,p}\exp\left[\frac{E_{0,p}-Ek,p}{k_B T}\right]}{4\big(1-\sum_{q=1}^{3} x_{\infty,q}\big)+\sum_{q=1}^{3}\sum_{s=1}^{4} x_{\infty,q}\exp\left[\frac{E_{0,q}-Es,q}{k_B T}\right]}\right\} \tag{B.15}$$

.

Bibliography

(1) Manna, L.; Scher, E. C.; Alivisatos, A. P. *J. Am. Chem. Soc.* **2000**, *122*, 12700–12706.

(2) Sun, Y. G.; Xia, Y. N. *Science* **2002**, *298*, 2176–2179.

(3) Yu, Y. Y.; Chang, S. S.; Lee, C. L.; Wang, C. R. *J. Phys. Chem. B* **1997**, *101*, 6661–6664.

(4) Love, J. C.; Gates, B. D.; Wolfe, D. B.; Paul, K. E.; Whitesides, G. M. *Nano Lett.* **2002**, *2*(8), 891–894.

(5) Chen, S.; Wang, Z. L.; Ballato, J.; Foulger, S. H.; Carroll, D. L. *J. Am. Chem. Soc.* **2003**, *125*, 16186–16187.

(6) Sung, K. E.; Vanapalli, S. A.; Mukhija, D.; McKay, H. A.; Millunchick, J. M.; Burns, M. A.; Solomon, M. J. *J. Am. Chem. Soc.* **2008**, *130*, 1335–1340.

(7) Cayre, O.; Paunov, V. N.; Velev, O. D. *J. Mater. Chem.* **2003**, *13*(10), 2445–2450.

(8) Perro, A.; Reculusa, S.; Ravaine, S.; Bourgeat-Lami, E. B.; Duguet, E. *J. Mater. Chem.* **2005**, *15*, 3745–3760.

(9) Roh, K. H.; Martin, D. C.; Lahann, J. *Nature Mater.* **2005**, *4*, 759–763.

(10) Zhang, G.; Wang, D.; Mohwald, H. *Angew. Chem. Int. Ed.* **2005**, *44*, 7767–7770.

(11) Zhang, G.; Wang, D.; Mohwald, H. *Nano Lett.* **2005**, *5*, 143–146.

(12) Snyder, C. E.; Yake, A. M.; Feick, J. D.; Velegol, D. *Langmuir* **2005**, *21*, 4813–4815.

(13) Hong, L.; Jiang, S.; Granick, S. *Langmuir* **2006**, *22*, 9495–9499.

(14) Cui, J. Q.; Kretzschmar, I. *Langmuir* **2006**, *22*, 8281–8284.

(15) Gennes, P. G. D. *Rev. Mod. Phys.* **1992**, *64*, 645–648.

(16) Takei, H.; Shimizu, N. *Langmuir* **1997**, *13*, 1865–1868.

(17) Gangwal, S.; Cayre, O. J.; Velev, O. D. *Langmuir* **2008**, *24*, 13312–13320.

(18) Hong, L.; Cacciuto, A.; Luijten, E.; Granick, S. *Nano lett.* **2006**, *6*, 2510–2514.

(19) Glotzer, S. C.; Solomon, M. J. *Nature Mater.* **2007**, *6*, 557–562.

(20) Liddell, C. M.; Summers, C. J.; Gokhale, A. M. *Mater. Chacter.* **2003**, *50*, 69–79.

(21) Champion, J. A.; Katare, Y. K.; Mitragotri, S. *Proc. Nat. Acad. Sci.* **2007**, *104*, 11901–11904.

(22) Langer, R.; Tirrell, D. *Nature* **2004**, *428*, 487–492.

(23) Gratzel, M. *Nature* **2001**, *414*, 338–344.

(24) Ito, T.; Okazaki, S. *Nature* **2000**, *406*, 1027–1031.

(25) Brust, M.; Kiely, C. *Coll. Surf. A* **2002**, *202*, 175–186.

(26) Glotzer, S. C.; Solomon, M. J.; Kotov, N. A. *AICHE J.* **2004**, *50*, 2978–2985.

(27) Boncheva, M.; Whitesides, G. M. *MRS Bull.* **2005**, *30*, 736–742.

(28) Aranovich, G. L.; Donohue, M. D. *J. Chem. Phys.* **2002**, *116*(16), 7255–7268.

(29) Zhang, Z.; Glotzer, S. C. *Nano Lett.* **2004**, *4*, 1407–1413.

(30) Malescio, G.; Pellicane, G. *Phys. Rev. E* **2004**, *70*, 021202.

(31) Glotzer, S. C.; Horsch, M. A.; Iacovella, C. R.; Zhang, Z. L.; Chan, E. R.; Zhang, X. *Curr. Opin. Coll. Interf. Sci.* **2005**, *10*, 287–295.

(32) Zhang, Z.; Keys, A. S.; Chen, T.; Glotzer, S. C. *Langmuir* **2005**, *21*, 11547–11551.

(33) Vanakaras, A. G. *Langmuir* **2006**, *22*, 88–93.

(34) Witman, J. E.; Wang, Z. G. *J. Phys. Chem. B* **2006**, *110*, 6312–6324.

(35) Pawar, A. B.; Kretzschmar, I.; Aranovich, G. L.; Donohue, M. D. *J. Phys. Chem. B* **2007**, *111*, 2081–2089.

(36) Casagrande, C.; Fabre, P.; Raphael, E.; Veyssie, M. *Europhys. Lett.* **1989**, (3), 251–255.

(37) Paunov, V. N. *Langmuir* **2003**, *19*, 7970–7976.

(38) Fujimoto, K.; Nakahama, K.; Shidara, M.; Kawaguchi, H. *Langmuir* **1999**, *15*, 4630–4635.

(39) Nakahama, K.; Kawaguchi, H.; Fujimoto, K. *Langmuir* **2000**, *16*, 7882–7886.

(40) Yake, A. M.; Snyder, C. E.; Velegol, D. *Langmuir* **2007**, *23*, 9069–9075.

(41) Jiang, S.; Granick, S. *Langmuir* **2008**, *24*, 2438–2445.

(42) Roh, K. H.; Martin, D. C.; Lahann, J. *J. Am. Chem. Soc.* **2006**, *128*, 6796–6797.

(43) Roh, K. H.; Yoshida, M.; Lahann, J. *Langmuir* **2007**, *23*, 5683–5688.

(44) Zhang, G.; Wang, D.; Mohwald, H. *Chem Mater* **2006**, *28*, 3985–3992.

(45) Howse, J. R.; Jones, R. A. L.; R, A. J.; Gough, T.; Vafabakhsh, R.; Golestanian, R. *Phys. Rev. Lett.* **2007**, *99*, 048102.

(46) Chastek, T. T.; Hudson, S. D.; Hackley, V. A. *Langmuir* **2008**, *24*, 13897–13903.

(47) Takahara, Y. K.; Ikeda, S.; Ishino, S.; Tachi, K.; Ikeue, K.; Sakata, T.; Hasegawa, T.; Mori, H.; Matsumura, M.; Ohtani, B. *J. Am. Chem. Soc.* **2005**, *127*, 6271–6275.

(48) Dinsmore, A. D.; Hsu, M. F.; Nikolaides, M. G.; Marquez, M.; Bausch, A. R.; Weitz, D. A. **2002**, *298*, 1006–1009.

(49) Petit, L.; Manaud, J. P.; Mingotaud, C.; Ravaine, S.; Duguet, E. *Mater. Lett.* **2001**, *51*, 478–484.

(50) Nisisako, T.; Torii, T.; Higuchi, T. *Chem. Eng. J.* **2004**, *101*, 23–29.

(51) Nie, Z.; Li, W.; Seo, M.; Xu, S.; Kumacheva, E. *J. Am. Chem. Soc.* **2006**, *128*, 9408–9412.

(52) Haynes, C. L.; Duyne, R. P. V. *J. Phys. Chem. B* **2001**, *105*, 5599–5611.

(53) Deckman, H. W.; Dunsmuir, J. H. *Appl. Phys. Lett.* **1982**, *41*, 377–379.

(54) Zhao, Y. P.; Ye, D. X.; Wang, P. I.; Wang, G. C.; Lu, T. M. *Int. J. Nanosci.* **2002**, *1*, 87–97.

(55) Zhao, Y. P.; Ye, D. X.; Wang, P. I.; Wang, G. C.; Lu, T. M. *Nano Lett.* **2002**, *2*(4), 351–354.

(56) Haynes, C. L.; McFarland, A. D.; Smith, M. T.; Hulteen, J. C.; Duyne, R. P. V. *J. Phys. Chem. B* **2002**, *106*, 1898–1902.

(57) Yoshida, M.; Lahann, J. *ACS Nano* **2008**, *2*, 1101–1107.

(58) Gangwal, S.; Cayre, O. J.; Bazant, M. Z.; Velev, O. D. *Phys. Rev. Lett.* **2008**, *100*, 058302.

(59) Crowley, J. M.; Sheridon, N. K.; Romano, L. *J. Electrostat.* **2002**, *55*, 247–259.

(60) Paxton, W. F.; Kistler, K. C.; Olmeda, C. C.; Sen, A.; Angelo, S. K. S.; Cao, Y.; Mallouk, T. E.; Lammert, P. E.; Crespi, V. H. *J. Am. Chem. Soc.* **2004**, *126*, 13424–13431.

(61) Paxton, W. F.; Sundararajan, S.; Mallouk, T. E.; Sen, A. *Angew. Chem. Int. Ed.* **2006**, *45*, 5420–5429.

(62) Ismagilov, R. F.; Schwartz, A.; Bowden, N.; Whitesides, G. M. *Angew. Chem. Int. Ed.* **2002**, *41*, 652–654.

(63) Anderson, J. L. *Ann. Rev. Fluid. Mech.* **1989**, *21*, 61–99.

(64) Golestanian, R.; Liverpool, T. B.; Ajdari, A. *Phys. Rev. Lett.* **2005**, *94*, 220801.

(65) Sear, R. P. *J. Chem. Phys.* **1999**, *111*(10), 4800–4806.

(66) Wang, Z. G. *Phys. Rev. A* **1992**, *45*, 692–701.

(67) Pawar, A. B.; Kretzschmar, I. *Langmuir* **2008**, *24*, 355–358.

(68) Himmelhaus, M.; Takei, H. *Sensor. Actuator B* **2000**, *63*(1-2), 24–30.

(69) Prevo, B. G.; Velev, O. D. *Langmuir* **2004**, *20*, 2099–2107.

(70) Kralchevsky, P. A.; Nagayama, K. *Adv. Colloid interf. Sci.* **2000**, *85*, 145–192.

(71) Israelachvili, J. *Intermolecular and Surface Forces;* Academic Press : New York, 2 ed., 1991.

(72) Kralchevsky, P. A.; Denkov, N. D. *Adv. Colloid Interface Sci* **2000**, *85*, 145–192.

(73) Kralchevsky, P. A.; Denkov, N. D. *Curr. Opin. Colloid Interface Sci* **2001**, *6*, 383–401.

(74) Denkov, N. D.; Velev, O. D.; Kralchevsky, P. A.; Ivanov, I. B.; Yoshimura, H.; Nagayama, K. *Langmuir* **1992**, *8*, 3183–3190.

(75) Postek, M. T.; Vladar, A. E. *Microsc. Microanal.* **2005**, *11*, 388–389.

(76) McDermott, J. J.; Velegol, D. *Langmuir* **2008**, *24*, 4335–4339.

(77) Kralchevsky, P. A.; Nagayama, K. *Langmuir* **1994**, *10*, 23–36.

(78) Giersig, M.; Mulvaney, P. *J. Phys. Chem.* **1993**, *97*, 6334–6336.

(79) Lumsdon, S. O.; Kaler, E. W.; Velev, O. D. *Langmuir* **2004**, *20*, 2108–2116.

(80) Gong, T.; Marr, D. W. M. *Langmuir* **2001**, *17*, 2301–2304.

(81) Velev, O. D.; Bhatt, K. H. *Soft Matter* **2006**, *2*, 738–750.

(82) Russel, W. B.; Saville, D. A.; Schowalter, W. R. *Colloidal Dispersions;* Cambridge University Press, 1989.

(83) Morgan, H.; Green, N. G. *AC Electrokinetics: colloids and nanoparticles;* Research Studies press Ltd. Hertfordshire, UK, 2003.

(84) Giner, V.; Sancho, M.; Lee, R. S.; Martinez, G.; Pethig, R. *J. Phys. D: Appl. Phys.* **1999**, *32*, 1182–1186.

(85) Anderson, J. L.; Lowell, M. E.; Prieve, D. C. *J. Fluid. Mech.* **1982**, *117*, 107–121.

(86) Golestanian, R.; Liverpool, T. B.; Ajdari, A. *New J. Phys.* **2007**, *9*, 126.

(87) Figueroa, U. M. C.; Brady, J. F. *Phys. Rev. Lett.* **2008**, *100*, 158303.

(88) Darnton, N.; Turner, L.; Breuer, K.; Berg, H. C. *Biophys. J.* **2004**, *86*, 1863–1870.

(89) Duffy, D. G. *Mixed boundary value problems;* Chapman and Hall/CRC, 2008.

(90) Deen, W. M. *Analysis of transport phenomena;* Oxford University Press, 1998.

(91) Bird, R. B.; Stewart, W. E.; Lightfoot, E. N. *Transport phenomena;* John Wiley and Sons, Inc., 2002.

(92) Leal, L. G. *Advanced transport phenomena;* Cambridge University Press, 2007.

(93) Happel, J.; Brenner, H. *Low Reynolds Number Hydrodynamics: with special applications to particulate media (Mechanics of Fluids and Transport Processes);* Springer, 1973.

(94) Stimson, M.; Jeffery, G. B. *Proc. Roy. Soc. (London)* **1926**, *A111*, 110–116.

(95) Sukharev, M.; Seideman, T. *Nano Lett.* **2006**, *6*, 715–719.

(96) Chang, C. W.; Choi, Z. S.; Thompson, C. V.; Gan, C. L.; Pey, K. L.; Choi, W. K.; Hwang, N. *J. Appl. Phys.* **2006**, *99*, 0945051–0945057.

(97) Kiselev, A. A.; Rossler, U. *Semicond. Sci. Technol* **1996**, *11*, 203–206.

(98) Kiselev, A. A.; Kim, K. W. *J. Appl. Phys.* **2003**, *94*, 4001–4005.

(99) Xu, J. *AICHE Journal* **2006**, *52*, 1169–1193.

(100) Aranovich, G. L.; Donohue, M. D. *Phys. Rev. E* **1999**, *60*, 5552–5560.